The Dissertation Committee for Lauren Joy De Pue Certifies that this is the approved version of the following dissertation:

Design and Analysis of Precursors for CVD of Ru Thin Films and Li-Ion Batteries with MoP_4 Anode Materials

Committee:

Richard A. Jones, Supervisor

David A. Atwood

Bradley J. Holliday

Alan H. Cowley

Philip D. Magnus

John G. Ekerdt

Design and Analysis of Precursors for CVD of Ru Thin Films and Li-Ion Batteries with MoP_4 Anode Materials

by

Lauren Joy De Pue, B.S; M.S.

Dissertation

Presented to the Faculty of the Graduate School of

The University of Texas at Austin

in Partial Fulfillment

of the Requirements

for the Degree of

Doctor of Philosophy

The University of Texas at Austin

August 2013

Dedication

For my family and friends,
who always have faith in me.
I cherish your love and support.

Thou ill-formed offspring of my feeble brain,
Who after birth didst by my side remain,
Till snatched from thence by friends, less wise than true,
Who thee abroad, exposed to public view,
Made thee in rags, halting to th' press to trudge,
Where errors were not lessened (all may judge).
At thy return my blushing was not small,
My rambling brat (in print) should mother call,
I cast thee by as one unfit for light,
The visage was so irksome in my sight;
Yet being mine own, at length affection would
Thy blemishes amend, if so I could.
I washed thy face, but more defects I saw,
And rubbing off a spot still made a flaw.
I stretched thy joints to make thee even feet,
Yet still thou run'st more hobbling than is meet;
In better dress to trim thee was my mind,
But nought save homespun cloth i' th' house I find.
In this array 'mongst vulgars may'st thou roam.
In critic's hands beware thou dost not come,
And take thy way where yet thou art not known;
If for thy father asked, say thou hadst none;
And for thy mother, she alas is poor,
Which caused her thus to send thee out of door.
~Anne Bradstree

Acknowledgements

I would like to thank my advisor, Professor Richard A. Jones for all of his knowledge, guidance, and mentorship, which have helped me tremendously during my graduate career, and for which I will always be grateful. In addition, I'd like to thank my committee: Dr. Alan H. Cowley, Dr. Bradley J. Holliday, Dr. Philip D. Magnus, Dr. John G. Ekerdt, for their support and helpful discussions about my research projects. Last but not least on my committee is my undergraduate advisor Dr. David A. Atwood. I would not be earning a higher degree without his allowing me to join his group as a freshman. I owe him a world of thanks for showing me what chemistry could be. I would also like to thank Dr. Keith Stevenson and his students for their assistance with electrochemical experiments.

I'd like to thank my co-workers, Justin Hall, Dr. Joseph Rivers, Dr. Jeff McCarty, Dr Xiaoping Yang, and Dr. Kyris Agapiou for their friendship, research discussions and help along the way.

Design and Analysis of Precursors for CVD of Ru Thin Films and Li-Ion Batteries with MoP_4 Anode Materials

Lauren Joy De Pue, Ph.D.

The University of Texas at Austin, 2013

Supervisor: Richard A. Jones

The chemical vapor deposition growth of amorphous metallic alloys is currently of interest for potential uses in electronic devices. We have explored the use of ligands having Ru-H, Ru-N, and Ru-P bonds to study the effects of ligand selection. The synthesis and design of novel Ru dinuclear complexes using volatile ligands such as 3,5-bis-trifluoromethylpyrazolate and trimethylphosphine will be presented as well as materials characterization studies on grown films.

Another class of functional materials of interest is the transition metal phosphides (TMPs) which have found applications in Li-ion batteries. Current research on TMPs is focused on obtaining materials with improved or new compositions and morphologies and on improving Li insertion/de-insertion reactions and charge carrying capacities. Traditional routes to these materials involve the use of high temperatures and pressures. The work presented here will focus on a synthetic route which employs relatively mild conditions. Surface analysis studies and the electrochemical performance of mesoporous MoP_4 for use as anode materials in Li-ion batteries will be described.

Table of Contents

List of Tables

List of Figures

List of Schemes

Chapter 1: Introduction

1.1: Background on CVD

Amorphous thin films of Ru, are peculiar metallic materials, usually lacking the long-range order of normal, crystalline metals. The amorphous nature of these materials results in the absence of crystalline defects typical of metals such as grain boundaries, dislocations, and stacking faults.[1] They have therefore received considerable interest for their extraordinary engineering properties such as strength, hardness, toughness, and elasticity. Thin films of Ru are currently of interest for use in a number of microelectronics applications, including use as a Cu diffusion barrier and Cu seed layer due to its low resistivity (~7 $\mu\Omega$,cm), chemical stability, and low solubility with Cu.[2] The decrease in size of the integrated circuit has initiated the drive for research on novel materials that maintain a high current density and low leakage currents. Methods to grow thin films in the dimensions needed for the modern electronics industry have driven the advancement of research in the deposition process.[3]

The deposition of thin films generally falls into two categories, chemical vapor deposition (CVD) and physical vapor deposition (PVD). Using CVD as the method films with good step coverage and uniform coatings may be obtained from this technique. By comparison, PVD techniques employ sputtering or evaporation for surface covering and are considered line-of-sight techniques, which cover horizontal and flat surfaces well but it is an inadequate method for complex microelectronics.[4] PVD can deposit alloys but not from a single source resulting in sputtering of different species that have different volatilities which lead to films of uneven compositions.[5] The vaporization of PVD materials can be done using numerous techniques including: evaporative heating, sputter deposition, and pulsed laser deposition, all which require high inputs of energy and high vacuum systems.[5,6]

In contrast, CVD differs from PVD by utilizing lower deposition temperatures; high deposition rates; can be deposited on planar and non-planar surfaces; and overall results in the growth of films of high purity.[3] The CVD technique employs one or more volatile organometallic or inorganic precursors that can be transported via a gaseous phase to the deposition chamber where the substrate is positioned. The precursor moves along with a carrier gas which can be either inert (e.g., Ar) or reactive (e.g., H_2) at lower pressures. The deposition chamber is heated to the optimized temperature at which the precursor decomposes and as the precursor enters the chamber it decomposes on the surface of the substrate and the by-products and volatile ligands are swept away leaving the deposited metallic alloy. The precursor decomposes through a series of complex chemical reactions that may involve oxidation, reduction, or others that result in thin layer formation of the film. Figure I-1 is a schematic of the CVD apparatus used to grow films of materials described in the following chapters. By controlling all stages of the CVD pathway (temperatures, flow rate, and pressure) this technique is useful for studying the physical properties that control the thermodynamics and kinetics resulting in different film morphologies.

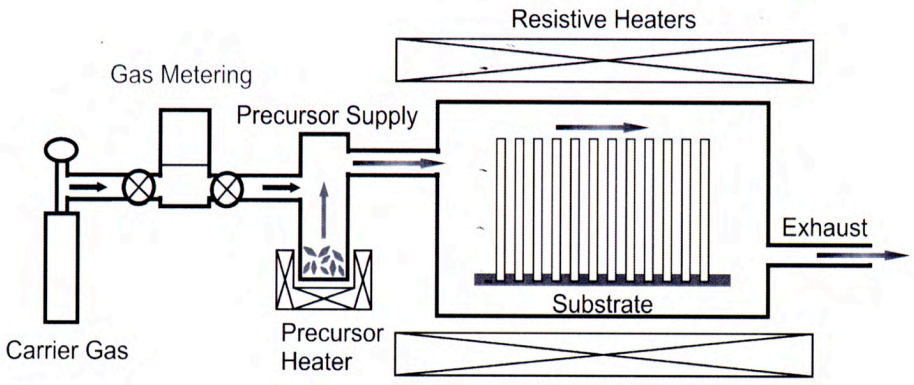

Figure I-1: Arrangement of the equipment of the CVD apparatus.

1.2: BACKGROUND ON CVD PRECURSOR DESIGN AND THE USE OF MICROWAVE ENERGY

Precursor design is most important for development of a variety of thin films. First, a precursor must be volatile in order to be a qualified candidate for CVD. The molecular structure of the precursor affects its volatility and thus, the choice of ligands is important to the design of CVD precursors. Previous research in screening viable CVD precursors include metal carbonyls of $W(CO)_6$,[7] $Cr(CO)_6$,[8] $Co_2(CO)_8$,[9] and $Mo(CO)_6$[10] which are all volatile and have been used for CVD of thin films of W, Cr, Co, and Mo. Not all films grown using these precursors eliminate CO during deposition and research has branched out to examine other organometallic complexes as potential CVD precursors including those at contain metal halides (WF_6),[5] metal alkyls ($Ga(CH_3)_3$),[11] multinuclear complexes ($Ga(As^tBu_2)_3$,[12] and organometallic complexes containing unsaturated ligands of alkene, allyl, and cyclopentadienyl and other dative and anionic ligands that fulfill coordination number and oxidation state requirements, such as, $Rh(\eta^3\text{-allyl})_3$,[13] Ir(Cp)(COD),[2] and $[Rh(3,5\text{-}(CF_3)_2\text{-Pz})(\eta^2\text{-}C_2H_4)_2]_2$.[14] Other single source precursors have been used to deposit thin films of metal nitrides using $(Me_3CN)_2W(NHCMe_3)_2$, and $(^tBuN)_2W(NH^tBu)_2$[3] as well as metal phosphides of In.[4]

Coordination compounds containing organic ligands with heteroatoms such as N, O, and P are widely studied for CVD precursors. These ligands include β-diketonates, pyrazolates, and trialkyl phosphines. The ligands break down during decomposition and the decomposition products are either carried away as volatile by-products or are incorporated into the film. CVD precursors using β-diketonates such as 1,1,1,5,5,5-hexafluoro-2-4-pentanedionate (hfa) and 2,2,6,6-tetramethylheptane-3,5-dione (tmhd) include $Cu(hfa)_2$[6] and $Ru(tmhd)_3$.[15] There are a variety of pyrazolates which increases the volatility of CVD precursors especially bis(trifluoromethyl)pyrazolate (3,5-$(CF_3)_2$-Pz). These precursors include $Os(CO)(3,5\text{-}(CF)\text{-Pz})$,[16] $Ru(CO)_3(3,5\text{-}(CF_3)_2\text{-Pz})]_2$,[17] $Ag(3,5\text{-}(CF_3)_2\text{-Pz})_3$,[18] and $Rh_2(\mu\text{-}3,5\text{-}(CF_3)_2\text{-Pz})_4$.[19]

CVD precursors with trialkyl phosphines can be used to grow metallic films of high purity as well as incorporate some P into the film composition. This P content has been shown to prevent the crystalline formation of the film creating amorphous phases. Recent work in the Jones and Ekerdt laboratories demonstrated the use of *cis*-$RuH_2(PMe_3)_4$ as a CVD precursor for Ru that has a substantial P content (15-28 %) with films that are amorphous which show promise as barrier layers for Cu diffusion (Figure I-2).[20]

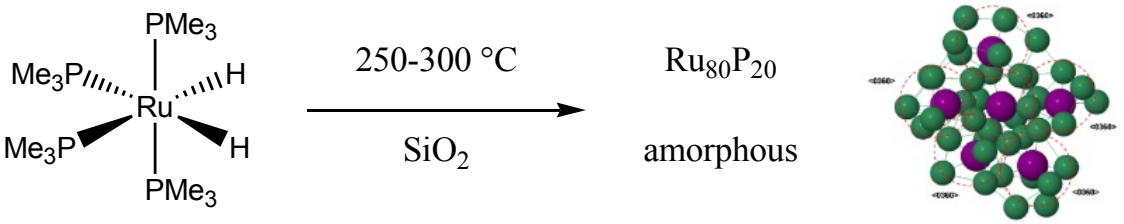

I-1

Figure I-2: CVD conditions using *cis*-$RuH_2(PMe_3)_4$ to grow amorphous films of $Ru_{80}P_{20}$.[20]

Film morphologies are also dependent on substrate type and temperature conditions during CVD growth. Impurity levels depend strongly on the precursor and carrier gas used. For example, films grown using argon as the carrier gas using $[Rh(3,5\text{-}(CF_3)_2\text{-}Pz)(\eta^2\text{-}C_2H_4)_2]_2$ at 170 ^{0}C contain 16 % Rh and 76 % C while films grown using H_2 as the carrier gas but otherwise under the same conditions deposited films of 58 % Rh and 42 % C.[19]

In order to expand upon the research of developing new CVD precursors for the growth of films of Ru with new compositions or morphologies we have used a Ru source that is known be a suitable CVD precursor, $[Ru(CO)_3(\mu\text{-}Pz\text{-}CF_3)]_2$. The replacement of one or more CO ligands with suitable phosphine ligands such as PMe_3 should produce volatile single source CVD precursors which can be used to deposit thin films containing both Ru and P. Interestingly, the CO substitution process proved difficult using

conventional methods and so another approach was used to synthesize new complexes in the form of microwave energy.

Microwave energy (MW) is commonly used to heat foods in microwave ovens in households worldwide. However, there are other potential applications for this method of rapid heating and scientists have discovered it is a good resource for chemical synthesis.[21-24] Professor Ajay K. Bose is credited to have been the pioneer of microwave laboratory instrumentation.[25-27]

When a molecule is irradiated with microwave radiation it rotates to align itself with the applied field. The frequency of molecular rotation is similar to that of the frequency of microwave radiation and consequently the molecule continually attempts to align itself with the changing field and the result is energy is absorbed. Microwave assisted organic reactions are "green" chemistry because it involves little to no solvent, thus diminishing waste disposal and savings in the cost of solvents.

Microwaves are considered a more efficient source of heating than conventional methods (oil bath heating), since the energy is directly imparted to the reaction medium rather than through the walls of a reaction vessel (Figure I-3). This efficient method of heating just the reagents in the reaction leads to a considerable saving of time.

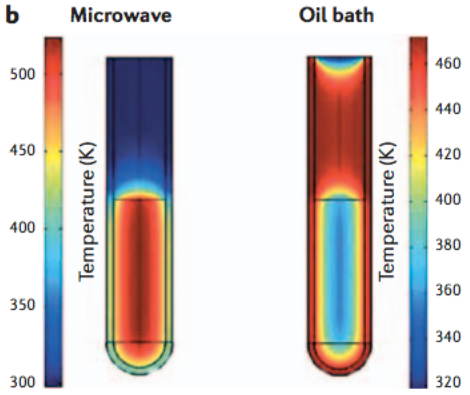

Figure I-3: Microwave irradiation and oil bath heating of a sample.[28]

Microwave assisted organic reactions are currently being used in a wide range of reactions from hydrogenation,[15] Diels-Alder cycloaddition,[29] aromatic substitution,[30] alkene functionalization,[31] esterification,[32] decarboxylations,[33] oxidation,[34] and many others.[21] In this thesis the use of microwave assisted techniques are described which are used to replace CO ligands with PMe_3 groups on a Ru compound in order to isolate and characterize novel CVD precursors.

1.3: BACKGROUND OF X-RAY PHOTOELECTRON SPECTROSCOPY (XPS) DEPTH PROFILING OF CVD FILMS

Solid materials interact with their surroundings through their surfaces. The physical and chemical composition of these surfaces determines the nature of the interactions and will influence such factors as corrosion rates, catalytic activity, adhesive properties, and contact potential. Surfaces influence many crucially important properties of the solid. X-ray Photoelectron Spectroscopy (XPS) is a surface analysis technique that can (a) evaluate which elements are present at the surface, (b) what chemical states these elements are in, (c) how much of each element are present, and (d) how uniform is the chemical composition of the film.[35] In XPS, the emission and energy analysis of low-energy electrons are liberated from the sample, which are then examined as a result of the photoemission process (Figure I-4).

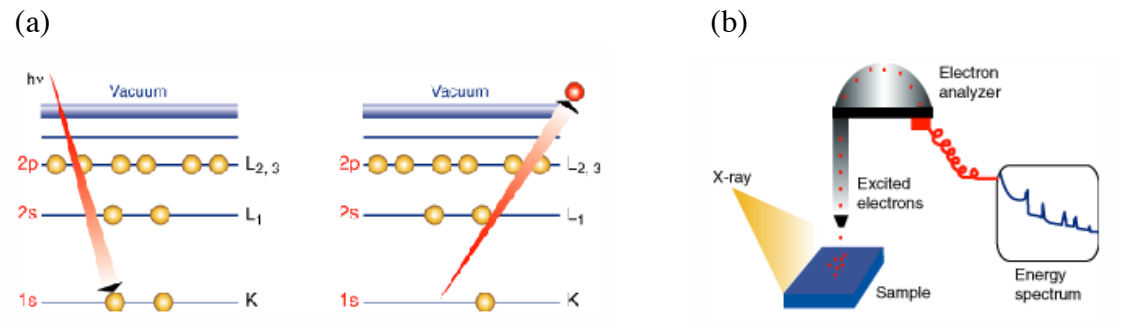

Figure I-4: (a) The photoemission principle of an x-ray (red arrow) bombarding a sample (left), some electrons (yellow spheres) become excited enough to escape the atom (right) and (b) Diagram of the inner workings of XPS spectroscopy.[36]

High resolution spectra as seen in the Ru 3d doublet in Figure I-5 are a visual source for interpreting the film composition. Carbon is a common source of impurities found in CVD films whether they have C due to exposure to the atmosphere or if the precursor deposited C into the film during deposition conditions. When analyzing films of Ru it is difficult to calculate the C content due to the binding energy of the C 1s singlet overlapping with that of the Ru $3d_{3/2}$ doublet at 285 eV. One method to estimate the amount of C is to use a peak fitting software and calculate the ratio of the Ru $3d_{5/2}$ to Ru $3d_{3/2}$ peak which should be 3:2 if no C is present. If more than one Ru species is accounted for in the film then analysis of C becomes even more difficult as the ratio begins to shift.

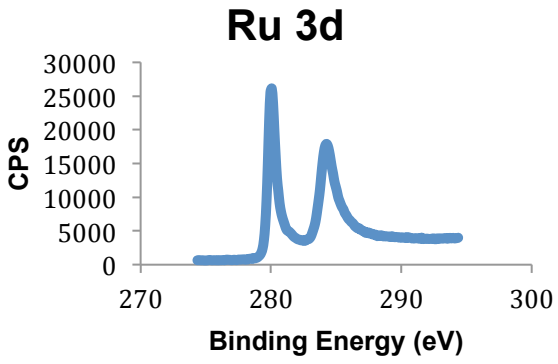

Figure I-5: High resolution XPS spectrum of Ru 3d doublet.

Although XPS is essentially a method of surface analysis it is possible to use it to provide some compositional information as a function of depth. This can be achieved in several ways: (a) manipulating the energy of the emitted electron and hence the information depth; (b) removing material mechanically and examining the freshly exposed surface; or (c) removing material from the surface *in situ* by ion sputtering. Analysis is then alternated with material removal and a compositional depth profile gradually built.[35] Sputter depth profiling is by far the most popular means of producing a compositional depth profile in surface analysis. The primary process of sputtering surface atoms away is to expose underlying atomic layers. A high-quality vacuum is essential to measure a good depth profile. If there are partial pressures or small changes in the vacuum pressure, the surface that is analyzed may not reflect the material composition with accuracy. It is possible to calculate the etch rate, but when analyzing a variety of films with different elements the rate needs to be calculated for each species. This can be difficult since current literature only calculates the etch rate for samples that are of one pure species while most films grown using CVD are composed of more than one elemental species. In chapter 4, use of the XPS technique is described for the study of films grown from CVD precursors and use depth profiling techniques to determine the consistencies of each film.

1.4: BACKGROUND ON NEW MATERIALS FOR LITHIUM ION BATTERIES

Devices such as lithium-ion batteries are currently the most promising power source for Plug-in Hybrid Electric Vehicles (PHEVs) and Electric Vehicles (EVs). These modes of transportation have the potential to greatly reduce CO_2 emissions and to reduce our dependence on foreign oil. Lithiated graphite is currently the most widely used anode but safer, cheaper, lighter, higher capacity and higher power materials are urgently needed in order to realize the full potential of PHEVs and EVs. Anode materials based

on inexpensive TMPs offer great promise for Li-ion batteries due to their exceptionally high gravimetric storage capacities and low intercalation potential. Nanostructured TMPs can significantly enhance mass transport rates and promote faster lithium ion reaction kinetics and can more easily accommodate volumetric changes and lattice stresses caused by phase transformations. Existing methods of preparing nano-sized particles of TMPs all employ high temperature routes and would be relatively difficult and expensive to scale up for manufacturing purposes. A new synthetic strategy involving clean, low temperature reactions of well-defined soluble transition metal organometallic species with phosphine (PH_3) has been recently reported.[37] The methodology offers great flexibility, ease of scale up and the potential to control morphology and stoichiometry.

A conventional lithium-ion battery (Figure I-6) contains a graphite anode (grey hexagons), a lithium cathode (lithium cobalt oxide in this case; brown circles), and a liquid electrolyte containing lithium ions (green) in a separator (orange). The removal of lithium ions by the simultaneous oxidation of cobalt in the cathode and insertion of lithium ions into the graphite anode charges the battery. Electricity is produced when ions move in the opposite direction and the cobalt is reduced.

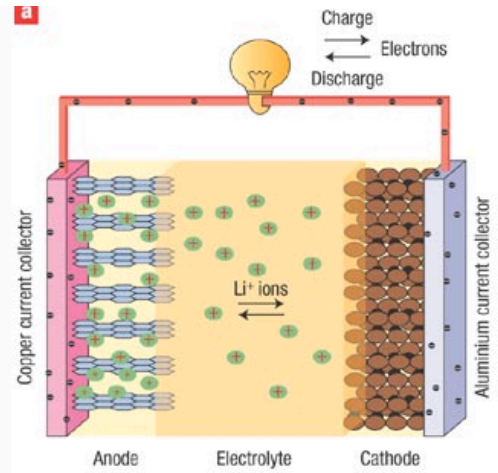

Figure I-6: Schematic of a conventional Li-ion battery.[38]

Here the goals of the proposed research are to explore new low temperature routes to mesoporous transition metal phosphides (TMPs) and to test these materials for advanced energy storage applications.

1.5: Overview and Scope

The work described in the following chapters can be divided into three categories. In the first category, the design and synthesis of new organometallic Ru complexes are discussed and screened for suitability as potential volatile CVD precursors (Chapters 2 and 3). The use of appropriate ligands which influence the volatile nature including 3,5-$(CF_3)_2$-Pz, and PMe_3 are employed for the production of these precursors.

In the second category, surface analysis of CVD films has been crucial to understanding the chemistry behind deposition of different compounds. Sputtering and depth profiling of films has been important to determine the purity, consistency of layers, and chemical composition of thin films of amorphous metals and metal alloys. The work described in Chapter 4 is focused on the use of XPS to establish the correlations between metal precursor and deposition parameters (temperature, pressure, carrier gas, etc.) and the chemical compositions of thin films comprising Rh, Ru, and Ni.

In the third category, the objectives of learning what factors affect TMP morphology and producing mesoporous materials that allow Li-ion transport using a low temperature preparation are explored (Chapter 5). TMPs with high surface area should allow Li-ion insertion/de-insertion reactions with little change in morphology after each cycle and should show improved performance as possible battery anode materials. The objectives of this work are to find amorphous TMPs of MoP_4 that will undergo the conversion process without changing phase, perform as reversible reactions, and are made using mild conditions.

1.6: REFERENCES

1. A. R. Yavari, *Nature (London)*, 2006, **439**, 405-406.

2. I. Goswami and R. Laxman, *Semiconductor International*, 2004, **27**, 49.

3. K. Seshan, *Handbook of Think-Film Deposition Processes and Techniques*, Noyes, Norwich, NY, 2002.

4. H. Lee, *Journal of Micromechanical Microengineering*, 2006, **16**, 557.

5. M. J. Hampden-Smith and T. T. Kodas, *The Chemistry of Metal CVD*, 1994.

6. D. L. Smith, *Thin-film Deposition: Principles and Practices*, McGraw-Hil, Boston, 1995.

7. E. A. Trifonova, D. S. Perekalin, K. A. Lyssenko and A. R. Kudinov, *J. Organomet. Chem.*, 2013, **727**, 60-63.

8. *Gmelins Handb. Anorg. Chem., Part C*, 1965, **16**, 45.

9. C. H. Wang, L. F. Xu, X.-L. Fan and J.-T. Wang, *Phys. Lett. A*, 2011, **375**, 562-567.

10. L. Calucci, F. G. N. Cloke, U. Englert, P. B. Hitchcock, G. Pampaloni, C. Pinzino, F. Puccini and M. Volpe, *Dalton Transactions*, 2006, 4228-4234.

11. H. Lee, *Journal of Microelectronics and Microengineering*, 2006, **16**, 557.

12. F. J. Williams, M. S. Tikhov, A. Palermo, N. Macleod and R. M. Lambert, *The Journal of Physical Chemistry B*, 2001, **105**, 2800-2808.

13. L. Marot, G. De Temmerman, V. Thommen, D. Mathys and P. Oelhafen, *Surface and Coatings Technology*, 2008, **202**, 2837-2843.

14. J. H. Rivers, L. J. DePue Anderson, C. M. N. Starr and R. A. Jones, *Dalton Transactions*, 2012, **41**, 5401-5408.

15. E. M. Gordon, D. C. Gaba, K. A. Jebber and D. M. Zacharias, *Organometallics*, 1993, **12**, 5020-5022.

16. Y. Chi, H.-L. Yu, W.-L. Ching, C.-S. Liu, Y.-L. Chen, T.-Y. Chou, S.-M. Peng and G.-H. Lee, *J. Mater. Chem.*, 2002, **12**, 1363-1369.

17. Y. H. Song, Y. L. Chen, Y. Chi, C. S. Liu, W. L. Ching, J. J. Kai, R. S. Chen, Y. S. Huang and A. J. Carty, *Chemical Vapor Deposition*, 2003, **9**, 162-169.

18. Y. Chi, E. Lay, T. Y. Chou, Y. H. Song and A. J. Carty, *Chemical Vapor Deposition*, 2005, **11**, 206-212.

19. W. J. McCarty, X. Yang, L. J. D. Anderson and R. A. Jones, *Dalton Transactions*, 2012, **41**, 173-179.

20. J. Shin, A. Waheed, K. Agapiou, W. A. Winkenwerder, H.-W. Kim, R. A. Jones, G. S. Hwang and J. G. Ekerdt, *J. Am. Chem. Soc.*, 2006, **128**, 16510-16511.

21. V. K. Ahluwalia, *Alternate energy processes in chemical synthesis : microwave, ultrasonic, and photo activation*, Alpha Science International Ltd., Oxford, U.K. :, 2008.

22. S. Caddick, *Tetrahedron*, 1995, **51**, 10403-10432.

23. L. Perreux and A. Loupy, *Tetrahedron*, 2001, **57**, 9199-9223.

24. R. S. Varma, *Green Chemistry*, 1999, **1**, 43-55.

25. U. A. A. Mirza, John Wiley & Sons, 2011, pp. 213-229.

26. D. J. Varughese, M. S. Manhas and A. K. Bose, *Tetrahedron Lett.*, 2006, **47**, 6795-6797.

27. B. K. Banik, K. J. Barakat, D. R. Wagle, M. S. Manhas and A. K. Bose, *The Journal of Organic Chemistry*, 1999, **64**, 5746-5753.

28. C. O. Kappe and D. Doris, *Nature Reviews Drug Discovery*, 2005, **5**, 51-63.

29. A. Stambouli, M. Chastrette and M. Soufiaoui, *Tetrahedron Lett.*, 1991, **32**, 1723.

30. R. Laurent, A. Laporterie, J. Dubac and J. Berlan, *Organometallics*, 1994, **13**, 2493-2495.

31. F. Adámek and M. Hájek, *Tetrahedron Lett.*, 1992, **33**, 2039-2042.

32. R. N. Gedye, W. Rank and K. C. Westaway, *Can. J. Chem.*, 1991, **69**, 706-711.

33. G. B. Jones and B. J. Chapman, *The Journal of Organic Chemistry*, 1993, **58**, 5558-5559.

34. R. Gedye, F. Smith, K. Westaway, H. Ali, L. Baldisera, L. Laberge and J. Rousell, *Tetrahedron Lett.*, 1986, **27**, 279-282.

35. J. F. Watts and J. Wolstenholme, *An introduction to surface analysis by XPS and AES*, J. Wiley, New York, NY, 2003.

36. D. Briggs and J. T. Grant, *Surface Analysis by Auger and X-Ray Photoelectron Spectroscopy*, IM Publications, 2003.

37. J. W. Hall, N. Membreno, J. Wu, H. Celio, R. A. Jones and K. J. Stevenson, *J. Am. Chem. Soc.*, 2012, **134**, 5532-5535.

38. B. Scrosati, *Nat Nano*, 2007, **2**, 598-599.

Chapter 2: Trimethylphosphine Pyrazolate Ruthenium Complexes

2.1: INTRODUCTION

2.1.1: Overview

The objectives of the work described in this chapter were to synthesize new volatile ruthenium complexes and assess their viability as CVD precursors for the deposition of ruthenium and ruthenium phosphorus alloys. The use of ligands that are known to impart volatility such as trimethylphosphine (PMe_3) and bis(trifluoromethyl)pyrazolate (3,5-$(CF_3)_2$-Pz) can yield complexes that show promise as CVD precursors. In this chapter, the chemistry of ruthenium has been explored with these ligands using conventional synthetic methods as well as introducing the use of microwave energy to isolate several new complexes that have promise as CVD precursors.

2.1.2: Ruthenium Thin Films

Physical vapor deposition (PVD) and CVD processes are both methods of growing thin films using the elements or organometallic complexes of metals. PVD requires sophisticated vacuum systems and extreme inputs of heat or energy compared to the appeal of mild conditions using CVD. CVD methods can also allow for the selective growth of films of different depths and compositions compared to the techniques using PVD.[1-3] Thin films of ruthenium are used for DRAM memory devices and seed layers, acting as a glue layer for copper.[4] RuO_2 is conductive, meaning that oxygen diffusion in the film will not affect the properties of a device.[5]

Reaction of Ru_3CO_{12} with three equivalents of 3,5-bis(trifluoromethyl)pyrazole (HPz-CF_3) at 180 ° yields the double pyrazolate-bridged Ru(I) complex [$Ru(CO)_3$(μ-Pz-CF_3)]$_2$ (**2-I**) (Scheme II-1). In 2003 Carty published the synthesis and characterization of this complex and reported its use as a CVD precursor. Using O_2 and H_2 as carrier gasses

films of RuO_2 and Ru were obtained in the deposition temperature range 300—450 ^{0}C, at 10 sccm, and under a pressure of 1.5 torr.[6]

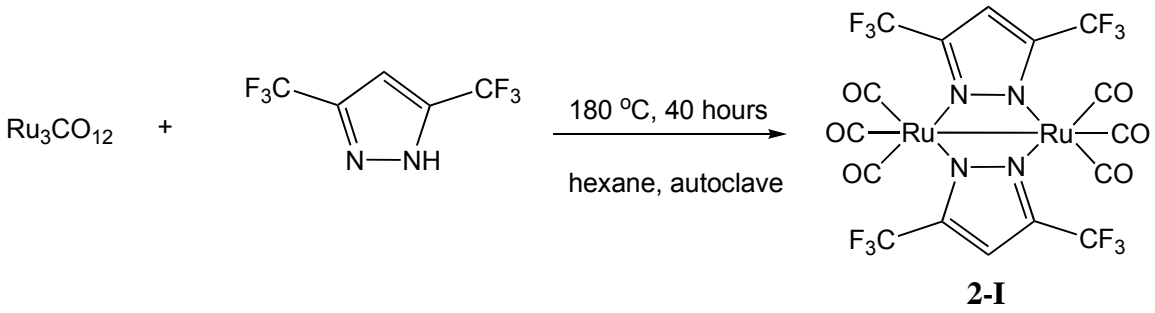

2-I

Scheme II-1: Synthesis of $[Ru(CO)_3(\mu\text{-}Pz\text{-}CF_3)]_2$ (**2-I**).

The suitability of **2-I** for the growth of Ru-containing thin films gains its advantage from the CF_3 groups on the bridging pyrazolate ligands, thus **2-I** sublimes readily at 70 ^{0}C at 200 mtorr. Crystalline films were obtained giving columnar-type microstructures as seen in Figure II-1.

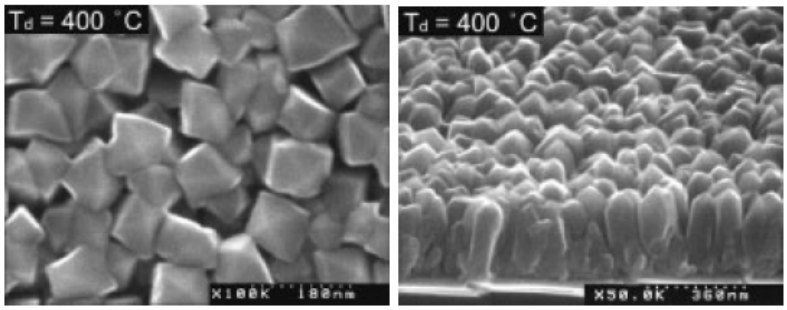

Figure II-1: Top and cross-sectional view SEM micrographs of Ru films deposited under H_2 using **2-I** as the precursor.[6]

Clearly complex **2-I** serves as a good starting point for developing the chemistry of CVD precursors which have the potential to deposit thin films of RuP alloys. The replacement of one or more CO ligands with suitable phosphine ligands such as PMe_3 should produce a volatile single source CVD precursor which can be used to deposit thin films containing both Ru and P. Complex **2-I** yields films of polycrystalline character. It

has been shown previously that the presence of PMe_3 in Ru containing molecules can lead to the CVD growth of amorphous films of RuP.[7] The work described in this chapter is focused on the synthesis, structures, and characterization of PMe_3 derivatives of **2-I** as well as film growth and characterization studies.

2.2: RESULTS AND DISCUSSION

Initial studies showed that **2-I** is an air stable crystalline solid and is fairly resistant to CO replacement with PMe_3 under thermal conditions. However the use of microwave energy under a variety of different conditions enabled the synthesis of a number of new PMe_3 pyrazolate Ru complexes as illustrated in Scheme II-2.

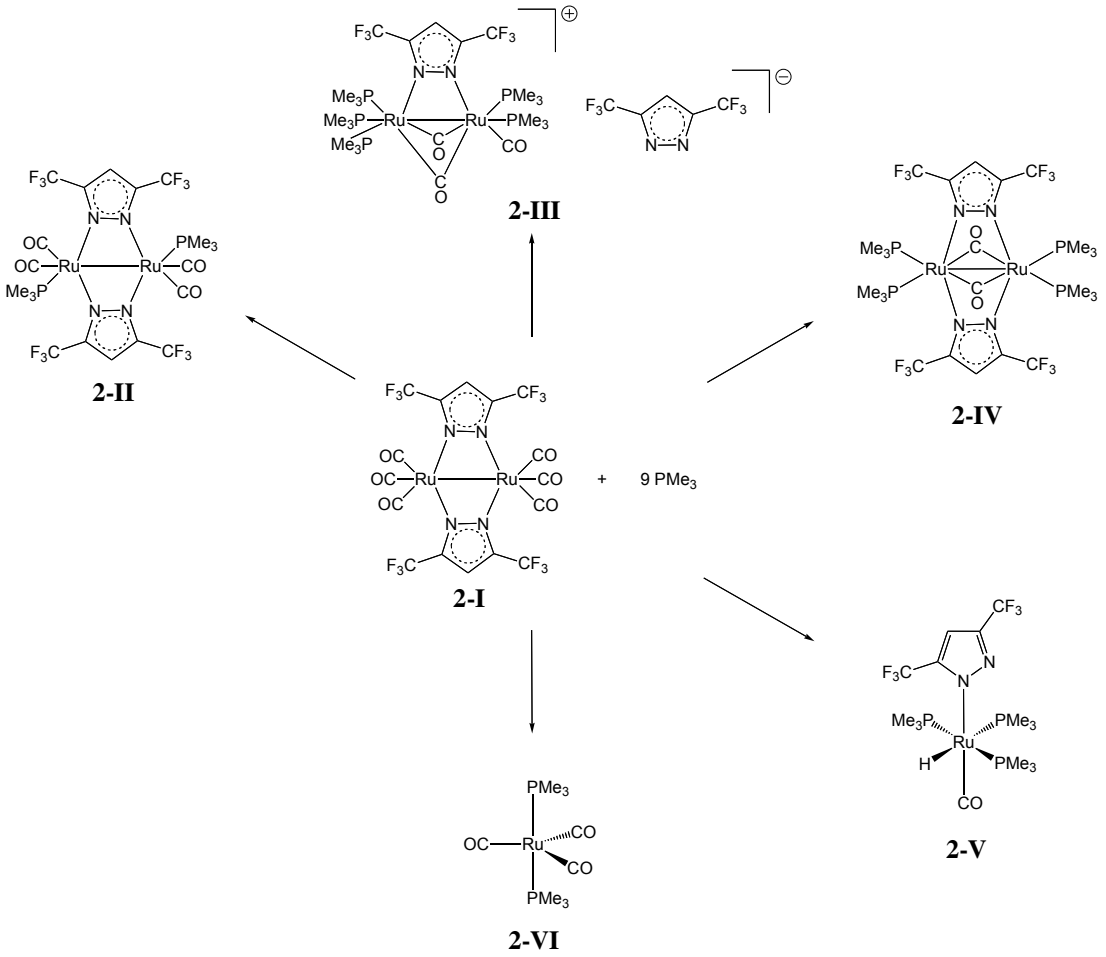

Scheme II-2: PMe_3 pyrazolate complexes of Ru produced via microwave synthesis.

2.2.1: Synthesis of Ruthenium Pyrazolate and Trimethylphosphine Compounds via Microwave Energy

Attempts at CO substitution reactions with PMe_3 in **2-I** using thermal procedures did not prove fruitful. Treating **2-I** with UV light in a quartz reaction vessel in various solvents and concentrations also yielded starting materials. These observations are consistent with CO acting as a very good π-acid ligand to low valent Ru. Therefore more aggressive conditions were selected in order to replace one or more CO groups. Microwave (MW) procedures are useful for the acceleration of chemical reactions,[8, 9] decrease in degradation of product,[10] and are environmentally friendly by reducing the use of solvents.[11] Microwave enhanced chemical synthesis of metal complexes is well known for Mn, Fe, as well as Ru in the current literature.[12-15]

In an airtight microwave tube complex **2-I** and nine equivalents of PMe_3 were dissolved in 5 mL of toluene. Using the efficiency of microwave energy complexes **2-II—2-VI** were isolated from the same reaction mixture under different conditions of time, temperature, and power as shown in Table II-1. As the three variables were increased the formation of Ru dinuclear complexes **2-II—2-IV** were isolated which reflect an increase in the number of CO ligands replaced with PMe_3. It is interesting to note that while leaving the temperature and reaction time the same by increasing the power from 80 W to 225 W one 3,5-CF_3-Pz was displaced forming a non-coordinatng anion (**2-III**). Once the temperatures were increased from 105 ^{0}C to 150 ^{0}C the loss of bridging 3,5-CF_3-Pz was observed yielding the mononuclear complex **2-V.** Upon increasing the temperature to 180 ^{0}C loss of 3,5-CF_3-Pz occurred completely yielding complex **2-VI**.

Table II-1: Microwave conditions for the synthesis of **2-II—2-VI.**

Complex	Time (minutes)	Temperature	Power	Result
2-II	30	105 ^{0}C	80 W	Coordination of 2 PMe_3's
2-III	30	105 ^{0}C	225 W	Coordination of 5 PMe_3's; salt formation
2-IV	60	105 ^{0}C	250 W	Coordination of 4 PMe_3's
2-V	60	150 ^{0}C	250 W	Coordination of 3 PMe_3's; mononuclear species
2-VI	60	180 ^{0}C	300 W	Coordination of 2 PMe_3's; mononuclear species, loss of 3,5-(CF_3)-Pz

$[Ru(CO)_2(3,5\text{-}(CF_3)_2\text{-}pz)(PMe_3)]_2$ (2-II). In an attempt to replace CO with PMe_3, complex **2-I** was dissolved in toluene and reacted with six equivalents of PMe_3 and refluxed at 130 ^{0}C for 18 hours. The reaction mixture turned a bright yellow. Solvent was removed and the yellow residue was dissolved in a minimal amount of hexane from which a crop of **2-II** could be obtained as yellow X-ray quality crystals by cooling to -35 ^{0}C (87 % yield). This compound can also be synthesized using microwave energy at a lower temperature of 105 ^{0}C and reaction time of 30 minutes as shown in Table II-1. **2-II** was tested for volatility in a sealed tube under vacuum (0.1 torr) and found to sublime without melting at 170 ^{0}C.

The ^{1}H NMR spectrum of **2-II** in $CDCl_3$ is consistent with the solid state structure and contains a doublet for the PMe_3 hydrogens centered at 1.35 ppm and a singlet for the 3,5-$(CF_3)_2$-pz hydrogen at 6.68 ppm. The $^{31}P\{^1H\}$ spectrum contains a singlet for the two equivalent PMe_3 groups at 8.88 ppm. The ^{19}F NMR spectrum contains two doublets at -59.27 ppm ($^2J_{F\text{-}P}$ = 2.26 Hz) and -59.84 ppm ($^2J_{F\text{-}P}$ = 2.63 Hz).

Complex **2-II** crystallizes in the monoclinic space group $P2_1/n$ with four molecules per unit cell. Figure II-2 shows the molecular geometry and atom numbering scheme. Crystallographic details are given in Table II-4 and key bond lengths and angles are given in Table II-6. The overall molecular structure of **2-II** is isoelectronic with **2-I** having two Ru(I) centers and a single Ru-Ru metal bond giving each Ru an electron count of 18.

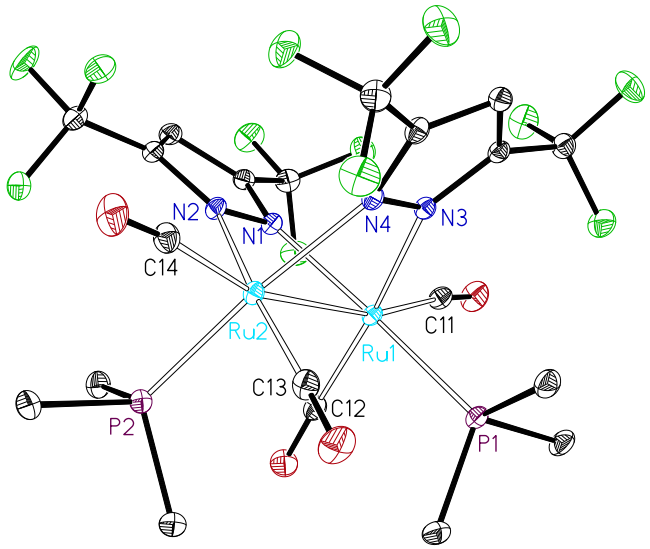

Figure II-2: ORTEP view of **2-II** with partial atom numbering scheme. Ellipsoids are drawn at 30% probability level. Hydrogen atoms are omitted for clarity.

The Ru(1)-Ru(2), Ru(2)-N(2), N(1)-N(2) bond lengths of **2-II** are 2.796(7) Å, 2.141(2) Å, and 1.346(3) Å, respectively, which can be compared with the Ru(1)-Ru(2), Ru(1)-N(2), N(1)-(N2) bond lengths 2.712 Å, 2.122 Å, and 1.340 Å of complex **2-I**. Complex **2-II** has a Ru(1)-P(1) bond length of 2.3235 Å. Each Ru has a distorted octahedral geometry as the C(13)-Ru(2)-N(2) bond angle is $169.20(10)^0$ while the C(13)-Ru(2)-C(14) bond angle of $91.59(12)^0$ is near ideal for octahedral geometry.

[Ru(PMe$_3$)$_3$(μ-CO)$_2$(μ-(3,5-(CF$_3$)-pz)Ru(PMe$_3$)$_2$CO)][3,5-(CF$_3$)-pz] (2-III). By increasing the power of the MW reaction and leaving the time and temperatures the same another compound was isolated from the reaction of [Ru(CO)$_3$(3,5-(CF$_3$)$_2$-pz)]$_2$ with nine equivalents of PMe$_3$. Using toluene as the solvent in a microwave tube at 105 ^{0}C and reaction time of 30 minutes, as shown in Table II-1, gave a crop of orange/red crystals of **2-**III in 15% yield. This complex was tested for volatility in a sealed tube under vacuum (0.1 torr) and found to sublime without decomposition at 100 ^{0}C.

The ^{1}H NMR spectrum of **2-III** in d$_6$-acetone is consistent with the solid state structure (Figure II-3) and contains two singlets for the non coordinating anionic 3,5-(CF$_3$)$_2$-Pz hydrogen at 6.2 ppm and the bridging 3,5-(CF$_3$)$_2$-Pz hydrogen at 6.95 ppm. The PMe$_3$ hydrogens appear as a multiplet at 1-1.8 ppm. The ^{31}P{^{1}H} spectrum contains singlets at 10.1 ppm, 8.7 ppm, and 3.8 ppm.

One bridging 3,5-(CF$_3$)$_2$-Pz has dissociated from **2-III** to form a non-coordinating anion and two CO groups are now bridging the two Ru centers. Three CO groups have been displaced. One Ru bears three PMe$_3$ groups and the other bears two PMe$_3$ groups with one CO ligand. Both are formally Ru(I) with the charges balanced by the bridging 3,5-(CF$_3$)$_2$-Pz and the non-coordinating 3,5-(CF$_3$)$_2$-Pz anion. Complex **2-III** crystallizes in the triclinic space group *P1* with 2 molecules per unit cell. Figure II-3 shows the molecular geometry and atom numbering scheme. Crystallographic details are given in Table II-4 and key bond lengths and angles are given in Table II-7. With the displacement of one 3,5-(CF$_3$)$_2$-Pz and the presence of two bridging CO ligands the Ru(1)-Ru(2) bond distance is 2.776(3) Å, which is still close to that of **2-I** and **2-II**. The two μ-CO ligands are not equidistant between Ru(1) and Ru(2) with bond lengths of 2.15(3) Å and 2.04(2) Å for Ru(1)-C(2) and Ru(2)-C(2), respectively, and a bond angle of 84.249(3)^0 for Ru(1)-C(2)-Ru(2). This distortion is no doubt due to the presence of an η^1-CO ligand and 2 PMe$_3$ groups on Ru(1) and 3 PMe$_3$ groups on Ru(2) making each Ru

differ electronically. The pyrazolate anion is fully dissociated in the solid state with the closest contact between the anion and the cation of 12.047(2) Å (F(3)-C(5)).

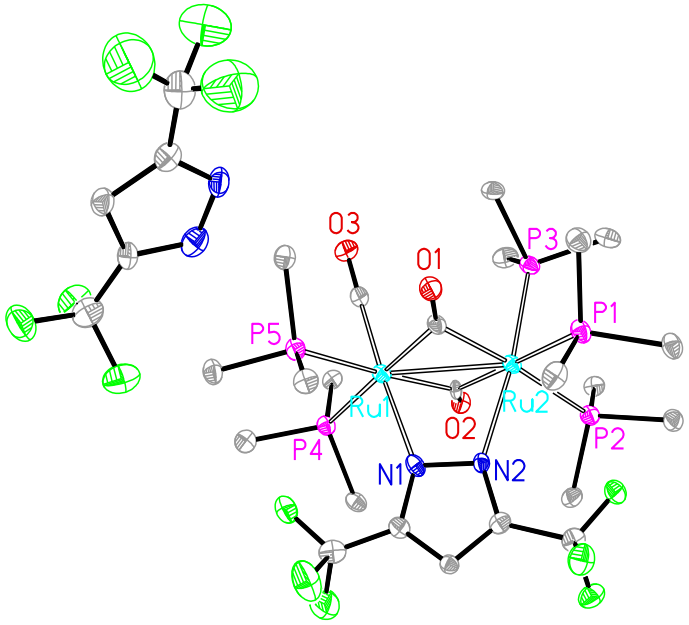

Figure II-3: ORTEP view of **2-III** with partial atom numbering scheme. Ellipsoids are drawn at 30% probability level. Hydrogen atoms are omitted for clarity.

[Ru(PMe$_3$)$_2$(μ-CO)(μ-(3,5-(CF$_3$)-Pz)]$_2$ (2-IV). In an attempt to displace more than three CO groups the reaction time was increased to 60 minutes and the power increased to 250 W but the temperature was maintained at 105 ^{0}C for the reaction of **2-I** with nine equivalents of PMe$_3$. These conditions yielded a mix of yellow and red crystals. The yellow crystals were determined by single crystal X-ray diffraction to be **2-II** (20 %) and the red were **2-IV** in 10 % yield.

The ^{1}H NMR spectrum of **2-IV** in CDCl$_3$ is consistent with the solid state structure (Figure II-4) and contains a multiplet for the PMe$_3$ hydrogens centered at 1.32 ppm and a singlet for the 3,5-(CF$_3$)$_2$-pz hydrogen at 6.65 ppm. The ^{31}P{^{1}H} spectrum contains a singlet at 9.1 ppm.

Complex **2-IV** crystallizes in the triclinic space group $P\bar{1}$ with 1 molecule per unit cell. Figure II-4 shows the molecular geometry and atom numbering scheme.

Crystallographic details are given in Table II-4 and key bond lengths and angles are given in Table II-8. The overall molecular structure of **2-IV** is isoelectronic with **2-I** and **2-II** having two Ru(I) centers and a Ru-Ru metal bond giving each Ru 18 electrons. Complex **2-IV** has two bridging CO groups like **2-III** but is structurally different with each Ru having two PMe_3 groups while **2-III** has three PMe_3 groups coordinated to one Ru and two on the other Ru center. Complex **2-IV** is also unique because it has both 3,5-$(CF_3)_2$-pz's bridging between the two Ru. The Ru(1)-Ru(1A) distance is 2.775(5) Å. It is interesting to note that the 4 PMe_3 groups are co-planar, as are the two 3,5-$(CF_3)_2$-Pz groups.

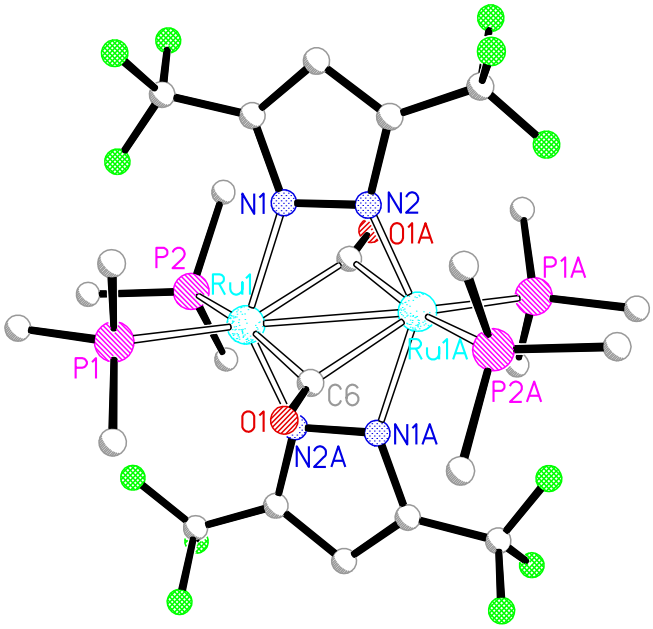

Figure II-4: ORTEP view of **2-IV** with partial atom numbering scheme. Ellipsoids are drawn at 30% probability level. Hydrogen atoms are omitted for clarity.

Ru(CO)(H)(3,5-(CF_3)-pz)$(PMe_3)_3$ (2-V). The reaction of **2-I** with nine equivalents of PMe_3 dissolved in toluene in a MW vessel with reaction time of 60 minutes, microwave power of 250 W, and an increased temperature of 150 ^{0}C yielded a mononuclear Ru complex, **2-V,** as colorless crystals in 10 % yield. Complex **2-V** has one bound 3,5-$(CF_3)_2$-pz, a CO ligand, three PMe_3 groups, and as detected by ^{1}H NMR, a Ru-

H (hydride). The increased harsher conditions result in a breakdown of the original dinuclear structure of **2-II**, and the Ru(I) centers have been oxidized to Ru(II), and several CO ligands have been replaced with PMe_3 (Table II-1).

The ^1H NMR spectrum of **2-V** in $CDCl_3$ is consistent with the solid state structure and contains a multiplet for the PMe_3 hydrogens at 1.4 ppm and a singlet for the 3,5-$(CF_3)_2$-pz hydrogen at 6.68 ppm. The Ru-*H* signal appears as a doublet of triplets of doublets (see Figure II-5) centered at -7.40 ppm. The $^{31}P\{^1H\}$ spectrum contains a triplet at 2.71 ppm ($^2J_{P\text{-}P}$ = 25.8 Hz) and a doublet at -2.81 ppm ($^2J_{P\text{-}P}$ = 28.2 Hz).

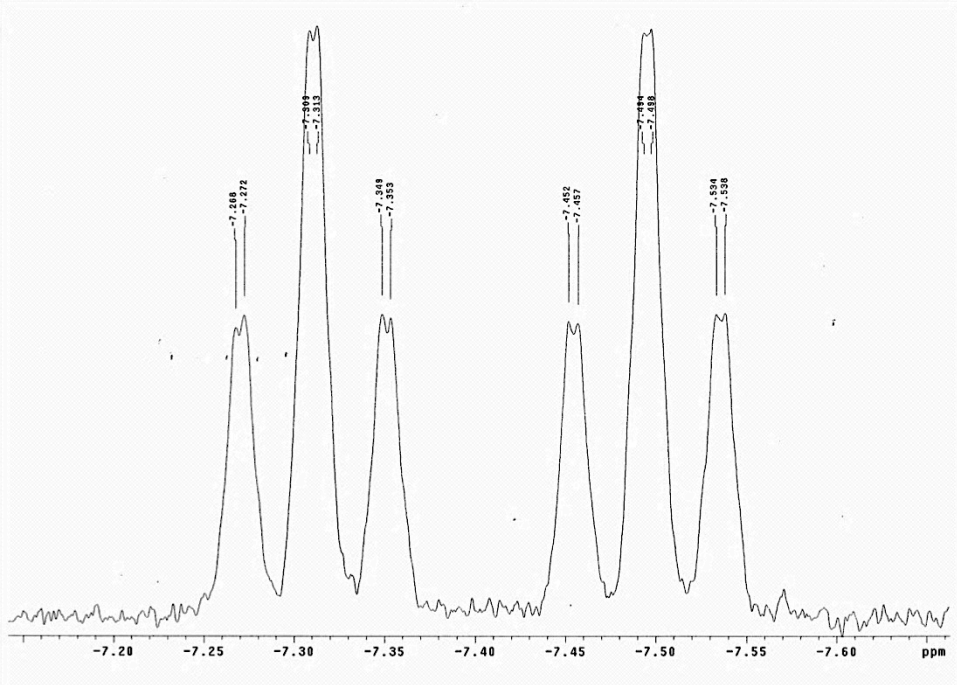

Figure II-5: ^1H NMR of **2-V** showing the doublet of triplets of doublets of the Ru-*H* at -7.40 ppm.

Based on simulation experiments of the Ru-*H*, the spectrum appears to be an AX_2Y spin system. This analysis gives a spectrum with $^2J_{P\text{-}Htrans}$ = 110.3 Hz and $^2J_{P\text{-}Hcis}$ = 23.9, $^2J_{P\text{-}H}$ = 2.4 (Figure II-6).

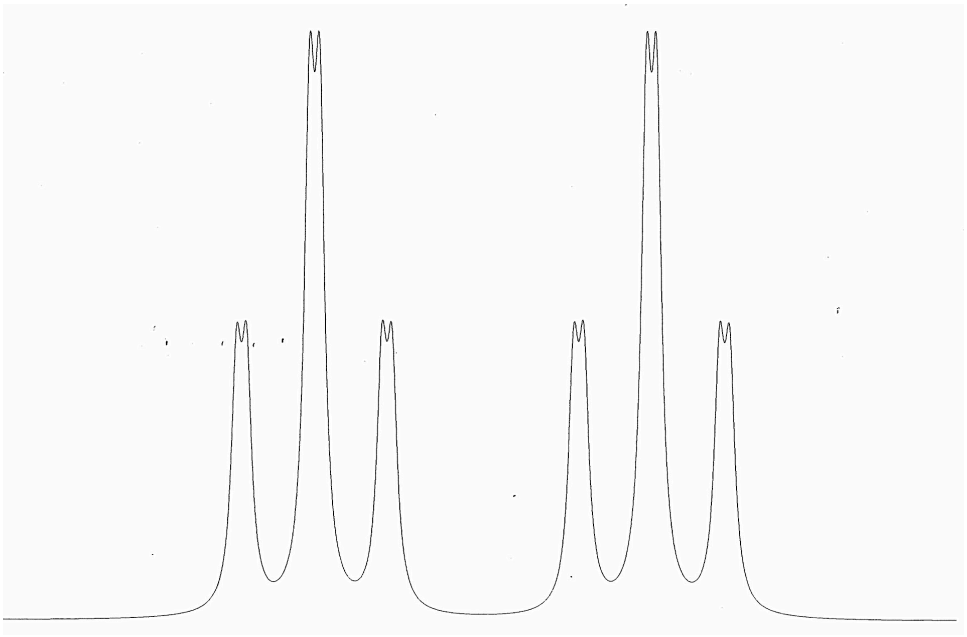

Figure II-6: Simulated spectrum of the Ru-*H* of **2-V** at -7.40 ppm.

Complex **2-V** crystallizes in the monoclinic space group $P2_1/n$ with 12 molecules per unit cell. Figure II-7 shows the molecular geometry and atom numbering scheme. Crystallographic details are given in Table II-4 and key bond lengths and angles are given in Table II-9. The Ru(1)-N(2) bond length is 2.087(3) Å which is considerably shorter than in complexes **2-I** through **2-IV** where the pyrazolates are bridging. The *trans* PMe_3 groups are bound with a significant deviation in the P-Ru-P angle from 180^0 to $167.5(3)^0$ (P(1)-Ru-P(3)).

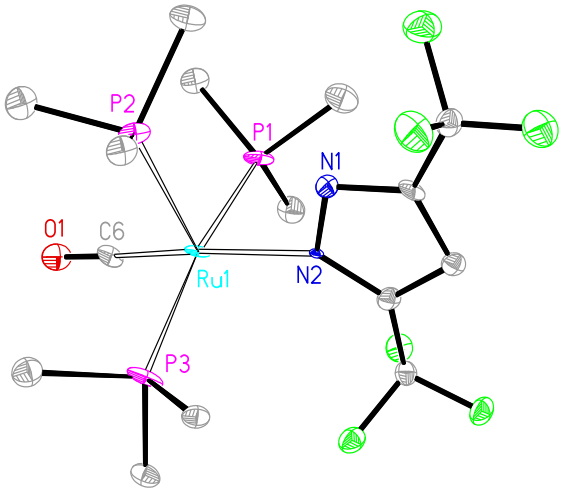

Figure II-7: ORTEP view of **2-V** with partial atom numbering scheme. Ellipsoids are drawn at 30% probability level. Hydrogen atoms are omitted for clarity.

***trans*-Ru(CO)$_3$(PMe$_3$)$_2$ (2-VI).** By further increasing the MW temperature and power to 180 ^{0}C and 300 W the reaction of **2-I** with nine equivalents of PMe$_3$ in toluene in 60 minutes, as shown in Table II-1, yielded **2-VI** as colorless crystals in 20 % yield. Complex **2-VI** has two PMe$_3$ groups, three CO ligands and no 3,5-(CF$_3$)$_2$-pz. Originally reported by Wilkinson in 1980, **2-VI** was synthesized via 6 atm CO at 60 ^{0}C from Ru$_2$(PMe$_3$)$_6$(μ-CH$_2$)$_3$ (see Figure II-8).[16]

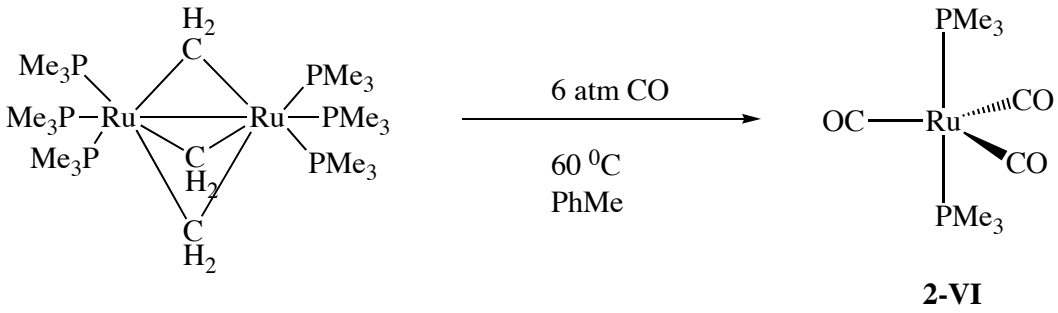

Figure II-8: 1980 synthesis of **2-VI** by Wilkinson using thermal methods.

Complex **2-VI** crystallizes in the orthorhombic space group *Pnma* with 4 molecules per unit cell. Figure II-9 shows the molecular geometry and atom numbering scheme. Crystallographic details are given in Table II-5 and key bond lengths and angles

are given in Table II-10**.** The Ru(1)-P(1) bond length of 2.332(3) Å is similar to the Ru-P bond lengths of **2-V**. The Ru(1)-C(1) bond length is 1.1912(4) Å which is slightly longer than the Ru(1)-C(6) bond length of 1.78(2) Å in **2-V**. The 3 CO ligands are bound with very nearly 120^0 between each other. Although it is interesting to note that upon increasing the severity of the MW conditions a known compound can be synthesized, complex **2-VI** was not screened as a CVD precursor due to the loss of the volatile ligand 3,5-$(CF_3)_2$-Pz and since it still has three CO groups coordinated to the Ru.

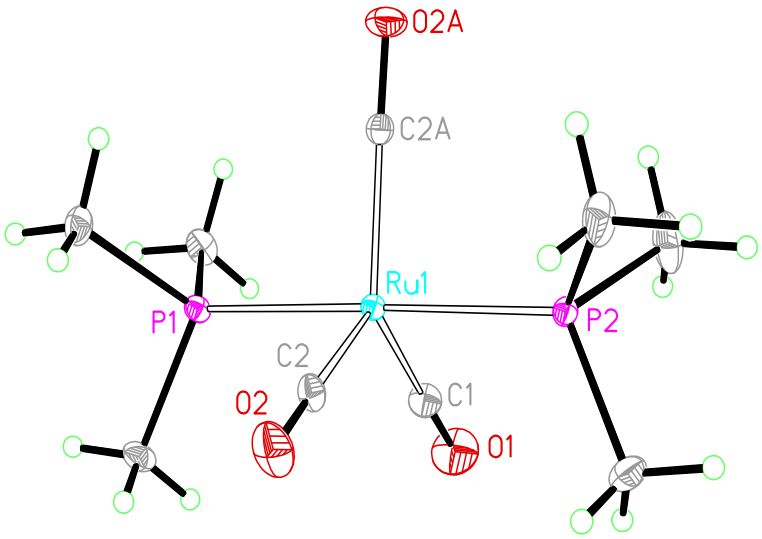

Figure II-9: ORTEP view of **2-VI** with partial atom numbering scheme. Ellipsoids are drawn at 30% probability level. Hydrogen atoms are omitted for clarity.

2.2.2: Synthesis of Ruthenium Pyrazolate and Trimethylphosphine Compounds via Thermal Methods

The synthetic route for the synthesis of **2-I** is to heat Ru_3CO_{12} in the presence of 3,5-$(CF_3)_2$-pz in an autoclave at 180 ^{0}C for 40 hours. To see if another pyrazolate ruthenium complex can be made without using the autoclave, Ru_3CO_{12} was dissolved in hexane along with 3,5-$(CF_3)_2$-pz and the mixture refluxed for 18 hours. This method produced **2-VII** (Scheme II-3) in 87 %.

Considering that a metal hydride was produced using MW conditions in the formation of **2-V** the logical step of treating **2-I** with a high pressure of H_2 in the presence of PMe_3 was attempted which indeed yielded another mononuclear Ru(II) hydride **2-VIII** (Scheme II-3).

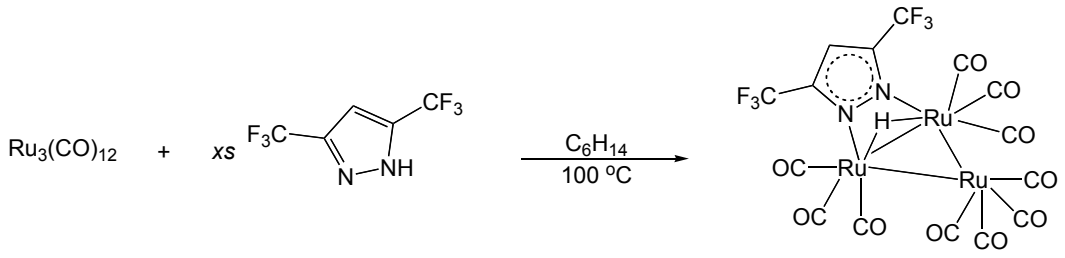

2-VII

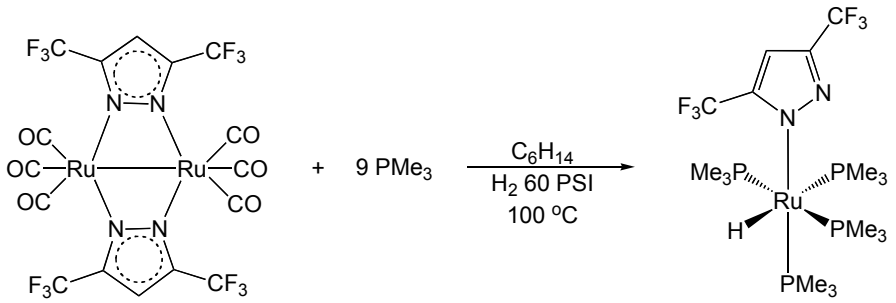

2-VIII

Scheme II-3: Synthetic route to ruthenium pyrazolate complexes **2-VII** and **2-VIII**.

$Ru_3(CO)_{10}(3,5\text{-}(CF_3)_2\text{-}Pz)(H)$ (2-VII). Reaction of $Ru_3(CO)_{12}$ with an excess of 3,5-$(CF_3)_2$-PzH in hexane at 100 ^{0}C affords an orange solution from which red-orange crystalline **2-VII** can be isolated in high yield (87 %). This complex was first reported by Wallis but its use as a CVD precursor was not explored.[17] Complex **2-VII** was tested for volatility in a sealed tube under vacuum (0.1 torr) and found to sublime without decomposing at 105 ^{0}C. Due to the presence of 10 CO's present in this compound attempts were made to replace CO with PMe_3. By refluxing in difference solvents, using

high pressures (40-80 atm) and high temperatures (100-250 ^{0}C) in an autoclave, and using MW reactions all attempts resulted in recovery of **2-VII** or decomposition.

Ru(H)(3,5-(CF$_3$)-Pz)(PMe$_3$)$_4$ (VIII). Complex **2-I** and nine equivalents of PMe_3 were dissolved in C_6H_{14} and transferred to a Fischer-Porter bottle equipped with a pressure gauge. Hydrogen (60 PSI) was introduced and the vessel was heated to 100 ^{0}C to give a dark yellow solution from which colorless crystalline **2-VIII** was isolated in low yield (9 %).

The ^{1}H NMR spectrum of **2-VIII** in $CDCl_3$ is consistent with the solid state structure and contains a multiplet for the PMe_3 hydrogens centered at 1.75 ppm and a singlet for the 3,5-$(CF_3)_2$-Pz hydrogen at 6.78 ppm. The Ru-*H* signal appears as a doublet of quartets centered at -9.55 ppm (figure II-10), which is similar to the multiplicity assigned to *cis*-$RuHCl(PMe_3)_4$ which the Ru-*H* appears at -8.50 ppm and appears as a doublet of quartets.[18] The $^{31}P\{^1H\}$ spectrum contains a doublet of triplets at 4.41 ppm ($^2J_{P\text{-}P}$ = 35.63 Hz), a doublet of triplets at -2.61 ppm ($^2J_{P\text{-}P}$ = 30.16 Hz), and a doublet of triplets at -8.13 ppm ($^2J_{P\text{-}P}$ = 30.91 Hz).

The Ru-*H* signal was simulated as an AXX'YZ spin system with $^2J_{P\text{-}H\textit{trans}}$ = 99.8 Hz, $^2J_{P\text{-}H\textit{cis}}$ = 23.5 Hz, and $^2J_{P\text{-}H\textit{cis(axial)}}$ = 24.8 Hz. As can be seen from a comparison between the experimental spectrum and the simulated spectrum (Figure II-11) further refinement is necessary.

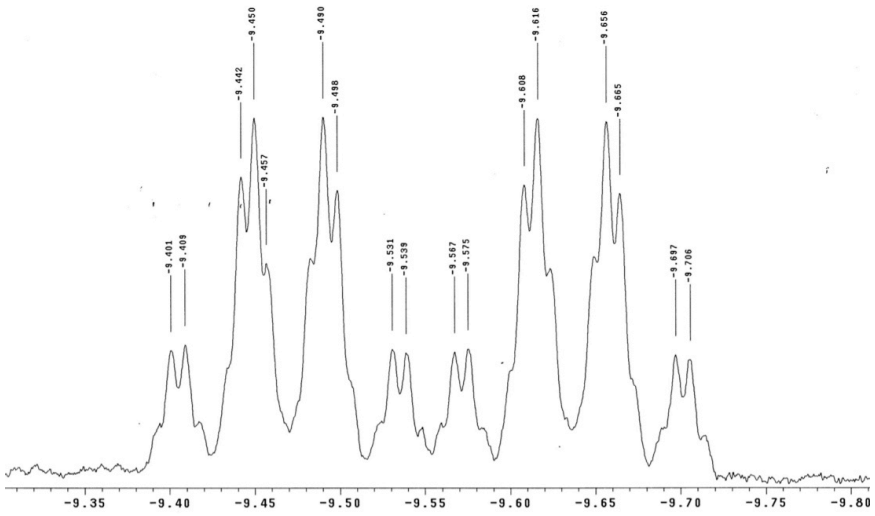

Figure II-10: ^{1}H NMR of **2-VIII** showing the doublet of quadruplets of the Ru-*H* at -9.55 ppm.

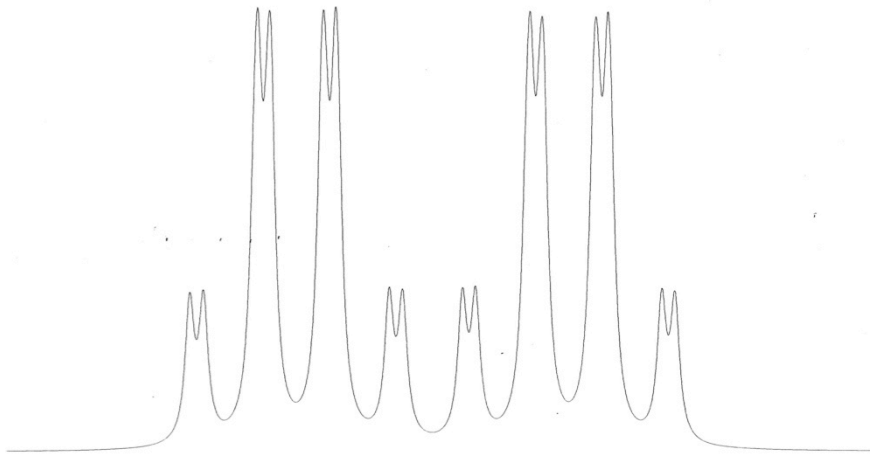

Figure II-11: Simulated spectrum of the Ru-*H* of **2-VIII** at -9.55 ppm

Complex **2-VIII** crystallizes in the orthrhombic space group *Pna2₁* with 4 molecules per unit cell. Figure II-12 shows the molecular geometry and atom numbering scheme. Crystallographic details are given in Table II-5 and key bond lengths and angles are given in Table II-11**.** The Ru(1)-N(1) bond length is 2.164(1) Å which is longer than the Ru(1)-N(2) bond length of 2.087(3) of **2-V**. In this case the 3,5-$(CF_3)_2$-Pz is *trans* to a PMe_3 while in **2-V** it is *trans* to a CO. The angle between the N(1)-Ru(1)-(P3) is 170.72(9)^0 and the angle between P(1)-Ru(1)-P(2) is 166.88(4)^0 which is not surprising for an asymmetric structure.

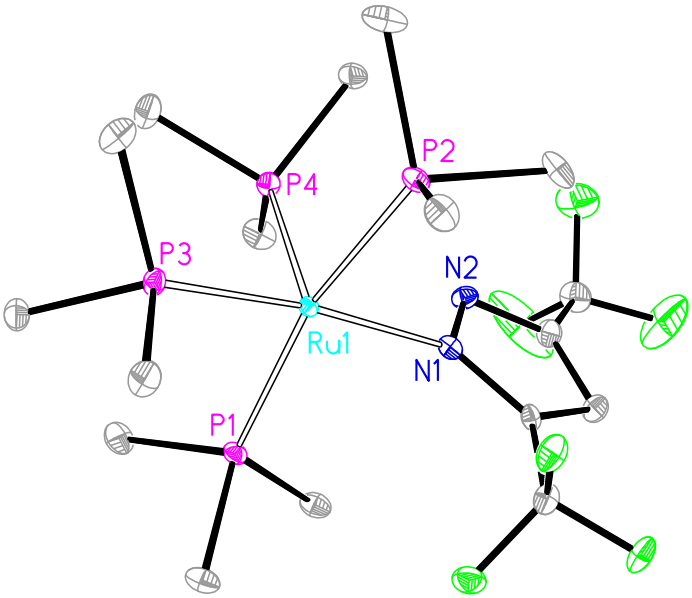

Figure II-12: ORTEP view of **2-VIII** with partial atom numbering scheme. Ellipsoids are drawn at 30% probability level. Hydrogen atoms are omitted for clarity.

2.2.3: Film Growth Studies

Complex **2-II** was used to grow a film on a SiO_2 substrate under argon at 170 ^{0}C with a deposition temperature of 400 ^{0}C giving a thickness of 2.4 μm (Table II-2). Films grown with **2-**II are a lustrous and metallic in appearance and resist scratching. A side angle view produced by SEM of this film displaying its amorphous character is shown in Figure II-13. XPS depth profiling of the film using Ar^+ shows a dramatic reduction of O

giving an overall composition of 98% Ru and 2 % O (Figure II-14). It can be seen that after 60 seconds of sputtering there are no further changes in film composition with further depth profiling.

Table II-2: Deposition conditions for **2-II**.

Carrier Gas	Sublimation Temperature	Deposition Temperature	Film Composition (at %) Ru	O
Ar	170 °C	400 °C	97.95	2.05

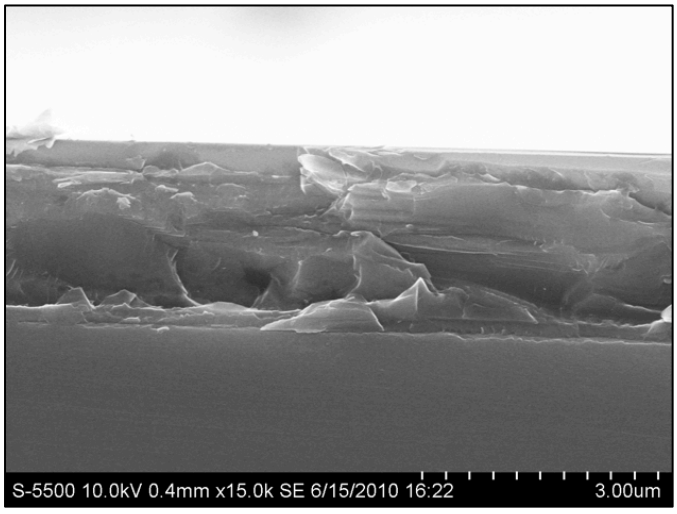

Figure II-13: SEM side angle view of a film deposited of a film grown from **2-II**.

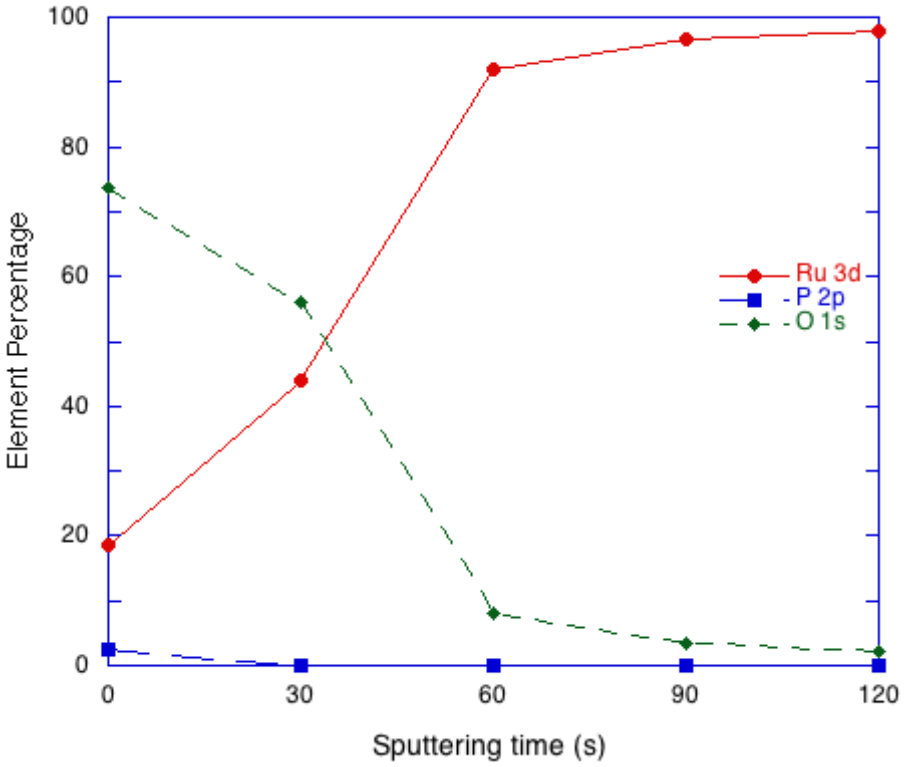

Figure II-14: XPS depth profiling of a film grown from **2-II**.

After analyzing each layer during sputtering the Ru 3d peak can be examined for the presence of one species. As seen in Figure II-15 the initial Ru 3d peaks are broad indicating more than one oxidation state of Ru is present, possibly indicating the presence of RuO_2 on the surface of the film. After subsequent removal of layers a relatively sharp Ru 3d peak is established. Due to the known overlap of the binding energy of the C 1s peak at 285 eV, it is estimated that the C content could not be detected accurately.

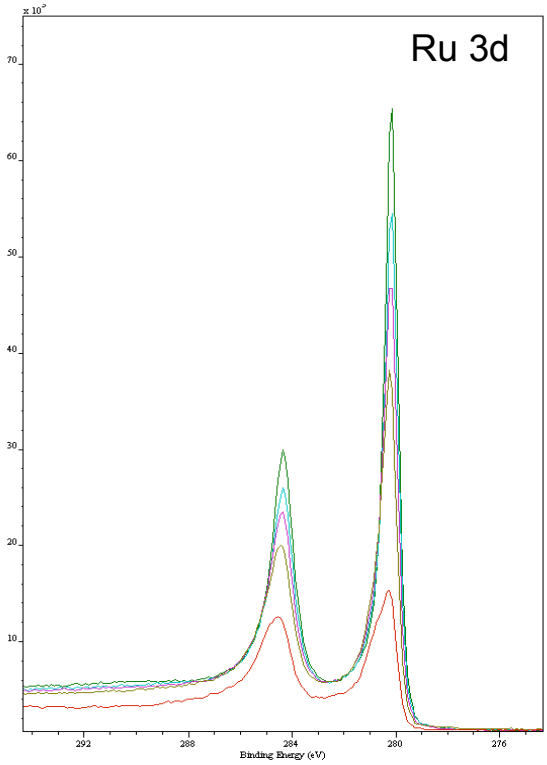

Figure II-15: XPS depth profiling of the Ru 3d peaks for a film grown from **2-II**.

On a SiO_2 substrate **2-III** was used to grow a film under argon at 100 ^{0}C with a deposition temperature of 400 ^{0}C giving a film thickness of 0.2 μm (Table II-3). A side angle SEM view of this film displaying its amorphous nature can be seen in Figure II-16. XPS depth profiling of this film using Ar^+ shows that after initial removal of surface contaminants via 30 seconds of sputtering the Ru film has an overall composition of 95% Ru and 5% O (Figure II-17).

Table II-3: Deposition conditions for **2-III**.

Carrier Gas	Sublimation Temperature	Deposition Temperature	Film Composition (%)	
			Ru	O
Ar	100 ^{0}C	400 ^{0}C	95.18	4.82

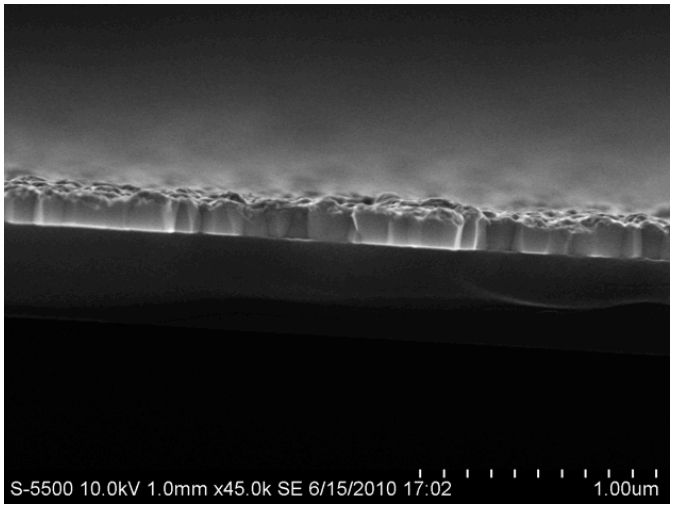

Figure II-16: SEM side angle view of a film grown from **2-III**.

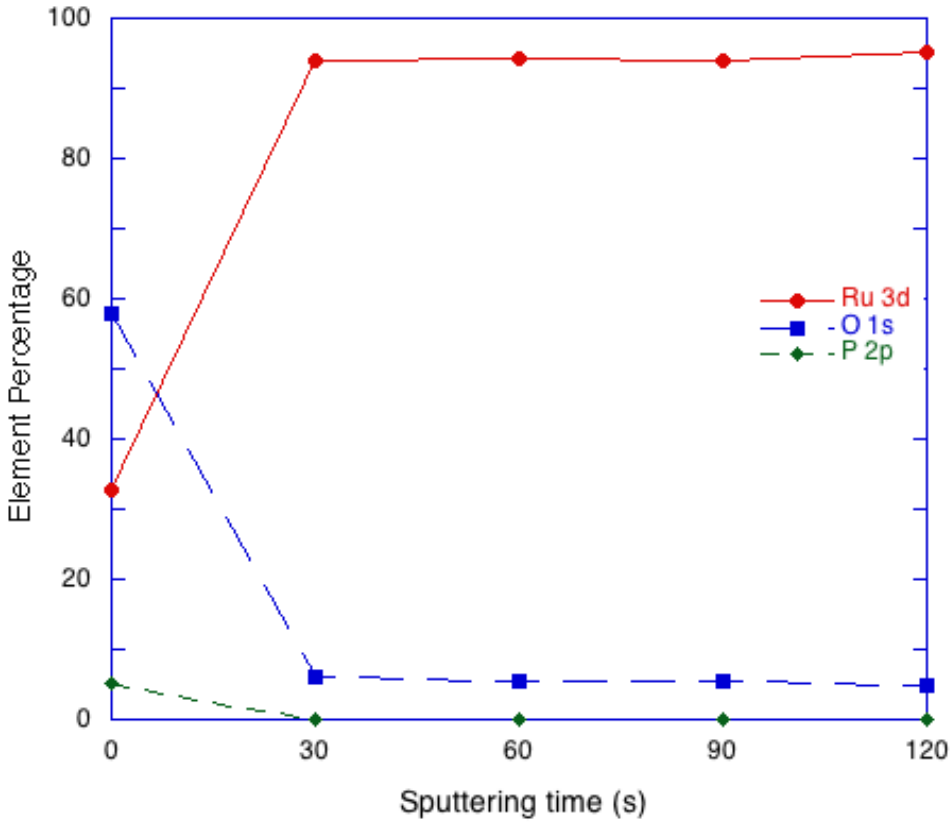

Figure II-17: XPS depth profiling of a film grown from **2-III**.

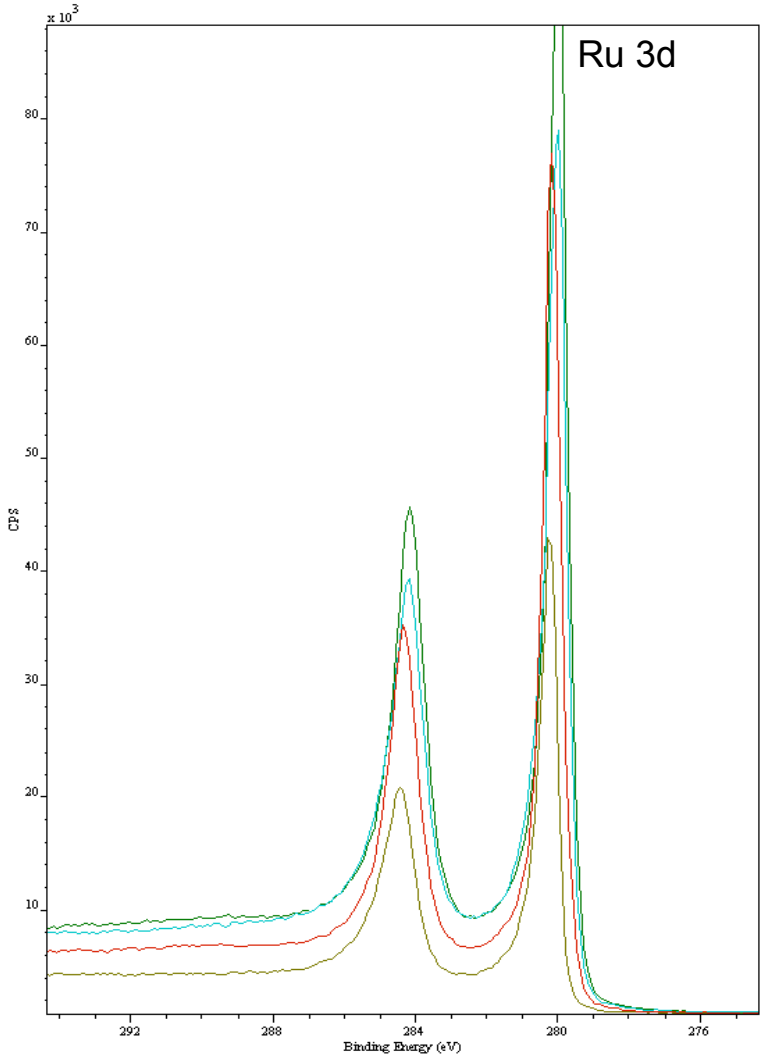

Figure II-18: XPS depth profiling of Ru 3d peaks of a film grown from **2-III**.

2.2.4: Future Studies

Although the exact mechanism(s) by which he precursor breaks down and films are formed are not known in detail it seems reasonable to assume that the pyrazolate

ligand would react with H_2 to form the volatile pyrazole, or might react further with it to produce volatile products that contaminate the films. This suggests that the as-deposited films from precursors grown under H_2 might contain lower amounts of carbon and oxygen impurities, due to the removal of intact pyrazole without ligand decomposition. Almost all of these complexes are highly moisture sensitive and the reaction vessel used for the MW reactions were not airtight. The use of a modified microwave for dry reactions would most likely produce higher yields of the compounds synthesized here.[19]

2.3: EXPERIMENTAL

2.3.1: General Synthesis

All reactions were performed under a dry, oxygen-free nitrogen atmosphere or under vacuum using standard Schlenk line and dry box techniques. Solvents were dried prior to use by distillation from sodium benzophenone ketyl anion under nitrogen. The compounds $[Ru(CO)_3(3,5\text{-}(CF_3)_2\text{-}Pz)]_2$,[6] 3,5-$(CF_3)_2$-pyrazole,[20] and $Ru_3(CO)_{10}(3,5\text{-}(CF_3)_2\text{-}Pz)(H)$ (**2-1**)[17] were prepared as previously described. Trimethylphosphine (97%), dihydrogen (99.996%) were purchased from Aldrich, PraxAir, and Linde and used without further purification.

2.3.2: Film Deposition Conditions

Films were grown in a homemade hot-wall CVD reactor consisting of a quartz deposition zone heated by a tube furnace. Films were deposited on native 400 nm SiO_2/Si(100) wafers. All fittings were VCR metal gasket face sealing connections with stainless steel lines. The precursor was heated in a Pyrex ampoule connected to the system and transported into the reactor using ultra-high purity argon (99.999%, Airgas) at flow rates of 5-15 sccm with a mass flow controller (Fathom Technologies, 0-50 sccm range). The lines were kept warm with insulated heating tape and wrapped with glass wool and heavy grade aluminum foil. The wafers were cut into approximately 3 mm x 5 mm pieces and positioned on quartz boats inside of the deposition zone. The system was

heated overnight under vacuum at pressures of 0.1 torr to remove the presence of water and oxygen.

2.3.3: Instrument Details

NMR spectra were recorded on a Varian 300 Unity Plus 300 MHz spectrometer (^{1}H, 300 MHz; ^{19}F, 282 MHz; ^{31}P, 121 MHz) at 25 °C. ^{1}H NMR signals are reported relative to residual proton resonances in deuterated solvents. ^{31}P NMR signals are reported relative to an external phosphoric acid standard. High-resolution mass spectra (HRMS) were obtained on a VG Analytical ZAB-VE sector instrument and are reported as *m*/*z* (relative intensity). Low-resolution chemical ionization (CI) mass spectra were collected on a Micromass Autospec Ultima mass spectrometer. Infrared spectra were recorded using a Nicolet IR 200 FTIR spectrometer using attenuated total reflectance (ATR). Melting points were obtained using an Electrothermal resistively heated melting point apparatus in sealed glass capillaries under a dinitrogen atmosphere or 0.1 torr vacuum. The microwave reactions were performed in a CEM discover reactor.

Film compositions were measured using *ex situ* high-resolution XPS analysis (Kratos AXIS Ultra DLD; monochromatic Al Kα). Depth profiling was achieved by sputtering the film with 4 kV Ar^{+}. The structural nature of the films were established by grazing angle ($2^{0} - 4^{0}$) X-ray diffraction (XRD) (Bruker-Nonius D8). Film thicknesses were determined using cross-sectioanl SEM (Hitachi S-5500 or Zeiss Supra 40 VP).

X-Ray diffractions studies were performed by Dr. Joseph Rivers and Dr. Xiaoping Yang. All crystals were mounted on a glass fiber. The data was collected on either a Nonius Kappa CCD diffractometer using a graphite monochromator with MoKα radiation (λ = 0.71073Å) at reduced temperature using an Oxford Cryostream low temperature device or a Rigaku AFC12 diffractometer with a Saturn 724+ CCD using a graphite monochromator with a MoKα radiation at reduced temperature using a Rigaku XStream low temperature device. Data reduction was performed with either DENZO-

SMN or Rigaku Americas Corporation's Crystal Clear version 1.40. The structures were solved by direct methods using SIR97 and refined by full-matrix least-squares on F^2 with anisotropic displacement parameters for the non-H atoms using SHELXL-97. The absolute configuration was assigned by internal comparison to the known absolute configuration of selected portions of the molecule. The hydrogen atoms on carbon were calculated in idealized positions with isotropic displacement parameters set to 1.2xUeq of the attached atom (1.5xUeq for methyl hydrogen atoms). Neutral atom scattering factors and values used to calculate the linear absorption coefficient are from the International Tables for X-ray Crystallography (1992). All figures were generated using SHELXTL/PC.

2.3.4: Synthesis of Complexes

$[Ru(CO)_2(3,5\text{-}(CF_3)_2\text{-}Pz)(PMe_3)]_2$ (2-II)

Method A: $[Ru(CO)_3(3,5\text{-}(CF_3)_2\text{-}Pz)]_2$ (1.00 g, 1.29 mmol) was dissolved in toluene (50 mL). PMe_3 (0.13 mL, 1.29 mmol) was added slowly via syringe and the reaction was stirred (18 h). The reaction mixture was concentrated under vacuum and cooled to -25 ^{0}C to give yellow crystals of **2-II** (0.82 g, 83 %) isolated yield.

Method B: $[Ru(CO)_3(3,5\text{-}(CF_3)_2\text{-}Pz)]_2$ (0.100 g, 0.129 mmol) was dissolved in 5 mL of anhydrous toluene and added to a microwave reaction tube. PMe_3 (0.118 mL, 1.16 mmol) was added via syringe. Microwave parameters: 105 ^{0}C, 30 minutes, 80 W. The solution was transferred to a Schlenk flask, solvent was removed *in vacuo* and the residue was dissolved in hexane, the solution filtered and cooled (-25 ^{0}C) to give yellow crystals of **2-II** (0.208 g, 87 %) isolated yield. m.p. 196-198 ^{0}C (1 atm N_2). 170 ^{0}C sublime (0.1 torr). ^{1}H NMR (300 MHz, $CDCl_3$, 27 ^{0}C) δ 6.68 (s, 2H), 1.35 (d, 18H, C*H*$_3$). $^{31}P\{^1H\}$ NMR (121 MHz, $CDCl_3$) δ 8.88 (s). ^{19}F NMR (282 MHz, $CDCl_3$) δ -59.27 (d, C*F*$_3$), -59.83 (d, C*F*$_3$). EI/MS *m/e*: 874 [M^+], 675 [-Pz]$^+$]. FTIR (ATR, cm^{-1}): 2925 (w), 2914

(vw), 1410 (m), 1286 (s), 1233 (s), 1124 (s), 1119 (s), 1014 (m), 972 (m), 849 (w), 744 (w), 702 (w).

[Ru(PMe$_3$)$_3$(μ-CO)$_2$(μ-(3,5-(CF$_3$)-Pz)Ru(PMe$_3$)$_2$CO)][3,5-(CF$_3$)-pz] (2-III)

[Ru(CO)$_3$(3,5-(CF$_3$)$_2$-Pz)]$_2$ (0.100 g, 0.129 mmol) was dissolved in anhydrous toluene (5 mL) and added to a microwave reaction tube. PMe$_3$ (0.118 mL, 1.16 mmol) was added via syringe. Microwave parameters: 105 ^{0}C, 30 minutes, 225 W. The solution was transferred to a Schlenk flask, solvent was removed *in vacuo* and the residue was dissolved in hexane, the solution filtered and cooled (-25 ^{0}C) to give orange crystals of **2-III** in 0.104 g (15 %) isolated yield. m.p. 126-128 ^{0}C (1 atm N$_2$). 100 ^{0}C sublime (0.1 torr). ^{1}H NMR (300 MHz, C$_3$D$_6$O 27 ^{0}C) δ 6.95 (s, 1H), 6.20 (s, 1H), 1-1.8 (m, 45H, C*H$_3$*). ^{31}P{^{1}H} NMR (121 MHz, C$_3$D$_6$O) δ 34.5 (s), 8.7 (s), 3.8 (s), 10.1 (s). EI/MS *m/e*: 1160 [M$^+$], 914 [-Pz]. FTIR (ATR, cm^{-1}): 2973 (w), 2903 (w), 1649 (w, br), 1499 (w), 1423 (w), 1339 (w), 1311 (w), 1287 (w), 1442 (m), 1130 (m), 1107 (s), 1000 (w), 977 (m), 935 (m), 841 (m), 790 (w), 714 (w).

[Ru(PMe$_3$)$_2$(μ-CO)(μ-(3,5-(CF$_3$)-Pz)]$_2$ (2-IV)

[Ru(CO)$_3$(3,5-(CF$_3$)$_2$-Pz)]$_2$ (0.100 g, 0.129 mmol) was dissolved in anhydrous toluene (5 mL) and added to a microwave reaction tube. PMe$_3$ (0.118 mL, 1.16 mmol) was added via syringe. Microwave parameters: 105 ^{0}C, 60 minutes, 250 W. The solution was transferred to a Schlenk flask, solvent was removed *in vacuo* and the residue was dissolved in hexane, the solution filtered and cooled (-25 ^{0}C) to give yellow crystals of **2-IV** in 0.013 g (10 %) isolated yield. m.p. 116-118 ^{0}C (1 atm N$_2$). ^{1}H NMR (300 MHz, CDCl$_3$, 27 ^{0}C) δ 6.65 (s, 1H), 1.32 (m, 36H. ^{31}P{^{1}H} NMR (121 MHz, C$_6$D$_6$) δ 9.1 (s, 2P), 8.9 (s, 2P). EI/MS *m/e*: 970 [M$^+$], 882 [-PMe$_3$] 690 [-Pz]. FTIR (ATR, cm^{-1}): 2920 (w), 1656 (s), 1530 (w), 1413 (m), 1330 (m), 1289 (w), 1215 (w), 1143 (w), 1114 (s), 1025 (m), 1008 (w), 953 (w), 862 (m), 841 (m), 759 (m).

Ru(CO)(H)(3,5-(CF_3)-Pz)(PMe_3)$_3$ (2-V)

[Ru(CO)$_3$(3,5-(CF_3)$_2$-Pz)]$_2$ (0.100 g, 0.129 mmol) was dissolved in 5 mL of anhydrous toluene and added to a microwave reaction tube. PMe_3 (0.118 mL, 1.16 mmol) was added via syringe. Microwave parameters: 150 ^{0}C, 60 minutes, 250 W. The solution was transferred to a Schlenk flask, solvent was removed *in vacuo* and the residue was dissolved in hexane, the solution filtered and cooled (-25 ^{0}C) to give colorless crystals of **2-V** in 0.010 g (10 %) isolated yield. m.p. 96-97 ^{0}C (1 atm N_2). ^{1}H NMR (600 MHz, $CDCl_3$, 27 ^{0}C) δ 6.68 (s, 1H, Pz-*H*), 1.41 (m, 27H, C*H*$_3$), -7.40 (dt, 1H, Ru*H*, $^2J_{P\text{-}Htrans}$ = 110.32 Hz, $^2J_{P\text{-}Hcis}$ = 23.86 Hz). ^{31}P{^{1}H} NMR (121 MHz, $CDCl_3$) δ 2.71 (s, 1P), 2.45 (s, 1P), -2.93 (s, 1P). EI/MS *m/e*: 562 [M$^+$], 486 [-PMe_3] 283 [-Pz]. FTIR (ATR, cm^{-1}): 2983 (w), 2908 (w), 1648 (w), 1520 (w), 1446 (w), 1331 (w), 1319 (w), 1287 (w), 1247 (m), 1138 (m), 1109 (s), 985 (m), 937 (s), 859 (m), 786 (m), 716 (m).

***trans*-Ru(CO)$_3$(PMe_3)$_2$ (2-VI)**

[Ru(CO)$_3$(3,5-(CF_3)$_2$-Pz)]$_2$ (0.100 g, 0.129 mmol) was dissolved in 5 mL anhydrous toluene and added to a microwave reaction tube. PMe_3 (0.118 mL, 1.16 mmol) was added via syringe. Microwave parameters: 180 ^{0}C, 60 minutes, 300 W. The solution was transferred to a Schlenk flask, solvent was removed *in vacuo* and the residue was dissolved in hexane, the solution filtered and cooled (-25 ^{0}C) to give colorless crystals of **2-VI** in 0.009 g (20 %) isolated yield. m.p. 89-92 ^{0}C (1 atm N_2). ^{1}H NMR (300 MHz, $CDCl_3$, 27 ^{0}C) δ 1.40 (m, 18H). ^{31}P{^{1}H} NMR (121 MHz, $CDCl_3$) δ (s, 1P). EI/MS *m/e*: 338 [M$^+$], 262 [-PMe_3], 234 [-CO]. FTIR (ATR, cm^{-1}): 1890 (vs), 1423 (s), 1304 (w), 1298 (s), 1115 (m), 947 (s), 860 (m), 680 (w), 587 (w), 490 (m), 463 (w).

Ru(H)(3,5-(CF_3)-Pz)(PMe_3)$_4$ (2-VIII)

[Ru(CO)$_3$(3,5-(CF_3)$_2$-Pz)]$_2$ (0.100 g, 0.129 mmol) was dissolved in hexane (30 mL). PMe_3 (0.118 mL, 1.16 mmol) was added via syringe. The reaction mixture was transferred to a Fisher-Porter bottle via cannula and was cooled to -78 ^{0}C. **2-I** was

introduced to an excess of hydrogen with the resultant pressure of 60 PSI. The flask was sealed, allowed to warm to room temperature, and heated to 100 ^{0}C for 12 hours. The excess hydrogen was removed under vacuum and the solution was transferred to a Schlenk flask, solvent was removed in vacuo and the residue was recrystallized from anhydrous hexane at -25 ^{0}C to give colorless crystals of **2-VI**. Isolated yield: 0.008 g, 9%. m.p. 120-123 ^{0}C (1 atm N_2). ^{1}H NMR (300 MHz, $CDCl_3$, 27 ^{0}C) δ 6.78 (s, 1H), 1.75 (m, 36H), -9.55 (dq, 1H). $^{31}P\{^1H\}$ NMR (121 MHz, $CDCl_3$) δ 4.41(dt, 1P, $^2J_{P\text{-}P}$ = 35.63 Hz), -2.61 ppm (dt, 2P, $^2J_{P\text{-}P}$ = 30.16 Hz), -8.13 ppm (dt, 2P, $^2J_{P\text{-}P}$ = 30.91 Hz). EI/MS *m/e*: 610 [M^+], 407 [-Pz], 331 [-PMe_3]. FTIR (ATR, cm^{-1}): 2902 (w), 1675 (w), 1530 (w), 1333 (w), 1280 (m), 1267 (m), 1210 (w), 1140 (w), 1108 (w), 987 (w), 876 (m), 852 (w), 767 (w).

2.4: APPENDIX

Table II-4: Crystal data and structure refinement for **2-II — 2-V**.

	2-II	**2-III**	**2-IV**	**2-V**
Empirical formula	$C_{20}H_{20}F_{12}N_4O_4P_2Ru_2$	$C_{28}H_{47}F_{12}N_4O_3P_5Ru_2$	$C_{24}H_{38}F_{12}N_4O_2P_4Ru_2$	$C_{15}H_{29}F_6N_2OP_3Ru$
Fw, g/mol	876.50	1159.87	968.60	562.39
Temperature, K	153(2)	153	293(2)	293(2)
Crystal system	Monoclinic	Triclinic	Triclinic	Monoclinic
Space group	$P2_1/n$	$P1$	$P\bar{1}$	$P2_1/n$
a, Å	15.604(3)	16.563(5)	9.694(5)	26.320(5)
b, Å	14.437(2)	17.354(4)	9.706(5)	9.968(2)
c, Å	15.868(3)	19.729(5)	14.736(5)	30.420(6)
α, deg	90	66.057(5)	75.948(5)	90
β, deg	92.86(3)	72.691(5)	87.872(5)	113.88(3)
γ, deg	90	70.314(4)	62.980(5)	90
V, Å^3	3570.2(12)	4794(2)	1193.9	7298(3)
Z	4	8	2	11
D_{calc}, g cm^{-3}	1.795	1.646	1.951	1.704
μ, mm^{-1}	1.037	0.759	0.935	0.833
F(000)	1904	2394	702	3753
θ range, deg	2.91 - 27.48	2.95 - 27.48	3.08 - 25.00	2.93 - 25.00
Reflections collected	8187	33515	6269	27826
Unique reflections	8146	6490	4111	12568
Reflections used	7832	20912	2073	8025
Restraints	0	324	182	504
Parameters	461	487	227	758
Goodness-of-fit	1.170	0.973	1.680	2.608
R[a] indices [I>2σ(I)]	R_1 = 0.0200	R_1 = 0.2093	R_1 = 0.1705	R_1 = 0.2556
	wR_2 = 0.0334	wR_2 = 0.2160	wR_2 = 0.3594	wR_2 = 0.5024
R[a] (all data)	R_1 = 0.0409	R_1 = 0.2675	R_1 = 0.2679	R_1 = 0.2978
	wR_2 = 0.0774	wR_2 = 0.3231	wR_2 = 0.3003	wR_2 = 0.5299

[a] $R_1 = \Sigma_{hkl} (|F_o|-|F_c|)/\Sigma_{hkl}|F_o|$, $R_2 = [\Sigma\, w(|F_o|-|F_c|)^2/\Sigma\, w|F_o|^2]^{1/2}$

Table II-5: Crystal data and structure refinement for **2-VI — 2-VIII**.

	2-VI	**2-VIII**
Empirical formula	$C_9H_{18}O_3P_2Ru$	$C_{17}H_{38}F_6N_2P_4Ru$
Fw, g/mol	340.28	609.45
Temperature, K	293(2)	293(2)
Crystal system	Orthorhombic	Orthorhombic
Space group	*Pnma*	*Pna2₁*
a, Å	10.049(2)	18.162(4)
b, Å	10.535(2)	15.540(3)
c, Å	13.942(3)	9.5868(19)
α, deg	90	90
β, deg	90	90
γ, deg	90	90
V, Å^3	1476.0(5)	2705.7(9)
Z	4	5
D_{calc}, g cm^{-3}	1.603	4.163
μ, mm^{-1}	0.635	4.651
F(000)	726	3215
θ range, deg	3.16- 27.48	3.36 - 25.00
Reflections collected	19957	12110
Unique reflections	1782	3716
Reflections used	1694	3698
Restraints	0	1
Parameters	79	271
Goodness-of-fit	0.697	0.863
R[a] indices [$I>2\sigma(I)$]	$R_1 = 0.0204$	$R_1 = 0.0248$
	$wR_2 = 0.0593$	$wR_2 = 0.0876$
R[a] (all data)	$R_1 = 0.0223$	$R_1 = 0.0249$
	$wR_2 = 0.0611$	$wR_2 = 0.0882$

[a] $R_1 = \Sigma_{hkl} (|F_o|-|F_c|)/\Sigma_{hkl}|F_o|$, $R_2 = [\Sigma\, w(|F_o|-|F_c|)^2/\Sigma\, w|F_o|^2]^{1/2}$

Table II-6: Selected Bond Lengths (Å) and Angles (°) for **2-II**.

Bond Lengths (Å)	
Ru(2)-Ru(1)	2.7958(7)
Ru(2)-N(2)	2.141(2)
Ru(1)-P(1)	2.3235(8)
N(2)-N(1)	1.346(3)
Ru(2)-C(14)	1.854(3)
Ru(2)-C(13)	1.951(3)
Bond Angles (°)	
C(14)-Ru(2)-C(13)	91.59(12)
C(13)-Ru(2)-N(2)	169.20(10)
C(14)-Ru(2)-N(2)	99.21(10)
N(2)-Ru(2)-N(4)	85.03(7)
C(14)-Ru(2)-P(2)	88.75(8)
C(13)-Ru(2)-P(2)	91.00(8)

Table II-7: Selected Bond Lengths (Å) and Angles (°) for **2-III**.

Bond Lengths (Å)	
Ru(1)-Ru(2)	2.776(3)
Ru(1)-C(2)	2.150(3)
Ru(2)-C(2)	2.040(2)
Ru(1)-N(1)	2.27(13)
Ru(2)-N(2)	2.28(15)
Ru(1)-P(4)	2.393(7)
Ru(1)-P(5)	2.439(8)
Ru(1)-C(3)	1.804(2)
Ru(2)-P(1)	2.270(7)
Ru(2)-P(2)	2.429(9)
Ru(2)-P(3)	2.448(6)
Bond Angles (°)	
C(3)-Ru(1)-N(1)	176.4(11)
P(4)-Ru(1)-C(3)	85.5(7)
P(4)-Ru(1)-C(1)	175.2(8)
C(3)-Ru(1)-Ru(2)	104.4(9)
C(1)-Ru(1)-Ru(2)	46.8(7)
N(1)-Ru(1)-Ru(2)	72.0(5)
C(1)-Ru(2)-C(2)	96.8(10)
N(1)-N(2)-Ru(2)	108.3(9)
Ru(1)-C(2)-Ru(2)	84.24(3)

Table II-8: Selected Bond Lengths (Å) and Angles (°) for **2-IV**.

Bond Lengths (Å)	
Ru(1)-Ru(1A)	2.775(5)
Ru(1)-N(1)	2.206(3)
Ru(1)-P(1)	2.436(4)
Ru(1)-P(2)	2.403(4)
Ru(1)-C(1)	2.162(5)
Ru(1)-N(2A)	2.092(2)
Bond Angles (°)	
N(1)-Ru(1)-N(2A)	127.24(9)
N(1)-Ru(1)-Ru(1A)	69.21(7)
C(1)-Ru(1)-C(2)	99.67(4)
P(1)-Ru(1)-P(2)	101.51(3)
P(1)-Ru(1)-Ru(1A)	129.58(5)
P(2)-Ru(1)-Ru(1A)	127.81(4)

Table II-9: Selected Bond Lengths (Å) and Angles (°) for **2-V**.

Bond Lengths (Å)	
Ru(1)-N(2)	2.087(3)
Ru(1)-P(1)	2.399(7)
Ru(1)-P(2)	2.477(7)
Ru(1)-P(3)	2.347(6)
Ru(1)-C(6)	1.78(2)
Bond Angles (°)	
C(6)-Ru(1)-N(2)	174.2(10)
Ru(1)-N(2)-N(1)	112.6(12)
P(1)-Ru(1)-P(2)	98.9(2)
P(1)-Ru(1)-P(3)	167.5(3)
P(2)-Ru(1)-P(3)	93.6(2)

Table II-10: Selected Bond Lengths (Å) and Angles (°) for **2-VI**.

Bond Lengths (Å)	
Ru(1)-P(1)	2.332(3)
Ru(1)-P(2)	2.341(7)
Ru(1)-C(1)	1.1912(4)
Bond Angles (°)	
P(1)-Ru(1)-P(2)	177.32(5)
C(1)-Ru(1)-C(2)	119.52(2)
C(2)-Ru(1)-C(3)	120.22(1)
C(3)Ru(1)-C(1)	120.22(1)
P(1)-Ru(1)-C(1)	88.68(4)

Table II-11: Selected Bond Lengths (Å) and Angles (°) for **2-VIII**.

Bond Lengths (Å)	
Ru(1)-N(1)	2.164(1)
Ru(1)-P(1)	2.333(3)
Ru(1)-P(2)	2.337(3)
Ru(1)-P(3)	2.281(4)
Ru(1)-P(4)	2.407(2)
Bond Angles (°)	
N(2)-Ru(1)-P(3)	170.72(9)
P(1)-Ru(1)-P(2)	166.88(4)
P(1)-Ru(1)-P(4)	96.91(1)
P(4)-Ru(1)-P(2)	94.42(2)
P(3)-Ru(1)-P(4)	99.50(3)

2.5: REFERENCES

1. M. J. Hampden-Smith and T. T. Kodas, *The Chemistry of Metal CVD*, 1994.

2. I. K. Igumenov, N. V. Gelfond, N. B. Morozova and H. Nizard, *Chemical Vapor Deposition*, 2007, **13**, 633-637.

3. E. L. Crane, Y. You, R. G. Nuzzo and G. S. Girolami, *J. Am. Chem. Soc.*, 2000, **122**, 3422-3435.

4. J. Gatineau, K. Yanagita and C. Dussarrat, *Microelectron. Eng.*, 2006, **83**, 2248-2252.

5. J. Gatineau and C. Dussarrat, *ECS Transactions*, 2007, **6**, 303-307.

6. Y. H. Song, Y. L. Chen, Y. Chi, C. S. Liu, W. L. Ching, J. J. Kai, R. S. Chen, Y. S. Huang and A. J. Carty, *Chemical Vapor Deposition*, 2003, **9**, 162-169.

7. J. Shin, A. Waheed, K. Agapiou, W. A. Winkenwerder, H.-W. Kim, R. A. Jones, G. S. Hwang and J. G. Ekerdt, *J. Am. Chem. Soc*., 2006, **128**, 16510-16511.

8. S. Caddick, *Tetrahedron*, 1995, **51**, 10403-10432.

9. T. Matsumura-Inoue, M. Tanabe, T. Minami and T. Ohashi, *Chem. Lett*., 1994, **23**, 2443-2446.

10. P. Lidstroum, J. Tierney, B. Wathey and J. Westman, *Tetrahedron*, 2001, **57**, 9225-9283.

11. R. S. Varma, *Green Chemistry*, 1999, **1**, 43-55.

12. T. Brietzke, W. Mickler, A. Kelling, U. Schilde, H.-J. Krüger and H.-J. Holdt, *European Journal of Inorganic Chemistry*, 2012, **2012**, 4632-4643.

13. K. Servaty, C. Moucheron and A. Kirsch-De Mesmaeker, *Dalton Transactions*, 2011, **40**, 11704-11711.

14. T. David Pilz, N. Rockstroh and S. Rau, *J. Coord. Chem*., 2010, **63**, 2727-2742.

15. S. Herrero, R. Jimenez-Aparicio, J. Perles, J. L. Priego and F. A. Urbanos, *Green Chemistry*, 2010, **12**, 965-967.

16. R. A. Jones, G. Wilkinson, A. M. R. Galas, M. B. Hursthouse and K. M. A. Malik, *J. Chem. Soc., Dalton Trans*., 1980, 1771-1778.

17. M. I. Bruce, M. G. Humphrey, M. R. Snow, E. R. T. Tiekink and R. C. Wallis, *J. Organomet. Chem*., 1986, **314**, 311-322.

18. R. A. Jones, F. M. Real, G. Wilkinson, A. M. R. Galas, M. B. Hursthouse, K. M. A. Malik, *J. Chem. Soc., Dalton Trans*., 1980, 511-518.

19. D. Villemin, M. Hammadi, M. Hachemi and N. Bar, *Molecules*, 2001, **6**, 831-844.

20. O. Renn and L. M. Venanzi, *Helv. Chim. Acta*, 1995, **78**, 993-999.

Chapter 3: A novel Ruthenium pyrazolate arene complex

3.1: INTRODUCTION

3.1.1: Overview

The objectives of the work described in this chapter were to design and synthesize new volatile ruthenium complexes and assess their viability to serve as CVD precursors. The deposition of ruthenium and ruthenium alloys are currently of considerable interest due to their high conductivity and chemical inactivity with copper and silicon[1] and it is known that films of Ru adhere well to silicon and can be directly electroplated with copper.[2, 3] Films of ruthenium tend to grow in crystalline columns oriented perpendicular to the film allowing copper diffusion over time[4] (Figure III-1).

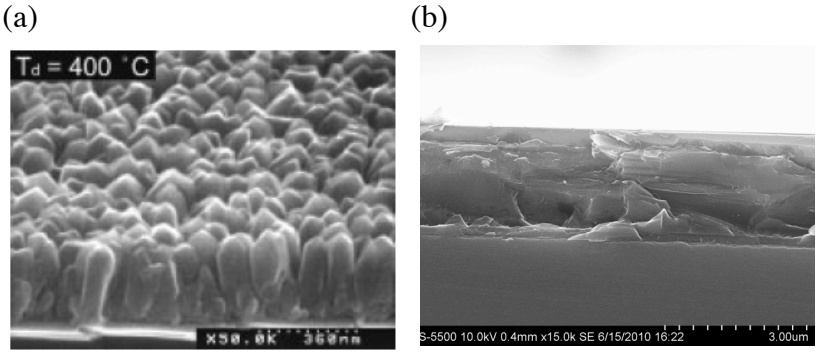

Figure III-1: Cross-sectional view SEM micrographs of Ru films that are (a) crystalline with column formations[5] and (b) amorphous.

As discussed in chapter 1, the use of amorphous thin films as barrier layers would eliminate this diffusion of the copper electrode as well as reduce problems associated with grain boundaries or stacking fault formation. Control over the morphology of deposited films whether amorphous or microcrystalline may reduce the migration of copper. In some cases it has been demonstrated that the morphology of films can be affected by the molecular structure of the precursor used as well as the deposition parameters (i.e., carrier gas, deposition temperatures, flow rate). Ligands designed to

improve the stability and volatility of metal complexes used as CVD precursors have been developed.[6-12]

In this respect, of particular interest in the Jones laboratory has been the use of the bis(trifluoromethyl)pyrazolate (3,5-$(CF_3)_2$-Pz) ligand (Figure III-2). It has been demonstrated by our group and by others that this ligand can give metal complexes which will enable the CVD growth of thin films of appropriate materials under relatively mild conditions.[7,9,11,13] Chapter 2 describes the synthesis and study of number of volatile carbonyl (CO) derivatives of Ru which feature the 3,5-$(CF_3)_2$-Pz ligand. An alternative approach to the design of volatile Ru complexes for CVD study is to investigate the use of ligands other than carbon monoxide. This chapter describes the synthesis, structure, and reactivity of the new compound $[(\eta^6\text{-}C_6H_6)(\mu\text{-}(3,5\text{-}(CF_3)\text{-Pz})Ru]_2$ (**3-II**) which bears an arene (η^6-C_6H_6) instead of three CO groups. It may be prepared by the reaction of the Ru(0) arene complex (η^6-C_6H_6)(η^4-C_6H_8)Ru (**3-I**) with the neutral pyrazole 3,5-$(CF_3)_2$-PzH.

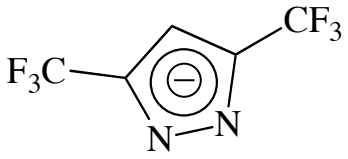

3,5-$(CF_3)_2$-Pz

Figure III-2: The bis(trifluoromethyl)pyrazolate ligand.

3.2: Results and Discussion

3.2.1 Synthesis of (η^6-C_6H_6)(η^4-C_6H_8)Ru as a Ru(0) source for CVD precursors

(η^6-C_6H_6)(η^4-C_6H_8)Ru (3-I). The Ru(0) starting material (η^6-C_6H_6)(η^4-C_6H_8)Ru (**3-I**) was prepared by a modification of the known procedure.[14] The treatment of an

ethanolic solution of $RuCl_3 \cdot 3H_2O$ and 1,3-cyclohexadiene with zinc dust after workup produces **3-I** in 70 % yield as a yellow crystalline solid (Scheme III-1). Under similar conditions, but using 1,4-cyclohexadiene instead of the 1,3 isomer, also produces **3-I** but in lower yields.[14] Compound **3-I** is thermally unstable at room temperature and should be stored at -78 ^{0}C and used within a few days of preparation.

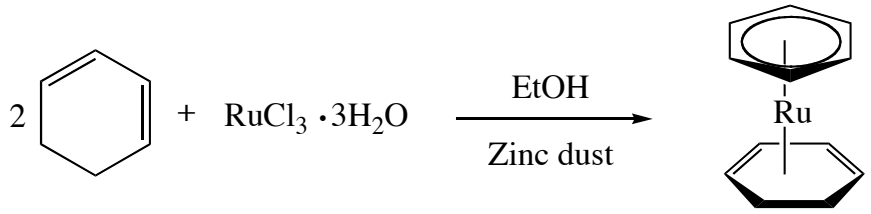

3-I

Scheme III-1: Synthesis of (η^6-C_6H_6)(η^4-C_6H_8)Ru (**3-I**).

Although the structure of **3-I** in solution was originally established by NMR studies[14] the structure in the solid state as determined by a single crystal X-ray diffraction study has never been reported. In order to completely characterize the compound this study was undertaken and the structure described below. Dr. Joseph Rivers performed the X-ray diffraction studies for **3-I**.

Complex **3-I** crystallizes in the monoclinic space group $P2_12_12_1$ with four molecules per unit cell. Figure III-3 shows the molecular geometry and atom numbering scheme. Crystallographic details are given in Table III-3 and key bond lengths and angles are given in Table III-4. The overall molecular structure of **3-I** does not have completely planar rings in its sandwich structure as in bis(η^5-cyclopentadienyl)ruthenium (ruthenocene), due to the presence of the η^4-cyclohexa-1,4-diene group. The carbon-ruthenium distance for the aromatic ring is 2.217(3) A which is similar to that found for the carbon-ruthenium distance in ruthenocene.[15] The carbon-ruthenium distances for the unbound methylenes are 3.050(7) Å and 3.064(7) Å.

The ^{1}H NMR of **3-I** has a singlet at 5.29 ppm for the η^6-C_6H_6, a doublet of doublets at 4.65 ppm for the hydrogens on C(12) and C(7), a multiplet at 2.05 ppm for the hydrogens on C(11) and C(8) and a multiplet at 1.35 ppm for the hydrogens on C(10) and C(9).

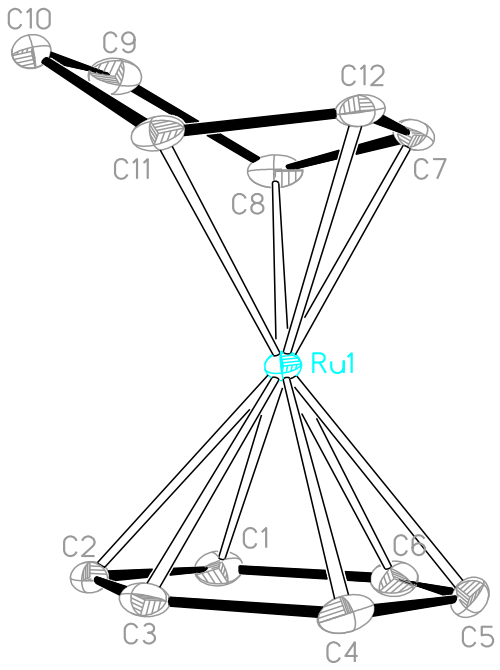

Figure III-3: ORTEP view of **3-I** with partial atom numbering scheme. Ellipsoids are drawn at 30% probability level. Hydrogen atoms are omitted for clarity.

3.2.2: Synthesis of the Ruthenium Pyrazolate [(η^6-C_6H_6)(μ-(3,5-(CF_3)-Pz)Ru]$_2$

[(η^6-C_6H_6)(μ-(3,5-(CF_3)-Pz)Ru]$_2$ (3-II). Reaction of (η^6-C_6H_6)(η^4-C_6H_8)Ru **(3-I)** with bis(trifluoromethyl)pyrazole (3,5-(CF_3)$_2$-PzH) in refluxing toluene for 18 hours produced a bright red colored solution. Evaporation of the solvent to dryness and recrystallization of the residue from hexane produced the red crystalline dimer [(η^6-C_6H_6)(μ-(3,5-(CF_3)-Pz)Ru]$_2$ **(3-II)** in 87 % yield. The compound is relatively air stable and thermally stable under nitrogen up to its melting point (240-1 ^{0}C). It may be sublimed under reduced pressure (0.1 torr) at 180 ^{0}C.

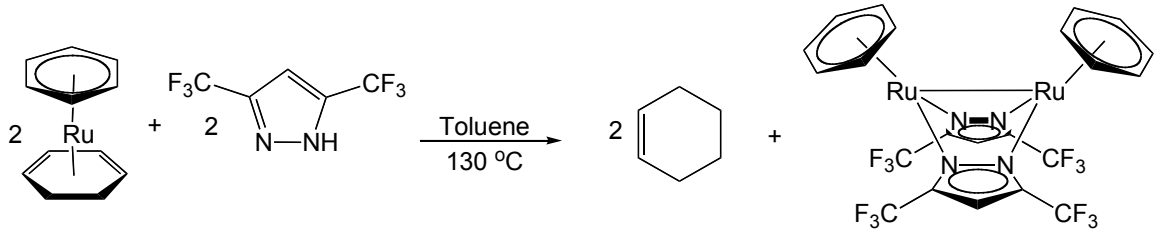

3-II

Scheme III-2: Synthesis of (**3-II**).

Complex **3-II** crystallizes in the monoclinic space group $C2/_c$ with 6 molecules per unit cell. Figure III-4 shows the molecular geometry and atom numbering scheme. Crystallographic details are giving in Table III-3 and key bond lengths and angles are given in Table III-5. The two benzene rings act as 6-electron donors (η^6-C_6H_6) and the two Ru(I) centers are separated by 2.750 Å. If this interaction is viewed as a single Ru-Ru bond then each of the Ru atoms has an electron count of 18. The compound is therefore isoelectronic with $[Ru(CO)_3\mu\text{-}(3,5\text{-}(CF_3)\text{-}Pz)]_2$ (**2-I**). The two μ-(3,5-(CF_3)-Pz groups bridge on the same side of the molecule with a dihedral angle of 82.73^0 between the two Ru_2N_2 planes.

The ^{1}H NMR spectrum in C_6D_6 has a singlet at 6.44 ppm assigned to the protons of the η^6-C_6H_6 plus a singlet at 5.44 ppm assigned to the unique proton on the backbone of the 3,5-$(CF_3)_2$-Pz groups. Integration of the peaks give a 6:1 ratio which is consistent with the structure $[Ru(CO)_3(\mu\text{-}Pz\text{-}CF_3)]_2$ (**2-I**).

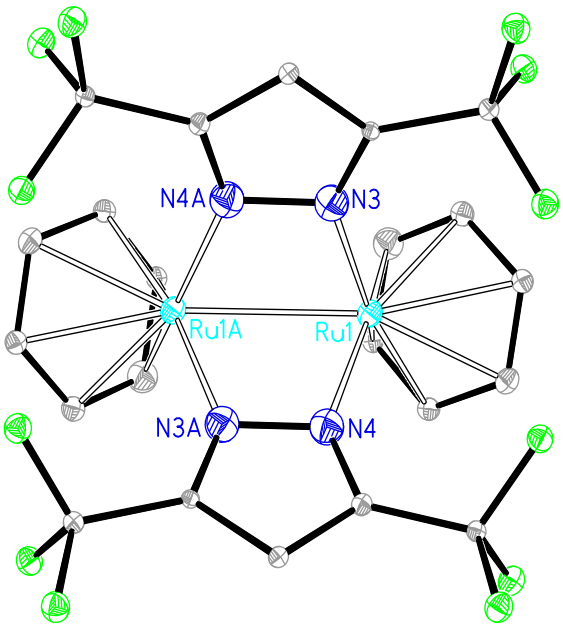

Figure III-4: ORTEP view of **3-II** with partial atom numbering scheme. Ellipsoids are drawn at 30% probability level. Hydrogen atoms are omitted for clarity.

3.2.3: Reactivity Studies of $[(\eta^6\text{-}C_6H_6)(\mu\text{-}(3,5\text{-}(CF_3)\text{-}Pz)Ru]_2$ 3-II.

The chemical reactivity of $[(\eta^6\text{-}C_6H_6)(\mu\text{-}(3,5\text{-}(CF_3)\text{-}Pz)Ru]_2$ **3-II** in terms of substitution, oxidation, reduction, and protonation reactions was explored. The isolation and characterization of the dinuclear pyrazolate complex $[(\eta^6\text{-}C_6H_6)(\mu\text{-}(3,5\text{-}(CF_3)\text{-}Pz)Ru]_2$ **3-II** leads to the possibility that other volatile CVD precursors could be prepared based on the central $Ru_2(Pz)_2$ framework by substitution of the $\eta^6\text{-}C_6H_6$ ligands. Although the metals are saturated, one side of side of the Ru-Pz plane is sterically open to access by reagents. However, at room temperature **3-II** appears to be quite unreactive with respect to simple reactions and under more extreme conditions of temperature and pressure decomposition occurred. Thus, **3-II** was recovered unchanged from reactions with neat hexafluorobenzene, tris(trifluoromethyl)benzene, thiophene, and PMe_3 at room temperature for several days. In the case of PMe_3, reactions at 110 ^{0}C in a closed system or microwave reactions with solutions of PMe_3 in THF, again resulted in no reaction occurring. A survey of the reactions and conditions is given in Scheme III-3. In

addition to these substitution reactions, treatment of **3-II** with molecular oxygen (O_2) and strong acid (HBF_4 in diethyl ether) at room temperature again resulted in no reaction and **3-II** was recovered unchanged from the reaction solutions. Unfortunately, under more forcing conditions the reactions described above all led to the decomposition, as did reactions with H_2 at higher temperatures. These reactions gave intractable mixtures from which no pure compounds could be isolated or identified (by ^1H NMR). A summary of these decomposition reactions is given in Scheme III-4.

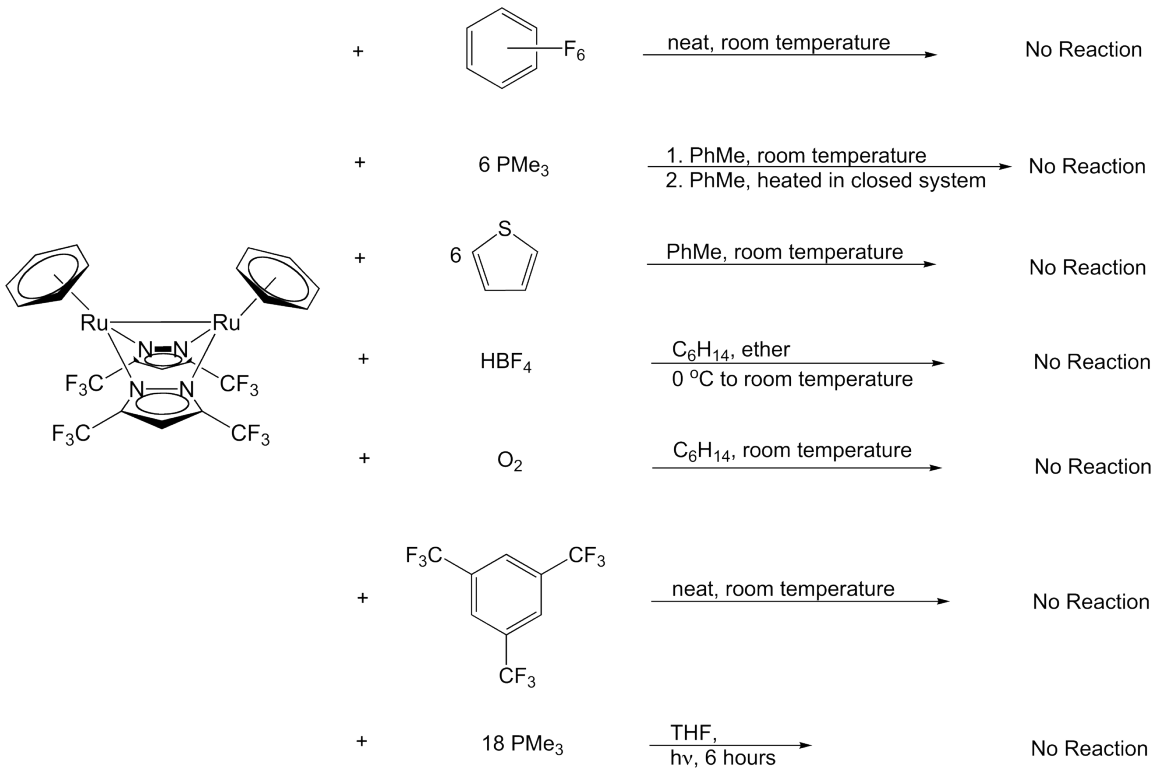

Scheme III-3: Reactivity studies: **3-II**.

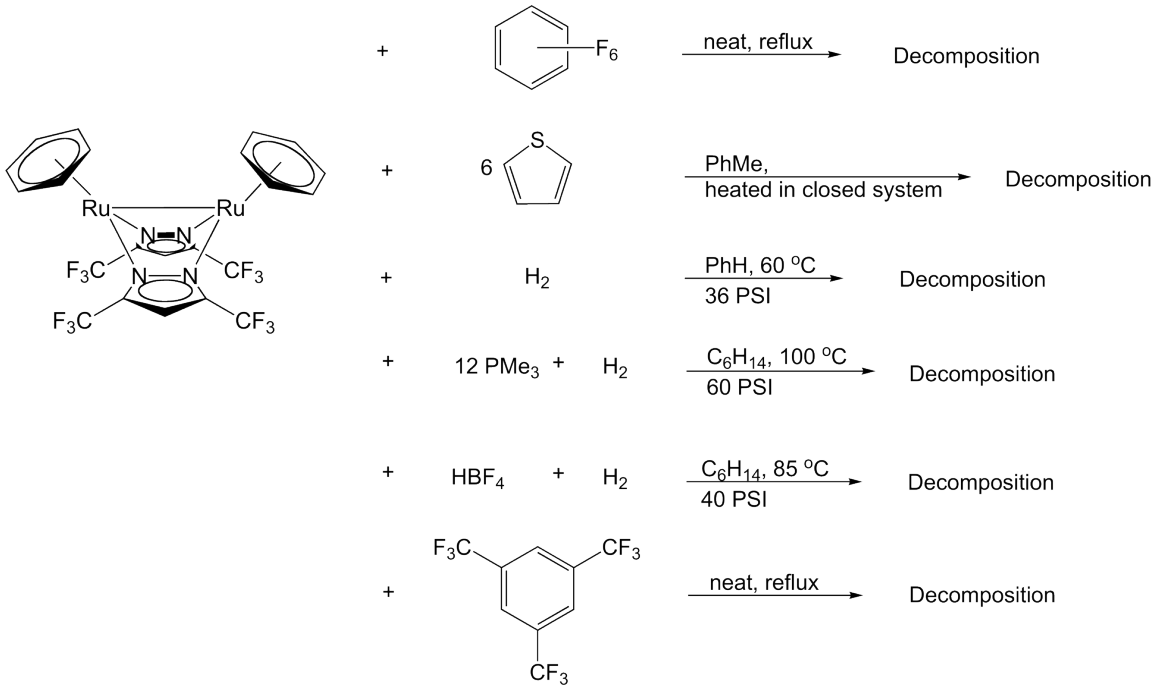

Scheme III-4: Decomposition reactions of **3-II**.

The stability or the lack of reactivity of **3-II** to oxidation, reduction, substitution reactions, as well as harsh conditions can be compared to the stability of $[(Cym)RuCl_2]_2$ (Cym = cymene) (**3-III**) another compound that is isoelectronic with **3-II** (Figure III-5). $[(Cym)RuCl_2]_2$ also contains two Ru(I) species with a metal-metal bond and cymene which can serve as a leaving group for this compound. Walstrom reported that **3-III** should have some reactivity associated either with its redox character, or even through heterolytic spitting of the Ru-Ru bond yielding a mononuclear species. This proved difficult, as **3-III** was reported to be quite unreactive to addition of 1 atm of N_2, H_2, N_2O, and equimolar $SiHMe_3$, even after heating for 24 hours at reflux.[16]

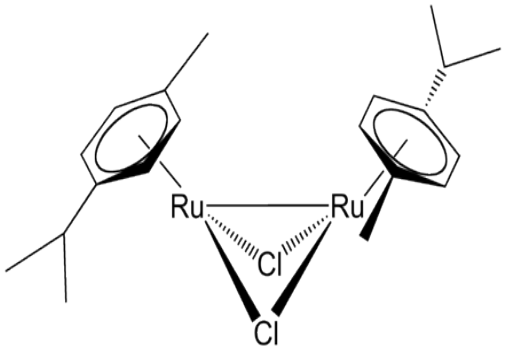

3-III

Figure III-5: $[(Cym)RuCl_2]_2$ (**3-III)** having similar reactivity as **3-II**.

3.2.4: Film Growth Studies

Complex $[(\eta^6\text{-}C_6H_6)(\mu\text{-}(3,5\text{-}(CF_3)\text{-}Pz)Ru]_2$ **(3-II)** was found to be a suitable CVD precursor and preliminary film growth studies were conducted. Thin films were deposited on native 400 nm SiO_2/Si(100) substrates under various conditions. A summary of typical deposition conditions is given in Table III-1 and film characterization data in Table III-2.

Table III-1: Typical deposition conditions of CVD films grown from **3-II**.

Precursor	Reaction Type	Carrier Gas/Flow rate (sccm)	Precursor Temp (°C)	Substrate Temp (°C)	Depostion Time (min.)
$[(\eta^6\text{-}C_6H_6)(\mu\text{-}(3,5\text{-}(CF_3)\text{-}Pz)Ru]_2$ **(3-II)**	Hot-wall	Ar, 11	180	400	45

Table III-2: Summary of material characterization data for films grown from **3-II**.

Precursor	Thickness (nm)	Microstructure	Composition after sputtering (%) Ru	O
$[(\eta^6\text{-}C_6H_6)(\mu\text{-}(3,5\text{-}(CF_3)\text{-}Pz)Ru]_2$ **(3-II)**	0.6 micro m	amorphous	90.05	9.95

Under the growth conditions employed thin films grown using **3-II** were of uniform thickness (0.4 micrometers) and SEM studies showed they were continuous with a glossy metallic appearance. Compositional analysis by XPS revealed a film composed

mostly of Ru with a high level of O distributed throughout. Sputtering with Ar^+ reduced the levels of the surface O but this leveled off and remained constant at less then 10 % (Figure III-6). No traces of N or F were detected after sputtering to remove surface contaminants. After surface contaminants are removed (accounting for 28 % of the surface of the film) the amount of Ru increased and the amount of O decreased until they remained constant. Carbon was not calculated because the C 1s orbital overlaps in the same region with the Ru 3d orbital. Side angle SEM images show a uniform film of 0.6 mm thickness with some evidence of grain boundaries (Figure III-7).

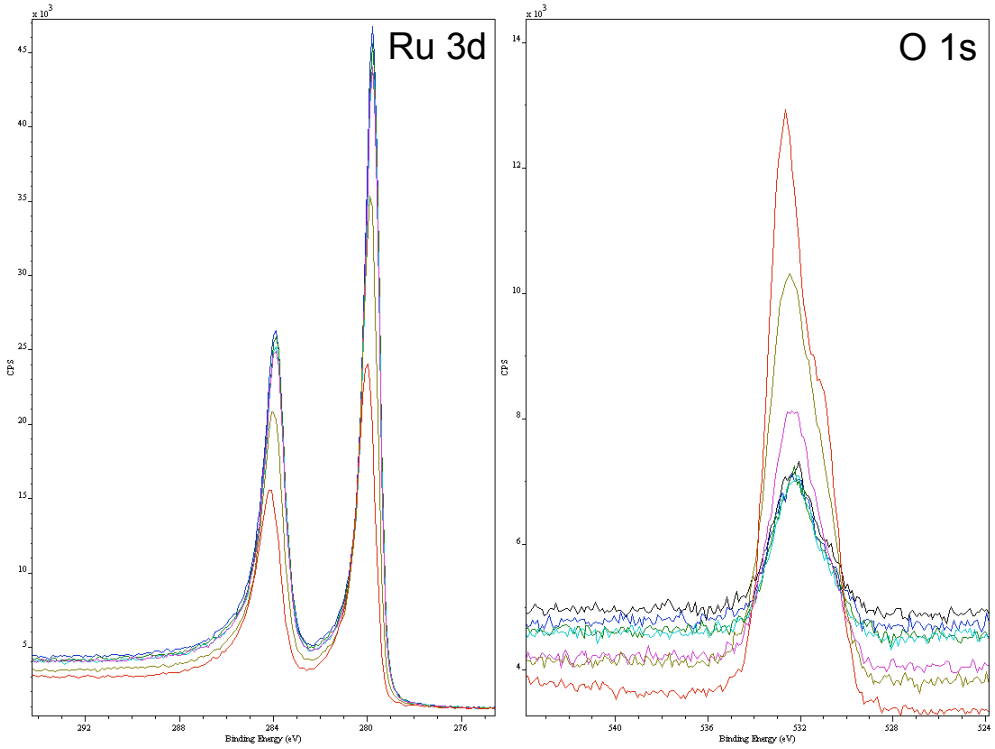

Figure III-6: XPS sputtering analysis of **3-II** (a) Ru 3d (b) O 1s.

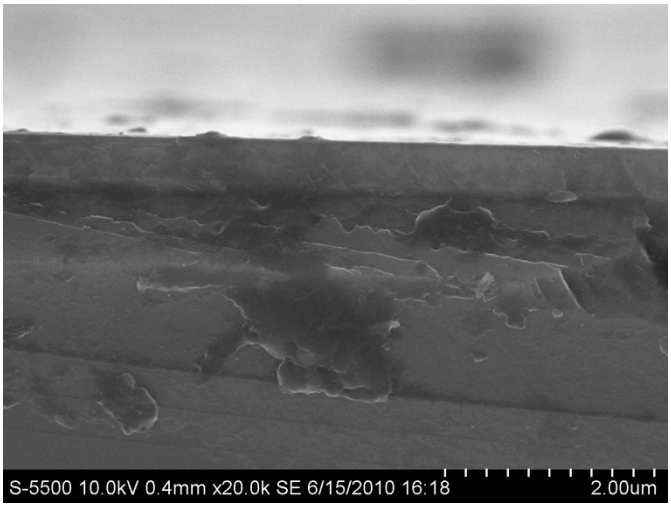

Figure III-7: SEM side view of film grown from **3-II.**

All deposited films appeared lustrous with a silvery-pink hue and adhered well to the silicon substrate as determined by a cellophane test. All as-deposited films were amorphous in nature, as indicated by the lack of diffraction peaks in the X-ray diffraction patterns taken after film growth (Figure III-8). Upon annealing at 500 ^{0}C under dynamic vacuum the films became crystalline in nature and diffraction peaks were observed as shown in Figure III-8. The peaks at 29, 31, and 32 represent crystalline hcp Ru, (hexagonal close packed) with lattice parameters a = 2.7508, b = 2.7508, c = 4.2819 Å (PDF# 01-088-1734).

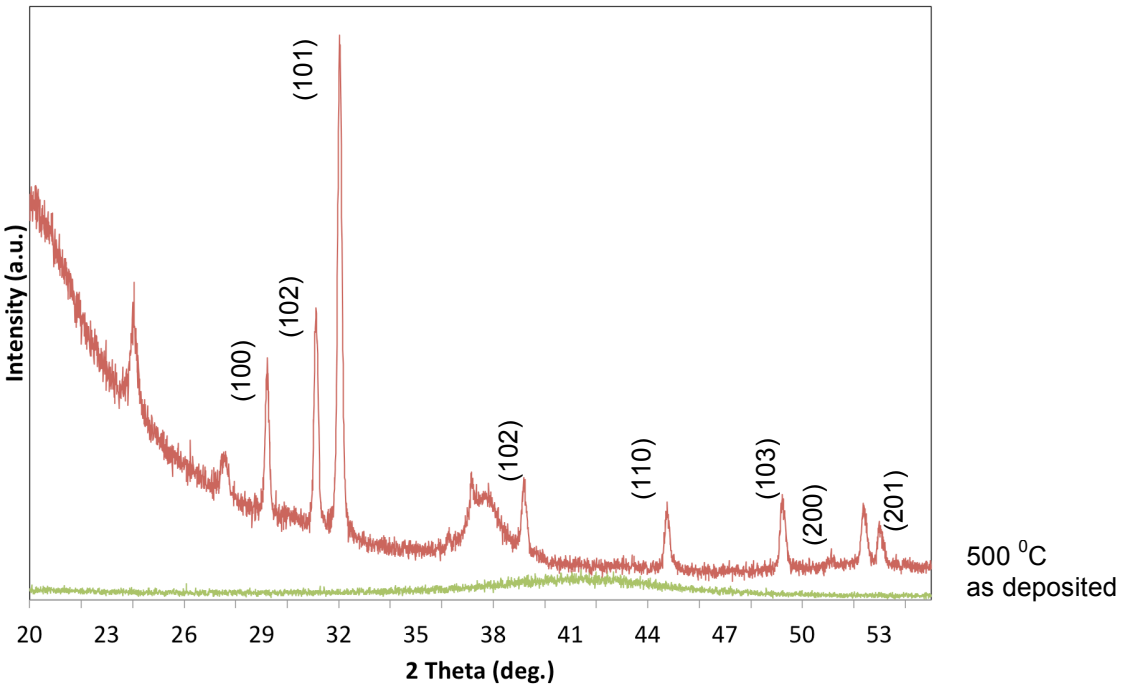

Figure III-8: XRD patterns of a Ru film deposited from **3-II** under Ar and then annealed at 500 ^{0}C under dynamic vacuum. The patterns are vertically shifted for comparison.

3.2.5: Future Studies

The synthesis and design of new CVD precursors is an expanding field and being able to analyze the differences in composition and morphology of the films by fine tuning the ligand environment is crucial to understanding how the molecular structure effects the film production. Compound **3-II** provided underwhelming results by being unreactive with other reagents or decomposing to indistinguishable products. Other pyrazolate derivatives (3,5-(^{t}Bu)$_2$-Pz and 3,5-(CH$_3$)$_2$-Pz) that were reacted with **3-I** produced mixtures of inseparable species of which no single product could be detected (by ^{1}H NMR) or isolated by crystallization. It is possible that the two CF$_3$ groups on the pyrazole are crucial for the formation of **3-II**. Future considering should be given to the reaction of **3-I** with 3-(CF$_3$),5-(^{t}Bu)-Pz and 3-(CF$_3$),5-(CH$_3$)-Pz to isolate new Ru compounds and screen them for CVD potential.

Ideally, a set of Ru(I)-Ru(I) complexes with diverse pyrazolate ligands would provide a better data set for the comparison of film growth and morphologies of Ru thin films. Finally, it was believed that the η^6-C_6H_6 ligand could be removed and substituted with other neutral ligands to produce another series of Ru(I)-Ru(I) complexes with bridging pyrazolates but that, too, became difficult.

Considering that there are other reactive arene-based sandwich compounds known it would be fruitful to synthesize other $[(\eta^6\text{–}C_6H_6)(\mu\text{-}(3,5\text{-}(CF_3)\text{-Pz})M]_2$ complexes based on the known reaction of **3-I** with 3,5-$(CF_3)_2$-PzH to screen for CVD precursors (M = Os,[17] Re,[18] Mn,[19] Mo[20]).

3.3: EXPERIMENTAL

3.3.1: General Synthesis

All reactions were performed under a dry, oxygen-free nitrogen atmosphere or under vacuum using standard Schlenk line and dry box techniques. Solvents were dried prior to use by distillation from sodium benzophenone ketyl anion under nitrogen. The compound bis(trifluoromethyl)pyrazole (3,5-$(CF_3)_2$-PzH) was prepared as previously described.[21] Trimethylphosphine (97%), hexafluorobenzene, trimethylphosphine, thiophene, fluoroboric acid, dioxygen, and 1,3,5-tris(trifluoromethyl)benzene were purchased from Fisher and Aldrich and used without further purification.

3.3.2: Film Deposition Conditions

Films were grown in a homemade hot-wall CVD reactor consisting of a quartz deposition region heated by a tube furnace. Films were deposited on native 400 nm SiO_2/Si(100) wafers. All fittings were VCR metal gasket face sealing connections with stainless steel lines. The precursor was heated in a Pyrex ampoule connected to the system and carried using ultra-high purity argon (99.999%, Airgas) at flow rates of 10-12 sccm with a mass flow controller (Fathom Technologies, 0-50 sccm range). The lines were kept warm with insulated heating tape and wrapped with glass wool and heavy

grade aluminum foil. The wafers were cut in 4 mm x 8 mm pieces and positioned on quartz boats inside the deposition region.

3.3.3: Instrumental Details

NMR spectra were recorded on a Varian 300 Unity spectrometer (^{1}H, 300 MHz) at 25 ^{0}C. ^{1}H NMR signals are reported relative to residual proton resonances in deuterated solvents. Infrared spectra were recorded using a Nicolet IR 200 FTIR spectrometer using attenuated total reflectance (ATR). High-resolution mass spectra (HRMS) were obtained on a VG Analytical ZAB-VE sector instrument and are reported as *m/z* (relative intensity). Melting points were obtained using an Electrothermal resistively heated melting point apparatus in sealed glass capillaries under a dinitrogen atmosphere or 0.1 torr vacuum. The microwave reactions were performed in a CEM discover reactor.

Film compositions were measured using *ex situ* high-resolution XPS analysis (Kratos AXIS Ultra DLD; monochromatic Al K_α). Depth profiling was achieved by sputtering the film with 4 kV Ar^+. The structural nature of the films were established by grazing angle (2^0-4^0) X-ray diffraction (XRD) (Bruker-Nonius D8). Film thicknesses were determined using cross-sectional SEM (Hitachi S-5500).

X-Ray diffraction studies were performed by Dr. Joseph Rivers and Dr. W. Jeffrey McCarty. All crystals were mounted on a glass fiber. The data was collected on either a Nonius Kappa CCD diffractometer using a graphite monochromator with MoK_α radiation (λ = 0.71073 Å) at reduced temperature using an Oxford Cryostream low temperature device or a Rigaku AFC12 diffractometer with a Saturn 724+ CCD using a graphite monochromator with MoK_α radiation at reduced temperature using a Rigaku XStream low temperature device. Data reduction was performed with either DENZO-SMN or Rigaku Americas Corporation's Crystal Clear version 1.40. The structures were solved by direct methods using SIR97 and refined by full-matrix least-squares on F^2 with

anisotropic displacement parameters for the non-H atoms using SHELXL-97. The absolute configuration was assigned by internal comparison to the known absolute configuration of selected portions of the molecule. The hydrogen atoms on carbon were calculated in idealized positions with isotropic displacement parameters set to 1.2XUeq of the attached atom. All figures were generated using SHELXTL/PC.

3.3.4: Synthesis of Complexes

(η^6-C_6H_6)(η^4-C_6H_8)Ru (3-I)

RuCl•3H2O (0.320 g, 1.23 mmol) was completely dissolved in absolute ethanol (8 mL). 1,3-cyclohexadiene (5 mL, 52 mmol) (previously distilled and stored under nitrogen) and zinc dust (3 g, 45 mmol) were added in that order and mixture stirred for 3 h at room temp. The resulting yellow-brown solution was canula-filtered to a new Schlenk flask and the residual solid was washed three times with anhydrous pentane. The solutions were combined and the solvent removed under vacuum. The solid residue was dissolved in anhydrous pentane (20 mL). The concentrated solution was cooled (-30 ^{0}C) to produce 0.225 g (70%) of yellow crystals. m.p. 118-120 ^{o}C (1 atm N_2). ^{1}H NMR (300 MHz, acetone-d_6, 27 ^{o}C) δ 5.29 (s, 6H, Ar-*H*), 4.65 (dd, 2H), 2.05 (m, 2H), 1.35 (m, 4H). EI/MS *m/e*: 289 [M^+].

[(η^6−C_6H_6)(μ-(3,5-(CF_3)-Pz)Ru]$_2$ (3-II)

Over molecular sieves **3-I** (0.211 g, 0.82 mmol) was dried in toluene (10 mL) in a Schlenk flask. In a secondary Schlenk flask 3,5-(CF_3)$_2$-PzH (0.500 g, 2.45 mmol) was dried over molecular sieves in toluene (15 mL). The solution of **3-I** was cannulated into the solution of 3,5-(CF_3)$_2$-PzH and the reaction mixture was refluxed (130 ^{0}C) for 18 h to give a vibrant red solution. Toluene was removed under vacuum and the residue dissolved in hexane and concentrated (5 mL). The concentrated solution was cooled to -40 ^{0}C to produce 0.44 g (70%) of red crystals. m.p. *dec*. 240 ^{o}C (1 atm N_2). 180 ^{o}C sublime (0.1 torr). ^{1}H NMR (300 MHz, $CDCl_3$, 27 ^{o}C) δ 6.44 (s, 12H, Ar-*H*), 5.44 (s,

2H,). EI/MS *m/e*: 765 [M^+], 562 [-Pz]. FTIR (ATR, cm^{-1}): 2372 (m), 2152 (m), 1941 (w), 1643 (w), 1409 (w), 1155 (m).

3.3.5: Reactivity studies of [(η^6–C_6H_6)(μ-(3,5-(CF_3)-Pz)Ru]$_2$ (3-II).

Reactivity Studies of [(η^6–C_6H_6)(μ-(3,5-(CF_3)-Pz)Ru]$_2$ (3-II):

[(η^6–C_6H_6)(μ-(3,5-(CF_3)-Pz)Ru]$_2$ (3-11) and C_6F_6. Compound **3-II** (0.100 g, 0.131 mmol) was dissolved in toluene (10 mL). Perfluorobenzene was added (0.045 mL, 0.393 mmol) via syringe. The reaction mixture was stirred for 18 h and mixture was cannula filtered to a new flask and solvent was removed under vacuum. The residual solid was dissolved in a minimal amount of hexane, concentrated (5 mL) and cooled to -30 ^{0}C to give red crystals of **3-II** (by ^{1}H NMR).

[(η^6–C_6H_6)(μ-(3,5-(CF_3)-Pz)Ru]$_2$ (3-11) and PMe_3. Compound **3-II** (0.100 g, 0.131 mmol) was dissolved in toluene (10 mL). PMe_3 was added (0.080 mL, 0.786 mmol) via syringe. The reaction mixture was stirred for 48 h and the mixture was cannula filtered to a new flask and solvent was removed under vacuum. The residual solid was dissolved in a minimal amount of hexane, concentrated (5 mL) and cooled to -30 ^{0}C to give red crystals of **3-II** (by ^{1}H NMR).

[(η^6–C_6H_6)(μ-(3,5-(CF_3)-Pz)Ru]$_2$ (3-11) and thiophene. Compound **3-II** (0.100 g, 0.131 mmol) was dissolved in toluene (10 mL). Thiophene which was previously dried and distilled was added (0.063 mL, 0.785 mmol) via syringe. The reaction mixture was stirred for 36 h and the mixture was cannula filtered to a new flask and solvent was removed under vacuum. The residual solid was dissolved in a minimal amount of hexane, concentrated (5 mL) and cooled to -30 ^{0}C to give red crystals of **3-II** (by ^{1}H NMR).

[(η^6–C_6H_6)(μ-(3,5-(CF_3)-Pz)Ru]$_2$ (3-11) and HBF_4. Compound **3-II** (0.050 g, 0.065 mmol) was dissolved in hexane (15 mL). The reaction mixture was cooled to 0 ^{0}C

and HBF_4 was added (0.218 mL, 0.065 mmol of a 37 % wt in diethyl ether) via syringe. The reaction mixture was slowly warmed to room temperature and was stirred for 18 h. The reaction mixture was cannula filtered to a new flask and solvent was removed under vacuum. The residual solid was dissolved in a minimal amount of hexane, concentrated (5 mL) and cooled to -30 ^{0}C to give red crystals of **3-II** (by ^{1}H NMR).

[(η^6–C_6H_6)(μ-(3,5-(CF_3)-Pz)Ru]$_2$ (3-11) and O_2. Compound **3-II** (0.050 g, 0.065 mmol) was dissolved in hexane (50 mL). Dry O_2 was slowly bubbled into the solution for 10 minutes. The reaction mixture was stirred for 12 h and mixture was cannula filtered to a new flask and solvent was removed under vacuum. The residual solid was dissolved in a minimal amount of hexane, concentrated (5 mL) and cooled to -30 ^{0}C to give red crystals of **3-II** (by ^{1}H NMR).

[(η^6-C_6H_6)(μ-(3,5-(CF_3)-Pz)Ru]$_2$ (3-11) and 1,3,5-tris(trifluoromethyl)benzene. Compound **3-II** (0.050 g, 0.065 mmol) was dissolved in 1,3,5-tris(trifluoromethyl)benzene (10 mL, 0.054 mmol). The reaction mixture was stirred for 18 h and mixture was cannula filtered to a new flask and solvent was removed under vacuum. The residual solid was dissolved in a minimal amount of hexane, concentrated (5 mL) and cooled to -30 ^{0}C to give red crystals of **3-II** (by ^{1}H NMR).

[(η^6–C_6H_6)(μ-(3,5-(CF_3)-Pz)Ru]$_2$ (3-11) and PMe_3 using hν. Compound **3-II** (0.100 g, 0.131 mmol) was dissolved in THF (15 mL) in a quartz Schlenk tube. PMe_3 was added (0.236 mL, 2.32 mmol) via syringe. While stirring the reaction mixture was trated with ultra-violet light (hν) via a mercury lamp for 6 h. The reaction mixture was cannula filtered to a new flask and solvent was removed under vacuum. The residual solid was dissolved in a minimal amount of hexane, concentrated (5 mL) and cooled to -30 ^{0}C to give red crystals of **3-II** (by ^{1}H NMR).

[(η^6–C_6H_6)(μ-(3,5-(CF_3)-Pz)Ru]$_2$ (3-11) and thiophene. Compound **3-II** (0.100 g, 0.131 mmol) was dissolved in toluene (10 mL). Thiophene which was previously dried and distilled was added (0.063 mL, 0.785 mmol) via syringe. The reaction mixture

was stirred for 36 h and mixture was cannula filtered to a new flask and solvent was removed under vacuum. The residual solid was dissolved in a minimal amount of hexane, concentrated (5 mL) and cooled to -30 ^{0}C to give red crystals of **3-II** (by ^{1}H NMR).

Using more forcing conditions with [(η^6–C_6H_6)(μ-(3,5-(CF_3)Ppz)Ru]$_2$ (3-II).

[(η^6–C_6H_6)(μ-(3,5-(CF_3)-Pz)Ru]$_2$ (3-11) and C_6F_6. Compound **3-II** (0.100 g, 0.131 mmol) was dissolved in toluene (10 mL). Perfluorobenzene was added (0.045 mL, 0.393 mmol) via syringe. The reaction mixture was refluxed (130 ^{0}C) for 36 h and the purple solution was cannula filtered to a new flask and solvent was removed under vacuum. The residual solid was washed with hexane, concentrated (5 mL) and cooled to -30 ^{0}C, no crystals formed and the ^{1}H NMR of the solid residue showed nothing distinguishable.

[(η^6–C_6H_6)(μ-(3,5-(CF_3)-Pz)Ru]$_2$ (3-11) and thiophene. Compound **3-II** (0.100 g, 0.131 mmol) was dissolved in toluene (10 mL). Thiophene which was previously dried and distilled was added (0.063 mL, 0.785 mmol) via syringe. The reaction mixture was refluxed (130 ^{0}C) for 24 h and mixture was cannula filtered to a new flask and solvent was removed under vacuum. The residual solid was washed with hexane, concentrated (5 mL) and cooled to -30 ^{0}C, no crystals formed and the ^{1}H NMR of the solid residue showed nothing distinguishable.

[(η^6–C_6H_6)(μ-(3,5-(CF_3)-Pz)Ru]$_2$ (3-11) and H_2. Compound **3-II** (0.090 g, 0.118 mmol) was dissolved in hexane (10 mL). PMe_3 was added (0.144 mL, 1.41 mmol) via syringe. The reaction mixture was transferred to a Fisher-Porter bottle via cannula and was cooled to -78 ^{0}C and was introduced to an excess of hydrogen with the resultant pressure of 60 PSI. The flask was sealed, allowed to warm to room temperature, and heated to 100 ^{0}C for 12 hours. The excess hydrogen was removed under vacuum and the

solution was transferred to a Schlenk flask, solvent was removed in vacuo and the residual solid was washed with hexane, concentrated (5 mL) and cooled to -30 ^{0}C, no crystals formed and the ^{1}H NMR of the solid residue showed nothing distinguishable.

[(η^6–C_6H_6)(μ-(3,5-(CF_3)-Pz)Ru]$_2$ (3-11), H_2, and PMe_3. Compound **3-II** (0.090 g, 0.118 mmol) was dissolved in hexane (10 mL). PMe_3 was added (0.144 mL, 1.41 mmol) via syringe. The reaction mixture was transferred to a Fisher-Porter bottle via cannula and was cooled to -78 ^{0}C and was introduced to an excess of hydrogen with the resultant pressure of 60 PSI. The flask was sealed, allowed to warm to room temperature, and heated to 100 ^{0}C for 12 hours. The excess hydrogen was removed under vacuum and the solution was transferred to a Schlenk flask, solvent was removed in vacuo and the residual solid was washed with hexane, concentrated (5 mL) and cooled to -30 ^{0}C, no crystals formed and the ^{1}H NMR of the solid residue showed nothing distinguishable.

[(η^6–C_6H_6)(μ-(3,5-(CF_3)-Pz)Ru]$_2$ (3-11), H_2, and HBF_4. Compound **3-II** (0.050 g, 0.065 mmol) was dissolved in hexane (15 mL). The reaction mixture was cooled to 0 ^{0}C and HBF_4 was added (0.218 mL, 0.065 mmol of a 37 % wt in diethyl ether) via syringe. Reaction mixture slowly warmed to room temperature and was stirred for 6 h. The reaction mixture was transferred to a Fisher-Porter bottle via cannula and was cooled to -78 ^{0}C and was introduced to an excess of hydrogen with the resultant pressure of 40 PSI. The flask was sealed, allowed to warm to room temperature, and heated to 85 ^{0}C for 18 hours. The excess hydrogen was removed under vacuum and the solution was transferred to a Schlenk flask, solvent was removed in vacuo and the residual solid was washed with hexane, concentrated (5 mL) and cooled to -30 ^{0}C, no crystals formed and the ^{1}H NMR of the solid residue showed nothing distinguishable.

[(η^6-C_6H_6)(μ-(3,5-(CF_3)-Pz)Ru]$_2$ (3-11) and 1,3,5-tris(trifluoromethyl)benzene. Compound **3-II** (0.100 g, 0.131 mmol) was dissolved in 1,3,5-tris(trifluoromethyl)benzene (10 mL, 0.054 mmol). The reaction mixture was refluxed for 18 h (150 ^{0}C) and mixture was cannula filtered to a new flask and solvent was

removed under vacuum. The residual solid was washed with hexane, concentrated (5 mL) and cooled to -30 ^{0}C, no crystals formed and the ^{1}H NMR of the solid residue showed nothing distinguishable.

3.4: APPENDIX

Table III-3: Crystal data and structure refinement for **3-I** and **3-II**.

	3-I	**3-II**
Empirical formula	$C_{12}H_{14}Ru$	$C_{22}H_{14}F_{12}NRu_2$
Fw, g/mol	288.37	565.75
Temperature, K	293(2)	293(2)
Crystal system	Monoclinic	Monoclinic
Space group	$P2_12_12_1$	$C2/_c$
a, Å	5.979(2)	15.818(3)
b, Å	7.985(1)	7.9605(16)
c, Å	19.840(3)	18.545(4)
α, deg	90	90
β, deg	90	101.64(3)
γ, deg	90	90
V, Å^3	947.208(3)	2287.2(8)
Z	4	6
D_{calc}, g cm^{-3}	1.807	1.643
μ, mm^{-1}	1.015	0.741
F(000)	512	1143
θ range, deg	3.56- 27.44	3.09 - 24.99
Reflections collected	2093	3698
Unique reflections	2093	1994
Reflections used	2041	1815
Restraints	0	0
Parameters	174	181
Goodness-of-fit	0.735	1.899
R[a] indices [I>2σ(I)]	R_1 = 0.0232	R_1 = 0.0929
	wR_2 = 0.0582	wR_2 = 0.2482
R[a] (all data)	R_1 = 0.0224	R_1 = 0.0892
	wR_2 = 0.0570	wR_2 = 0.2456

[a] $R_1 = \Sigma_{hkl} (|F_o|-|F_c|)/\Sigma_{hkl}|F_o|$, $R_2 = [\Sigma\, w(|F_o|-|F_c|)^2/\Sigma\, w|F_o|^2]^{1/2}$

Table III-4: Selected Bond Lengths (Å) and Angles (°) for **3-I**.

Bond Lengths (Å)	
Ru(1)-C(7)	2.144(3)
Ru(1)-C(12)	2.142(3)
Ru(1)-C(8)	2.164(3)
Ru(1)-C(11)	2.166(3)
Ru(1)-C(1)	2.211(3)
Ru(1)-C(2)	2.217(3)
Ru(1)-C(3)	2.213(3)
Ru(1)-C(4)	2.246(3)
Ru(1)-C(5)	2.229(3)
Ru(1)-C(6)	2.229(3)
C(9)-C(10)	1.528(5)
Bond Angles (°)	
C(7)-Ru(1)-C(12)	38.55(12)
C(12)-Ru(1)-C(8)	67.09(12)
C(8)-Ru(1)-C(11)	72.97(11)
C(7)-Ru(1)-C(3)	163.16(13)
C(9)-C(8)-Ru(1)	111.8(2)
C(10)-C(11)-Ru(1)	110.8(2)

Table III-5: Selected Bond Lengths (Å) and Angles (°) for **3-II**.

Bond Lengths (Å)	
Ru(1A)-Ru(1)	2.75(12)
Ru(1)-N(4)	2.109(8)
Ru(1)-N(3)	2.093(7)
N(3)-N(4)	1.358(10)
Ru(1)-C(9)	2.198(10)
Ru(1)-C(7)	2.198(9)
Ru(1)-C(6)	2.205(10)
Ru(1)-C(5)	2.215(10)
Ru(1)-C(8)	2.259(10)
Ru(1)-C(10)	2.272(10)
Bond Angles (°)	
N(4)-Ru(1)-N(3)	82.7(3)
Ru(1A)-Ru(1)-N(3)	70.6(6)
Ru(1A)-Ru(1)-N(3)	70.6(3)
N(4A)-N(3)-Ru(1)	109.9(6)
N(3)-N(4A)-Ru(1A)	108.7(5)

3.5: REFERENCES

1. M. S. Mudholkar and L. T. Thompson, *J. Appl. Phys.*, 1995, **77**, 5138-5143.
2. S. L. Roberson, D. Finello and R. F. Davis, *Thin Solid Films*, 1998, **324**, 30-36.
3. R. Fix, R. G. Gordon and D. M. Hoffman, *Thin Solid Films*, 1996, **288**, 116-119.
4. M. Damayanti, *J. Electrochem. Soc.*, 2006, **153**, J41.

5. Y. H. Song, Y. L. Chen, Y. Chi, C. S. Liu, W. L. Ching, J. J. Kai, R. S. Chen, Y. S. Huang and A. J. Carty, *Chemical Vapor Deposition*, 2003, **9**, 162-169.

6. J. Shin, A. Waheed, K. Agapiou, W. A. Winkenwerder, H.-W. Kim, R. A. Jones, G. S. Hwang and J. G. Ekerdt, *J. Am. Chem. Soc.*, 2006, **128**, 16510-16511.

7. J. H. Rivers, L. J. DePue Anderson, C. M. N. Starr and R. A. Jones, *Dalton Transactions*, 2012, **41**, 5401-5408.

8. L. McElwee-White, *Dalton Transactions*, 2006, **0**, 5327-5333.

9. W. J. McCarty, X. Yang, L. J. D. Anderson and R. A. Jones, *Dalton Transactions*, 2012, **41**, 173-179.

10. I. Jipa, K. Danova, N. Popovska, M. A. Siddiqi, R. A. Siddiqui, B. Atakan, T. Cremer, F. Maier, H. Marbach, H.-P. Steinruck, F. W. Heinemann and U. Zenneck, *J. Mater. Chem.*, 2011, **21**, 3014-3024.

11. Y. Chi, E. Lay, T. Y. Chou, Y. H. Song and A. J. Carty, *Chemical Vapor Deposition*, 2005, **11**, 206-212.

12. T. Ando, N. Nakata, K. Suzuki, T. Matsumoto and S. Ogo, *Dalton Transactions*, 2012, **41**, 1678-1682.

13. Y. Chi, H.-L. Yu, W.-L. Ching, C.-S. Liu, Y.-L. Chen, T.-Y. Chou, S.-M. Peng and G.-H. Lee, *J. Mater. Chem.*, 2002, **12**, 1363-1369.

14. P. Pertici, G. Vitulli, M. Paci and L. Porri, *Journal of the Chemical Society, Dalton Transactions*, 1980, 1961-1964.

15. G. L. Hardgrove, Templeton, D. H.,, *Acta Crystallographica*, 1959, **12**, 28-32.

16. A. G. Walstrom, M. Pink, X. Yang and K. G. Caulton, *Dalton Transactions*, 2009, **0**, 6001-6006.

17. A. J. Deeming, S. S. Ullah, A. J. P. Domingos, B. F. G. Johnson and J. Lewis, *Journal of the Chemical Society, Dalton Transactions*, 1974, **0**, 2093-2104.

18. E. A. Trifonova, D. S. Perekalin, K. A. Lyssenko and A. R. Kudinov, *J. Organomet. Chem.*, 2013, **727**, 60-63.

19. C. H. Wang, L. F. Xu, X.-L. Fan and J.-T. Wang, *Phys. Lett. A*, 2011, **375**, 562-567.

20. L. Calucci, F. G. N. Cloke, U. Englert, P. B. Hitchcock, G. Pampaloni, C. Pinzino, F. Puccini and M. Volpe, *Dalton Transactions*, 2006, 4228-4234.

21. O. Renn and L. M. Venanzi, *Helv. Chim. Acta*, 1995, **78**, 993-999.

Chapter 4: The Use of X-ray Photoelectron Spectroscopy for Analysis of Films Grown from CVD Precursors

4.1: INTRODUCTION

4.1.1: Overview

X-ray photoelectron spectroscopy (XPS) is a surface analysis technique that allows chemical identification of the elements in the top few atomic layers of a sample by analyzing the binding energies of the electrons associated with the atoms present in the sample (Figure 1). Binding energies not only differ between elements but also vary with the bonding conditions in which the element is found, providing information on what species are present in and on the surface and providing quantitative measurements of the compositions of those elements.

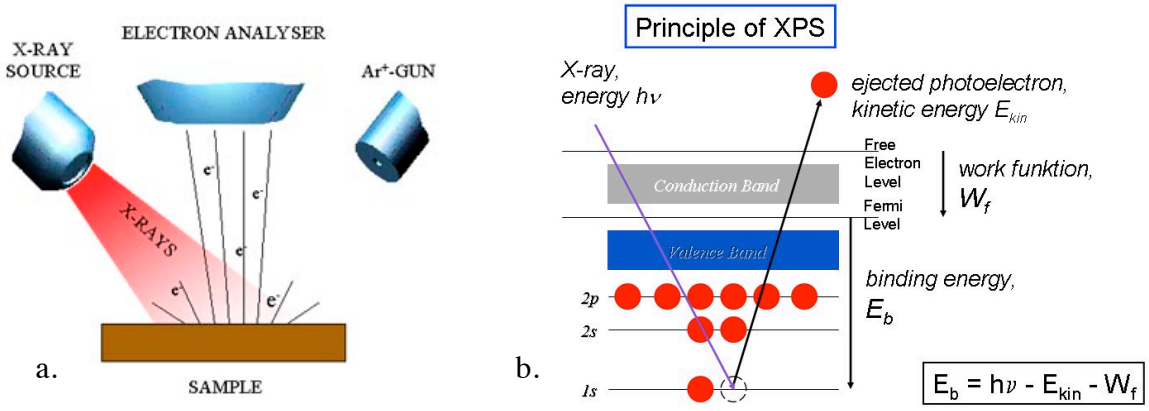

Figure IV-1. a) XPS illustration of inside instrumentation and b) diagram of the principle of XPS and how the binding energies are determined.[1]

XPS is an important technique for measuring surface chemistry and surface composition in a variety of chemical and engineering fields including metal/polymer interfaces,[2] carbon fiber composites,[3] catalytic surfaces[4] and self-assembled monolayers.[5] It continues to be an important technique for studying microelectronic devices and materials.[6,7] As the size of the components in microelectronic devices continues to shrink, the chemical composition of the films becomes more important creating a need for more

sophisticated techniques in small area analysis. Depth profiling by sputtering with Ar^+ ions is also used to determine the composition and purity of films as well as determine purity in other materials such as tinplates,[8] steel,[9] and metallic Ru thin films.[10]

XPS combined with low energy Ar^+ sputtering techniques is a popular surface spectroscopic technique used to investigate the depth profiles of material surfaces. It can be employed to analyze chemical composition at different depths of a material surface with the thickness of tens of nanometers. Surface analysis of CVD films has been crucial to understanding the chemistry behind deposition of different compounds.

Sputtering and depth profiling of films has been important work in the Jones group to determine the purity, consistency of layers, and chemical composition of thin films of amorphous metals and metal alloys. The work described in this chapter is focused on the use of XPS to establish the correlations between metal precursor and deposition parameters (temperature, pressure, carrier gas, etc.) and the chemical compositions of thin films comprising Rh, Ru, and Ni. A table which provides a summary of correlations between precursor chemistry and the material properties of films is provided in on page 92 (Table IV-18).

4.2: Results and Discussion

4.2.1: Analysis of Rh films

Thin films of rhodium are used for electrical contacts,[11] catalysis,[12] and reflective coatings.[13] Previous studies have primarily focused on volatile compounds that feature traditional ligands such as CO, C_5H_5, and trifluoroacetylacetonate (tfac). The precursors in this chapter focus on using the ligands bis(trifluoromethyl)pyrazolate 3,5-($(CF_3)_2$-Pz), bis(trifluoromethyl)pyrrolyl (3,4-$(CF_3)_2$-Pyr) and PMe_3 and their use in developing CVD precursors of metallic thin films. The Rh precursors **4-I – 4-III** were synthesized by

Joseph Rivers in the Jones group and films grown from these compounds were analyzed by XPS (Figure IV-2).[14]

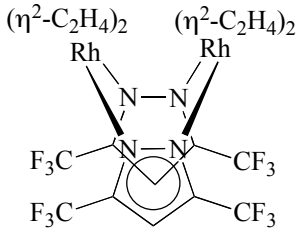

4-I

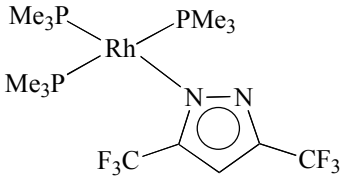

4-II

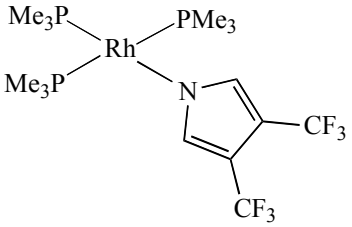

4-III

Figure IV-2: Structures of $[Rh(3,5\text{-}(CF_3)_2\text{-}Pz)(\eta^2\text{-}C_2H_4)_2]_2$ (**4-I**), $Rh(PMe_3)_3(3,5\text{-}(CF_3)_2\text{-}Pz)$ (**4-II**), and $Rh(PMe_3)_3(3,4\text{-}(CF_3)_2\text{-}Pyr)$ (**4-III**)

Thin films of Ru were grown from complexes **4-I**, **4-II**, and **4-III** at various temperatures in a hot-wall CVD reactor with ultra-high purity argon or hydrogen as the carrier gas. Thin films were deposited on native 400 nm SiO_2/Si(100) substrates on a surface of area 4 mm by 8 mm. A summary of deposition conditions are given in Table IV-1.

Table IV-1: Deposition conditions for Rh CVD precursors **4-I** – **4-III**.

Precursor		Carrier Gas/flow rate (sccm)	Precursor Temp (^oC)	Substrate Temp (^oC)	Deposition Time (min.)
$[Rh\ (3,5\text{-}(CF_3)_2\text{-}Pz)(\eta^2\text{-}C_2H_4)_2]_2$	**(4-I)**	Ar, 7	170	500	60
$Rh(PMe_3)_3(3,5\text{-}(CF_3)_2\text{-}Pz)$	**(4-II)**	Ar, 7	130	350	30
$Rh(PMe_3)_3(3,4\text{-}(CF_3)_2\text{-}Pyr)$	**(4-III)**	Ar, 7	120	300	30
$[Rh\ (3,5\text{-}(CF_3)_2\text{-}Pz)(\eta^2\text{-}C_2H_4)_2]_2$	**(4-I)**	H_2, 11	170	500	45
$Rh(PMe_3)_3(3,5\text{-}(CF_3)_2\text{-}Pz)$	**(4-II)**	H_2, 11	130	350	45

Complex **4-I** was synthesized via a salt elimination pathway involving the reaction of $(3,5\text{-}(CF_3)_2\text{-}PzLi$ with $[Rh(C_2H_4)_2Cl]_2$ in the presence of ethylene

(Scheme IV-1). This compound utilizes 3,5-$(CF_3)_2$-Pz, as a ligand which is known to produce volatile CVD precursors (see Chapter 2). The films grown using Ar as the carrier gas were crystalline and metallic in appearance and compositional analysis revealed moderate amounts of Rh with high levels of C present throughout the films (Table IV-2). The film was sputtered at 30 second intervals and analyzed until a large amount of O was noticeable which is attributed to the surface of the SiO_2/silicon substrate.

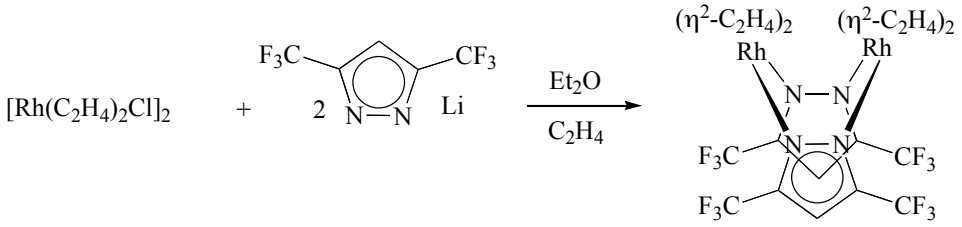

4-I

Scheme IV-1: Synthesis of [Rh(3,5-$(CF_3)_2$-Pz)(η^2-$C_2H_4)_2$]$_2$ **4-I**.

Table IV-2: Compositional analysis of the film using [Rh(3,5-$(CF_3)_2$-Pz)(η^2-$C_2H_4)_2$]$_2$ (**4-I**) as the precursor under Ar.

Sputtering (seconds)	% Rh	% N	% F	% O	% C
0	2.38	15.49	10.74	3.10	61.29
30	7.06	9.49	1.84	0	81.61
60	10.83	10.72	1.25	0	77.19
90	14.48	6.69	0	0	78.83
150	17.48	5.04	0	0	77.48
210	17.87	6.50	0	0	75.63
270	16.19	7.64	0	0	76.18
390	14.13	3.69	0	25.83	38.41

Using H_2 as the carrier gas to deposit **4-I** the amount of C present in the cyrstalline films was reduced substantially from an average 78.3 % to 41.9 % giving an overall

amount of Rh of 58.1 % (Table IV-3). Clearly, the lower levels of C present in these films is due to the change in carrier gas. Here, the hydrogenation of ethylene to give ethane as a volatile by-product is no doubt responsible for the lower C concentration.

Table IV-3: Compositional analysis of the film using $[Rh(3,5\text{-}(CF_3)_2\text{-}Pz)(\eta^2\text{-}C_2H_4)_2]_2$ (**4-I**) as the precursor under H_2.

Sputtering (seconds)	% Rh	% N	% F	% O	% C	% Si
0	18.07	1.80	19.65	4.65	55.82	0
30	46.01	0	0	0	53.99	0
60	52.12	0	0	0	47.88	0
120	58.14	0	0	0	41.86	0
210	54.74	0	0	0	22.51	24.72
240	27.04	0	0	0	16.69	56.27
300	17.13	0	0	0	8.62	74.25

Treatment of $[Rh(COD)(\mu\text{-}3,5\text{-}(CF_3)_2\text{-}Pz]_2$ with PMe_3 gives **4-II** in high yield (Scheme IV-2). This compound utilizes $3,5\text{-}(CF_3)_2\text{-}Pz$, and PMe_3 as ligands that are known to produce volatile CVD precursors (see Chapter 2). Films grown using Ar as the carrier gas were amorphous and metallic in appearance and compositional analysis revealed high levels of Rh (64.5 %) with moderate amounts of C (16.1 %) present throughout the films (Table IV-4). Continuous sputtering revealed that the C content decreases with increasing distance from the surface. The presence of P is fairly constant throughout the film (11.2 %) which is similar to the films grown using the complex *cis*-$(H)_2Ru(PMe_3)_4$[14,15] However, the presence of Si was detected after sputtering 60 seconds through the film indicating that although the film is mostly Rh, it is very thin (c.a. 150-200 nm) compared to other Rh films that have been previously analyzed.

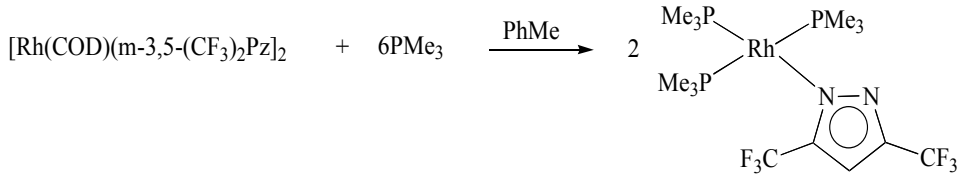

4-II

Scheme IV-2: Synthesis of $Rh(PMe_3)_3(3,5\text{-}(CF_3)_2\text{-}Pz)$ **4-II.**

Table IV-4: Compositional analysis of the film using $Rh(PMe_3)_3(3,5\text{-}(CF_3)_2\text{-}Pz)$ (**4-II**) as the precursor under Ar.

Sputtering (seconds)	% Rh	% P	% C	% Si
60	58.98	13.02	24.98	3.04
120	64.53	11.20	16.07	8.20
180	61.16	10.17	11.71	16.97

CVD precursor **4-II,** using H_2 as the carrier gas, deposited an amorphous film of uniform thickness (250 nm) with a pink metallic color. It did not result in significant reduction of the level of C throughout the film as was seen with complex **4-I** (Table IV-5). This is not surprising, as **4-II** does not have ethylene bound to it as **4-I** does. Initial sputtering of Ar^+ for 15 seconds removed the surface contaminants and continuous depth profiling proved to give a film containing C in moderate composition at 15 %, with the majority of the film as Rh (67 %) and moderate levels of P (17 %).

Table IV-5: Compositional analysis of the film using $Rh(PMe_3)_3(3,5\text{-}(CF_3)_2\text{-}Pz)$ (**4-II**) as the precursor under H_2.

Sputtering (seconds)	% Rh	% P	% F	% O	% C	% Si
0	28.70	9.81	2.89	22.47	36.13	0
15	53.97	21.54	0	0	24.44	0
30	61.49	21.40	0	0	17.11	0
45	66.57	17.98	0	0	15.45	0
60	67.91	18.28	0	0	13.81	0
90	67.70	16.75	0	0	15.54	0
120	67.04	17.94	0	0	15.02	0
180	68.21	14.43	0	0	17.36	0
240	58.98	13.21	0	0	24.98	3.04
300	64.53	11.20	0	0	16.07	8.20
360	61.16	10.17	0	0	11.71	16.97

Reaction of $[Rh(COD)Cl_2]_2$ in the presence of PMe_3 with $3,4\text{-}(CF_3)_2$-PyrNa gives **4-III** in high yield (72 %) (Scheme IV-3). Using this compound as the precursor, films grown under Ar were crystalline and metallic in appearance with a film thickness of 50-70 nm. Compositional analysis showed that the bulk of the film was RhP with the level of carbon increasing slightly during continuous sputtering from 19.9 % of 26.2 % (Table IV-6). The film was sputtered over 30 second intervals and analyzed until Si was detected which is attributed to the surface of the Silicon substrate.

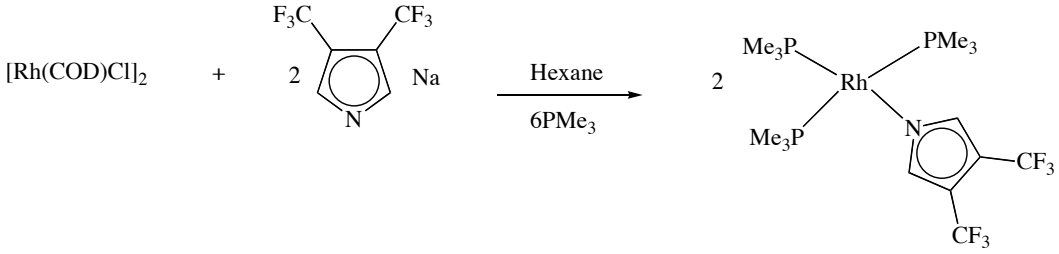

4-III

Scheme IV-3: Synthesis of $Rh(PMe_3)_3(3,4\text{-}(CF_3)_2\text{-}Pyr)$ (**4-III**).

Table IV-6: Compositional analysis of the film using $Rh(PMe_3)_3(3,4\text{-}(CF_3)_2\text{-Pyr})$ (**4-III**) as the precursor under Ar.

Sputtering (seconds)	% Rh	% P	% C	% O
0	10.98	15.79	33.86	39.37
30	55.81	24.29	19.90	
60	60.89	21.85	17.26	
120	55.76	23.30	20.94	
180	55.07	20.25	24.69	
300	58.32	15.53	26.15	

The deposition of **4-III** using H_2 as the carrier gas did reveal a reduction of the presence of C throughout the film from 20 % using Ar to 14 % with H_2 (Table IV-7). This is possibly due to the difference in volatility of $3,5\text{-}(CF_3)_2$-Pz and $3,4\text{-}(CF_3)_2$-Pyr where the pyrrole sublimes at 25 ^{0}C under 0.1 torr and the pyrazole sublimes at 40 ^{0}C under 0.1 torr. The more volatile pyrrole by-product would be removed from the vicinity of the grainy surface more effectively and be less likely to be incorporated into the film. There is no presence of F in the films from precursors having $3,5\text{-}(CF_3)_2$-Pz ligands or from those having the $3,4\text{-}(CF_3)_2$-Pyr.

Table IV-7: Compositional analysis of the film using $Rh(PMe_3)_3(3,4\text{-}(CF_3)_2\text{-Pyr})$ (**4-III**) as the precursor under H_2.

Sputtering (seconds)	% Rh	% P	% C	% O
0	22.44	42.02	13.22	22.31
30	57.06	25.44	17.49	
60	54.93	26.91	18.17	
150	57.66	34.32	14.03	
295	54.12	33.69	12.19	

At this point it becomes clear that the use of H_2 instead of Ar as the carrier gas results in improved films with lower carbon concentration. The next set of experiments were therefore conducted solely with H_2 as the carrier gas. The Rh precursors **4-IV** – **4-VI** were synthesized by W. Jeffrey McCarty in the Jones group and films grown from these compounds were analyzed by XPS (Figure IV-3).

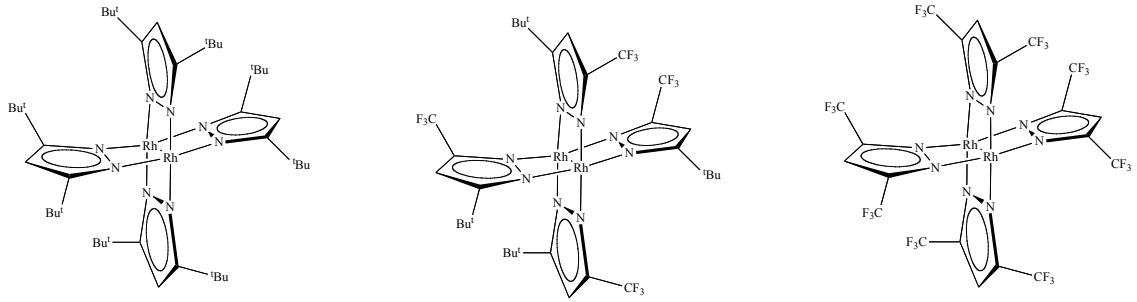

4-IV **4-V** **4-VI**

Figure IV-3: Structures of $Rh_2(\mu\text{-}3,5\text{-}(^tBu)_2Pz)_4$ (**4-IV**), $Rh_2(\mu\text{-}3\text{-}(CF_3),5\text{-}(^tBu)Pz)_4$ (**4-V**), and $Rh_2(\mu\text{-}3,5\text{-}(CF_3)_2Pz)_4{\cdot}2H_2O$ (**4-VI**).

Thin films of Rh were grown from complexes **4-IV**, **4-V**, and **4-VI** at various temperatures in a hot-wall CVD reactior with ultra-high purity H_2 as the carrier gas. Thin films were deposited on native 400 nm SiO_2/Si(100) substrates on a surface are of 4 mm by 6 mm. A summary of deposition conditions are given in Table IV-8.

Table IV-8: Deposition conditions for Rh CVD precursors **4-IV** – **4-VI**.

Precursor		Carrier Gas/flow rate (sccm)	Precursor Temp (^oC)	Substrate Temp (^oC)	Deposition Time (min.)
$Rh_2(\mu\text{-}3,5\text{-}(^tBu)_2Pz)_4$	**(4-IV)**	H_2, 11	210	550	30
$Rh_2(\mu\text{-}3\text{-}(CF_3),5\text{-}(^tBu)Pz)_4$	**(4-V)**	H_2, 9	180	400	45
$Rh_2(\mu\text{-}3,5\text{-}(CF_3)_2Pz)_4{\cdot}2H_2O$	**(4-VI)**	H_2, 8	140	400	45

Complexes **4-IV** – **4-VI** were synthesized via the reactions of 3,5-substituted pyrazolates with $Rh_2(OAc)_4$ at -78 ^0C in good yields (75-90 %) and showed sufficient volatility at 0.2 torr to be investigated for CVD experiments (Scheme IV-4). These compounds utilize 3,5-$(CF_3)_2$-Pz and related pyrazolate derivatives. The films grown

under H_2 were crystalline and metallic in appearance with an average thickness of 30-50 nm. Compositional analysis and depth profiling revealed high amounts of Rh with moderate amounts of C present varying depending upon the pyrazolate derivative.

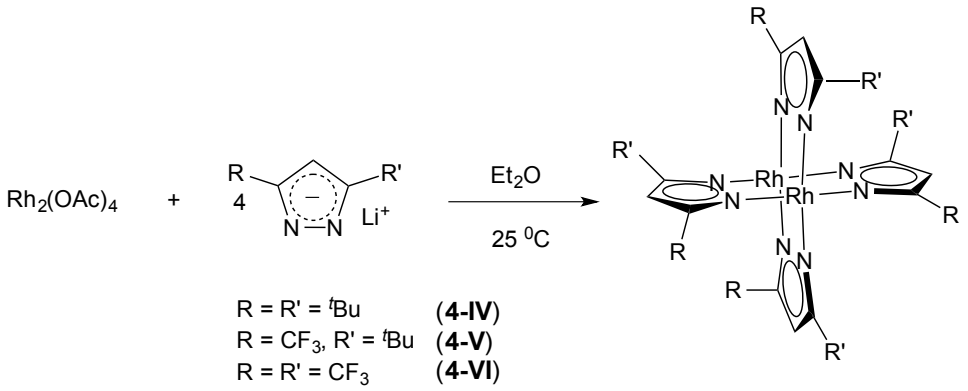

Scheme IV-4: Synthesis of **4-IV**, **4-V**, and **4-VI**.

Depth profiling of complex **4-IV** revealed a significant drop in C during continuous Ar^+ sputtering. Overall the film began with a carbon content of 42 % and ended with 15 % at the lowest point. The surface of the film was 50 % Rh which after depth profiling increased to 82 %. Compositional analysis is shown in Table IV-9.

Table IV-9: Compositional analysis of the film using $Rh_2(\mu\text{-}3,5\text{-}(^tBu)_2Pz)_4$ (**4-IV**) as the precursor under H_2.

Sputtering (seconds)	% Rh	% C	% O
0	50.30	41.72	7.98
30	58.52	34.38	7.10
45	71.38	21.39	7.23
60	75.49	18.43	6.08
90	77.34	16.98	5.68
120	81.86	14.62	3.52

Depth profiling of complex **4-V** revealed a moderate reduction in the C content during continuous Ar^+ sputtering. Overall the film began with a carbon content of 35 %

and ended with 24 % at the lowest point. The surface of the film was 53 % Rh which after depth profiling increased to 72 %. Compositional analysis is shown in Table IV-10.

Table IV-10: Compositional analysis of the film using $Rh_2(\mu\text{-}3\text{-}(CF_3),5\text{-}(^tBu)Pz)_4$ (**4-V**) as the precursor under H_2.

Sputtering (seconds)	% Rh	% C	% O
0	53.20	35.16	11.64
30	69.32	22.38	8.30
45	70.18	23.42	6.40
60	71.76	23.86	4.38
120	72.41	24.18	3.41

Depth profiling of complex **4-V** revealed the largest decrease in C content during continuous Ar^+ sputtering. Overall the film began with a carbon content of 37 % and ended with 5 % at the lowest point. The surface of the film was 49 % Rh which after depth profiling increased to 91 %. The film grown using this CVD precursor has the highest Rh content and lowest C content compared to the other two. It is believed to be the case due to the use of the 3,5-$(CF_3)_2$-Pz ligand which has two volatile CF_3 groups and with the use of H_2 as the carrier gas the ligand could be easily transported away from the growing film with other by-products rather than decomposing onto the substrate. Compositional analysis is shown in Table IV-11.

Table IV-11: Compositional analysis of the film using $Rh_2(\mu\text{-}3,5\text{-}(CF_3)_2Pz)_4{\cdot}2H_2O$ (**4-VI**) as the precursor under H_2.

Sputtering (seconds)	% Rh	% C	% O
0	48.72	36.98	14.30
30	59.17	28.63	12.47
45	66.38	25.69	7.93
60	71.79	21.39	6.82
90	84.01	10.17	5.82
120	91.08	5.42	3.51

Several Rh(II) paddlewheel complexes were used as CVD precursors and underwent surface analysis by XPS of composition. Variation of the 3- and 5- positions on the pyrazolate affected the composition of Rh, C, and O in films grown. Complex **4-VI** contained the most Rh and the least amount of C while **4-IV** and **4-V** each contained less Rh and more C than **4-VI** as shown in Table IV-12.

Table IV-12: Comparison after sputtering films grown from **4-IV** – **4-VI** for 120 seconds

Precursor		% Rh	% C	Result
$Rh_2(\mu\text{-}3,5\text{-}(^tBu)_2Pz)_4$	**(4-IV)**	81.86	14.62	Moderate levels of C
$Rh_2(\mu\text{-}3\text{-}(CF_3),5\text{-}(^tBu)Pz)_4$	**(4-V)**	72.41	24.18	High levels of C
$Rh_2(\mu\text{-}3,5\text{-}(CF_3)_2Pz)_4{\cdot}2H_2O$	**(4-VI)**	91.08	5.42	Low levels of C

4.2.2: Analysis of Ru films

Ru CVD precursors have been previously reported to have a strong influence on the film morphology (Chapter 2 and 3).[15, 16] The incorporation of P from the use of PMe_3 as a ligand is believed to interfere with crystalline formation as films are deposited and this results in amorphous alloys, showing no long-range order. The compounds **4-VII** and **4-VIII** are ruthenium hydrides and were synthesized by Dr. W. Jeffrey McCarty using various phosphorus donor ligands for use as single source CVD precursors (Figure IV-4).

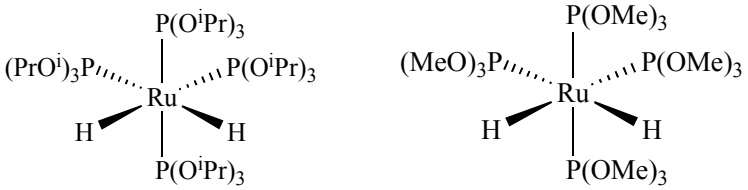

4-VII **4-VIII**

Figure IV-4: Structures of *cis*-$H_2Ru(P(O^iPr)_3)_4$ (**4-VII**) and *cis*-$H_2Ru(P(OMe)_3)_4$ (**4-VIII**).

Thin films of Ru were grown from complexes **4-III** and **4-VIII** at various temperatures in a hot-wall CVD reactior with ultra-high purity hydrogen as the carrier gas. Amorphous thin films of golden hue were deposited on native 400 nm SiO_2/Si(100) substrates on a surface of area 4 mm by 6 mm. A summary of deposition conditions is given in Table IV-13.

Table IV-13: Deposition conditions for Ru CVD precursors **4-VII** – **4-VIII**.

Precursor		Carrier Gas/flow rate (sccm)	Precursor Temp (^oC)	Substrate Temp (^oC)	Deposition Time (min.)
cis-$H_2Ru(P(O^iPr)_3)_4$	**(4-VII)**	H_2, 10	120	420	30
cis-$H_2Ru(P(OMe)_3)_4$	**(4-VIII)**	H_2, 13	85	350	30

The two *cis*-$H_2Ru(P(OR)_3)_4$ (R = ^{i}Pr, Me) complexes were synthesized by refluxing $RuCl_3 \cdot nH_2O$ and the corresponding trialkyl phosphite in methanol and reducing the mixture with $NaBH_4$ to give **4-VII** and **4-VIII** in moderate yields (50-60 %) (Scheme IV-5).

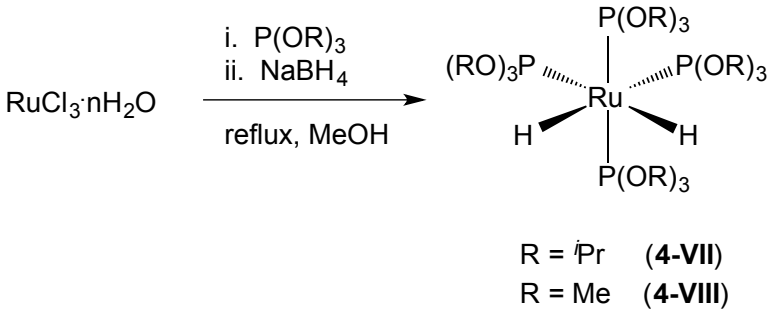

Scheme IV-5: Synthesis of *cis*-$H_2Ru(P(O^iPr)_3)_4$ (**4-VII**) and *cis*-$H_2Ru(P(OMe)_3)_4$ (**4-VIII**).

XPS depth profiling was used to analyze the composition of the film grown from precursor **4-VII**. The surface was sputtered to reveal consistent layers of RuP with substantial amount of O present above 30 % for the whole film. This is not seen in films

of other CVD precursors and is most likely due to the O in the phosphite ligand. Over time the film changes from a ratio of 1:1 for Ru:P to 1.6:1 for Ru:P. Results are shown in Table IV-14.

Table IV-14: Compositional analysis of the film using *cis*-$H_2Ru(P(O^iPr)_3)_4$ (**4-VII**) as the precursor under H_2.

Sputtering (seconds)	% Ru	% P	% O
0	8.69	24.18	67.12
30	15.53	26.30	58.17
60	23.76	25.86	50.39
120	32.47	22.38	45.15
180	34.38	20.85	39.00

XPS depth profiling was used to analyze the composition of the film grown from precursor **4-VIII**. The surface was sputtered to reveal consistent layers of RuP with increased levels of O present around 50 %, which is 20 % more than found in the film grown from **V-II**. The amount of Ru present in this film is also reduced to above 20 %. It is interesting to note that over time the film changes from a ratio of 1:2 for Ru:P to 1:1 for Ru:P. Results are shown in Table IV-15.

Table IV-15: Compositional analysis of the film using *cis*-$H_2Ru(P(OMe)_3)_4$ (**4-VIII**) as the precursor under H_2.

Sputtering (seconds)	% Ru	% P	% O
0	11.25	25.01	63.73
30	14.58	29.20	56.21
60	18.42	29.00	52.47
120	21.16	30.08	48.76
180	23.80	27.48	48.72

The use of trialkyl phosphite ligands as P donor ligands proved useful to develop films of amorphous phases and the incorporation of P into the films. These ligands are less expensive and air stable when compared to their corresponding trialkylphosphines.

4.2.3: Analysis of Ni films

Films of Ni are of importance for a variety of applications including microelectronics, corrosion-resistant coatings, solar cell materials, semiconductor interfaces, and novel magnetic properties.[17-22] There is therefore increasing interest in the development of single source CVD precursors for deposition of thin films of Ni. The compounds *trans*-Ni(PMe_3)$_2$(3,5-(CF_3)$_2$-Pz)$_2$ (**4-IX**) and *trans*-Ni(PEt_3)$_2$(3,5-(CF_3)$_2$-Pz)$_2$ (**4-X**) were synthesized by Dr. Joseph Rivers using various trialkyl phosphine donor ligands to synthesize single source CVD precursors (Figure IV-5).

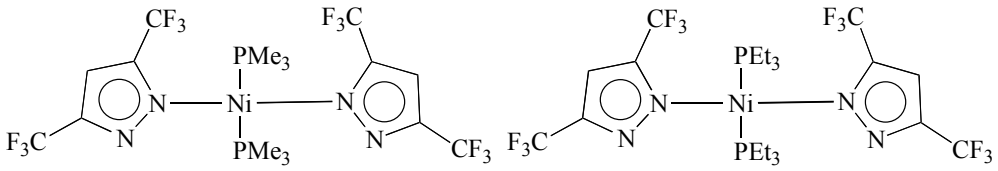

4-IX **4-X**

Figure IV-5: Structures of *trans*-Ni(PMe_3)$_2$(3,5-(CF_3)$_2$-Pz)$_2$ (**4-IX**) and *trans*-Ni(PEt_3)$_2$(3,5-(CF_3)$_2$-Pz)$_2$ (**4-X**).

Thin films of Ni were grown from complexes **4-IX** and **4-X** at various temperatures in a hot-wall CVD reactior with ultra-high purity argon as the carrier gas. Crystalline thin films with a pink hue were deposited on native 400 nm SiO_2/Si(100) substrates on a surface of 4 mm by 6 mm. A summary of deposition conditions are given in Table IV-15.

Table IV-15: Deposition conditions for Ni CVD precursors **4-IX** – **4-X**.

Precursor		Carrier Gas/flow rate (sccm)	Precursor Temp (^{o}C)	Substrate Temp (^{o}C)	Deposition Time (min.)
trans-Ni$(PMe_3)_2(3,5\text{-}(CF_3)_2\text{-}Pz)_2$	**(4-IX)**	Ar, 7	120	300	30
trans-Ni$(PEt_3)_2(3,5\text{-}(CF_3)_2\text{-}Pz)_2$	**(4-X)**	Ar, 7	130	350	30

trans-Ni$(PMe_3)_2(3,5\text{-}(CF_3)_2\text{-}Pz)_2$ (**4-IX**) was synthesized via traditional lithium salt elimination reaction pathways using two equivalents of the lithiated $3,5\text{-}(CF_3)_2$-Pz and $Ni(PMe_3)_2Cl_2$ at -78 ^{0}C to give moderate yields (63 %) of **4-IX** (Scheme IV-6). **4-IX** was found to have suitable volatilities and could sublime under vacuum to be a viable CVD precursor.

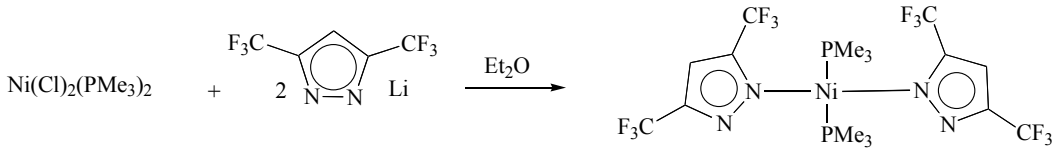

Scheme IV-6: Synthesis of *trans*-Ni$(PMe_3)_2(3,5\text{-}(CF_3)_2\text{-}Pz)_2$ (**4-IX**).

XPS depth profiling was used to analyze the composition of the film grown from precursor **4-IX**. The surface was sputtered to reveal a film with composition consisting of Ni, C, N, O, and F (Table IV-16). It is surprising that with the presence of a trialkyl phosphine ligand that there is no P in the film. The film was sputtered until the presence of the silicon substrate was detected.

Table IV-16: Compositional analysis of the film using *trans*-Ni$(PMe_3)_2(3,5\text{-}(CF_3)_2\text{-}Pz)_2$ (**4-IX**) as the precursor under Ar.

Sputtering (seconds)	% Ni	% F	% N	% C	% O	% Si
0	3.65	8.60	15.95	67.12	4.68	
30	4.45	1.72	12.55	80.12	1.16	
60	2.70	1.94	10.63	80.52	2.74	1.47
95	3.56	1.80	7.94	77.00	5.98	3.71

trans-Ni$(PEt_3)_2$(3,5-$(CF_3)_2$-Pz)$_2$ (**4-X**) was prepared via traditional lithium salt elimination reaction pathways using two equivalents of the lithiated 3,5-$(CF_3)_2$-Pz and $Ni(PEt_3)_2Cl_2$ at -78 ^{0}C to give good yields (81 %) of **4-X** (Scheme IV-7). **4-X** was found to have suitable volatilities and sublimed under vacuum to be a viable CVD precursor.

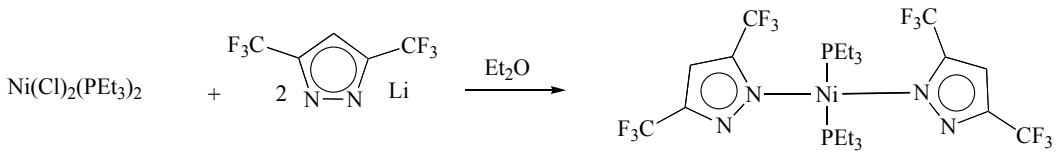

Scheme IV-7: Synthesis of *trans*-Ni$(PEt_3)_2$(3,5-$(CF_3)_2$-Pz)$_2$ (**4-X**).

XPS depth profiling was used to analyze the composition of the film grown from precursor **4-X**. The surface was sputtered to reveal a film with composition consisting of Ni, C, N, F, and O (Table IV-17). Again, it is surprising that with the presence of a trialkyl phosphine ligand that there is no P in the film. The film was sputtered until the presence of the silicon substrate was detected.

Table IV-17: Compositional analysis of the film using *trans*-Ni$(PEt_3)_2$(3,5-$(CF_3)_2$-Pz)$_2$ (**4-X**) as the precursor under Ar.

Sputtering (seconds)	% Ni	% F	% N	% C	% O	% Si
0	17.46	24.17	10.06	40.36	7.95	
10	18.31	23.15	10.44	45.79	2.31	
48	15.44	12.12	9.92	60.61	1.91	
98	11.35	7.12	9.54	70.54	1.46	
150	10.12	5.11	9.56	73.47	1.74	
180	7.88	4.46	8.81	77.29	1.54	
480	8.03	4.37	9.40	76.10	1.21	0.89

The 3,5-$(CF_3)_2$-Pz ligand coordinated to a variety of transition metals can provide suitable compounds as volatile CVD precursors. The use of H_2 as the carrier gas should be explored as it is likely that films would contain different elemental compositions. It is

interesting to note that in the films of **4-IX** and **4-X** the presence of P was not observed despite each compound having two trialkyl phosphines, it would be beneficial to the comparison of carrier gases to see if P is present in films grown using H_2.

4.2.4: Conclusions and Future Studies

In this work, focus was on the use of different organometallic CVD precursors and how their molecular structure affected the morphology and elemental composition of films grown using them. Using trialkyl phosphines or trialkyl phosphite ligands the incorporation of P into film content prevented crystalline formation to occur giving films of amorphous nature. This appears to work for CVD precursors of Ru and Rh, while the CVD precursors of Ni with phosphorus ligands did not grow films with any P content.

The use of the two different carrier gases, H_2 and argon, gave different results in overall film composition (Summary of results in Table IV-18, next page). Using H_2 reduces the amount of C present in the films but it will, at times, react with the precursor in the vapor phase of the precursor preventing film growth from occurring. Thus, screening for future CVD precursors must also include selection between those that are resistant to hydrogenation in the vapor phase while moving through the CVD reactor versus those which react with H_2 in the vapor phase in which case Ar should be used as the carrier gas. Future work should include the exploration of growing films using the same precursor but changing the carrier gas from Ar to H_2 and working with mixtures of Ar/H_2 to compare the composition of the films grown under different conditions.

Table IV-18: Summary Table: Correlation between precursor chemistry and material properties of grown films

Precursor		Carrier Gas	Composition	Morphology	Result
$[Rh\ (3,5\text{-}(CF_3)_2\text{-}Pz)(\eta^2\text{-}C_2H_4)_2]_2$	**(4-I)**	Ar, H_2	RhNC, RhC	crystalline	Use of H_2 reduces C concentrations
$Rh(PMe_3)_3(3,5\text{-}(CF_3)_2\text{-}Pz)$	**(4-II)**	Ar, H_2	RhPC	amorphous	Ar and H_2 films have similar concentrations
$Rh(PMe_3)_3(3,4\text{-}(CF_3)_2\text{-}Pyr)$	**(4-III)**	Ar, H_2	RhPC	crystalline	Use of H_2 reduces C concentrations
$Rh_2(\mu\text{-}3,5\text{-}(^tBu)_2Pz)_4$	**(4-IV)**	H_2	RhCO	crystalline	Moderate levels of C
$Rh_2(\mu\text{-}3\text{-}(CF_3),5\text{-}(^tBu)Pz)_4$	**(4-V)**	H_2	RhCO	crystalline	High levels of C
$Rh_2(\mu\text{-}3,5\text{-}(CF_3)_2Pz)_4{\cdot}2H_2O$	**(4-VI)**	H_2	RhCO	crystalline	Low levels of C
cis-$H_2Ru(P(O^iPr)_3)_4$	**(4-VII)**	H_2	RuPO	amorphous	Substantial concentration of O
cis-$H_2Ru(P(OMe)_3)_4$	**(4-IIX)**	H_2	RuPO	amorphous	Substantial concentration of O
trans-$Ni(PMe_3)_2(3,5\text{-}(CF_3)_2\text{-}Pz)_2$	**(4-IX)**	Ar	NiFNCO	crystalline	High C concentrations
trans-$Ni(PEt_3)_2(3,5\text{-}(CF_3)_2\text{-}Pz)_2$	**(4-X)**	Ar	NiFNCO	crystalline	High C concentrations

4.3: EXPERIMENTAL

4.3.1: General Synthesis and Film Deposition Conditions

Films were grown in a homemade hot-wall CVD reactor consisting of a quartz deposition zone heated by a tube furnace. Films were deposited on a native 400 nm SiO_2/Si(100). All fittings were VCR metal gasket face sealing connections with stainless steel lines. The precursor was heated in a Pyrex ampoule connected to the system and carried using ultra-high purity argon (99.999%, Airgas) at flow rates of 5-11 sccm with a mass flow controller (Fathom Technologies, 0-50 sccm range). The lines were kept warm with insulated heating tape and wrapped with glass wool and heavy grade aluminum foil. The wafers were cut into approximately 3 mm x 5 mm pieces and positioned on quartz boats inside of the deposition zone. The system was heated overnight under vacuum pressures of 0.1 torr to remove the presence of water and

oxygen. Deposition temperatures below 350 ^{0}C resulted in much of the precursor passing through the inner chamber.

4.3.2: Instrument Details

Film compositions were measured using *ex situ* high-resolution XPS analysis (Kratos AXIS Ultra DLD; monochromatic Al Kα). Depth profiling was achieved by sputtering the film with 4 kV Ar^{+}.

4.4: REFERENCES

1. J. F. Watts and J. Wolstenholme, *An introduction to surface analysis by XPS and AES*, J. Wiley, New York, NY, 2003.

2. P. K. Wu, *MRS Online Proceedings Library*, 1995, **385**, null-null.

3. P. M. A. Sherwood, *J. Electron Spectrosc. Relat. Phenom.*, 1996, **81**, 319-342.

4. N. S. McIntyre, P. A. Spevack and M. J. Walzak, *Journal of Surface Review Letters*, 1995, **2**, 689-699.

5. G. C. Herdt, D. R. Jung and A. W. Czanderna, *Prog. Surf. Sci.*, 1995, **50**, 103-129.

6. S. Pignataro, *Fresenius. J. Anal. Chem.*, 1995, **353**, 227-233.

7. S. Iwata and A. Ishizaka, *J. Appl. Phys.*, 1996, **79**, 6653-6713.

8. S. Chen, L. Xie and F. Xue, *Appl. Surf. Sci.*, 2013, **276**, 454-457.

9. S. Chen, F. Yan, F. Xue, L. Yang and J. Liu, *Mater. Chem. Phys.*, 2010, **124**, 472-476.

10. W. Liao and J. G. Ekerdt, *Chem. Mater.*, 2013, **25**, 1793-1799.

11. H. Lee, *Journal of Microelectronics and Microengineering*, 2006, **16**, 557.

12. F. J. Williams, M. S. Tikhov, A. Palermo, N. Macleod and R. M. Lambert, *The Journal of Physical Chemistry B*, 2001, **105**, 2800-2808.

13. L. Marot, G. De Temmerman, V. Thommen, D. Mathys and P. Oelhafen, *Surface and Coatings Technology*, 2008, **202**, 2837-2843.

14. J. H. Rivers, L. J. DePue Anderson, C. M. N. Starr and R. A. Jones, *Dalton Transactions*, 2012, **41**, 5401-5408.

15. J. Shin, A. Waheed, K. Agapiou, W. A. Winkenwerder, H.-W. Kim, R. A. Jones, G. S. Hwang and J. G. Ekerdt, *J. Am. Chem. Soc.*, 2006, **128**, 16510-16511.

16. J. Shin, A. Waheed, W. A. Winkenwerder, H.-W. Kim, K. Agapiou, R. A. Jones, G. S. Hwang and J. G. Ekerdt, *Thin Solid Films*, 2007, **515**, 529-5307.

17. V. V. Bakovets, V. N. Mitkin and N. V. Gelfond, *Chemical Vapor Deposition*, 2005, **11**, 112-117.

18. A. Panneerselvam, M. A. Malik, M. Afzaal, P. O'Brien and M. Helliwell, *J. Am. Chem. Soc.*, 2008, **130**, 2420-2421.

19. T. Kada, M. Ishikawa, H. Machida, A. Ogura, Y. Ohshita and K. Soai, *J. Cryst. Growth*, 2005, **275**, e1115-e1119.

20. S. T. Oyama, *J. Catal.*, 2003, **216**, 343-352.

21. N. Bahlawane, P. A. Premkumar, Z. Tian, X. Hong, F. Qi and K. Kohse-Huinghaus, *Chem. Mater.*, 2009, **22**, 92-100.

22. R. A. Fischer, W. Scherer, M. Kleine, O. Lehmann and M. Stuke, *Chem. Mater.*, 1995, **7**, 1863-1872.

Chapter 5: Transition Metal Phosphides of MoP_4 for Li Ion Battery Applications

5.1: INTRODUCTION

5.1.1: Overview

The demand for batteries with higher operating voltage, increased energy density, long life cycles, and improved rate capacity has been driven by their increasing use in portable electronic devices as well as electric vehicles.[1-3] Lithiated graphite is currently the most widely used anode in portable devices, but to power electric vehicles or plug-in hybrid electric vehicles the weight, capacity, safety and cost of lithiated graphite is in need of significant improvements.[4] Considerable research has been carried out towards the goals of improving lithium-ion battery anode and cathode materials by producing new materials with morphologies and chemical compositions that allow for fast charge/discharge rates with high capacity. Among them molybdenum oxides undergo intercalation of Li^+ ions into their crystal lattices easily. However, their ability to recharge is moderate and they have a low electrical conductivity.[5, 6] One of the approaches to avoid these problems has been to use molybdenum doped vanadium oxides where the presence of the Mo^{6+} ions in the V_2O_5 lattice increases the surface area of the materials allowing discharge capacity of 150 mAh/g and has a good rate of reversibility.[7,8]

Primary attributes of new materials for lithium-ion batteries include reversible lithium insertion/de-insertion reactions, high capacities, and economical methods of preparation. Lithium-ion batteries made using transition metal phosphides (TMPs) are currently being examined due to their high gravimetric capacities upon reaction with Li. Several studies of TMPs such as TiP_2,[9] NiP_2,[10] and CuP_2[11] have shown promising results. In recent reports Li_7TiP_4, $LiMnP_4$, and FeP_2 have shown to exhibit discharge capacities of 625, 1400, and 906 mAh/g, respectively.[12-14] These capacities are greatly improved when compared to lithiated graphite which has a reversible capacity of 370 mAh/g.[15]

Depending on the nature of the metal and the cutoff voltage region, TMP materials present two lithiating mechanism reactions:

Simple Li-ion intercalation $MP_n + xLi^+ + xe^- \rightarrow Li_xMP_n$ (1)

Conversion reaction $MP_n + xLi^+ + xe^- \rightarrow M(Li_xM) + Li_{1-x}P_n$ (2)

The first, simple Li-ion intercalation (equation 1), can be observed in manganese phosphide MnP_4, where Li-ion intercalation into a layered structure takes place by an electrochemical reduction/oxidation process.[16] However, after 10 cycles the MnP_4 phase starts to decompose into metallic Mn and Li_3P. Therefore, the best candidates for TMP anode materials are ones that allow the conversion reaction mechanism (equation 2) to dominate. The common feature in electrochemically reversible TMP materials is that they have the residual phosphorus atoms directly bonded to the metal ion. The excess Li-ion intercalation leads the formation of Li-P bonding without decomposition. Research in MoP_2 has shown that highly reversible Li-ion redox reactions between MoP_2 and Li_xMoP_2 exist in a wide voltage region.[17]

5.1.2: Synthesis of transition metal phosphides

The following work describes the development of a different synthetic approach for the facile direct synthesis of TMPs in near quantitative yield. Current methods of preparing TMPs include solvothermal processes which employ high pressure and temperatures of 200-300 ^{0}C as well as mechanochemical grinding.[18-20] The synthetic strategy developed in the following research utilizes lower temperatures ranging from room temperature to 100 ^{0}C in a reaction of organometallic complexes of molybdenum with phosphine gas (PH_3) to form amorphous phases of Mo based TMPs. Literature from the 19th and early 20th centuries contains evidence that PH_3 reacts with salts of Cr, U, Mn,

Ni, Co, and Fe to form metal phosphides. These materials were not fully characterized and do not appear to be currently under investigation.[21] Our group has had success in using the low temperature synthetic route, for example, using PH_3 with $Fe(N(SiMe_3)_2)_3$ at 100 ^{0}C to produce FeP_2 that maintains a high conversion capacity after 10 cycles.[14]

The objectives of this research include learning what factors affect TMP morphology and to produce mesoporous materials that allow Li-ion transport using a low temperature preparation. TMPs with high surface area are theorized to allow Li-ion insertion/de-insertion reactions with little change in morphology after each cycle and should show improved performance as battery anode materials. The focus of this work was to find amorphous TMPs of MoP_4 that will undergo the conversion process without changing phase, perform as reversible reactions, and are made using mild conditions.

5.2: RESULTS AND DISCUSSION

The TMP MoP_4 was synthesized from a low-temperature synthetic method involving interaction of phosphine gas with reactive metal alkyl complexes in the following ways: (a) as a powder precipitate from solution, (b) via drop casting followed by evaporation of solvent, and (c) adhered during synthesis on several substrates including copper, steel, ITO slides, and carbon blocks. These materials were then characterized by electron microscopy. Nellymar Membreno in the Stevenson group evaluated their electrochemical properties in battery cells between 1.0 and 4.0 V for use as anode materials for Li-ion batteries.

5.2.1: Synthesis of molybdenum phosphides

Two molybdenum alkyl complexes were synthesized from molybdenum tetraacetate **5-I** (Scheme V-1) as starting materials for generating TMPs. Dimolybdenum tetraacetate **5-I** was originally synthesized by Wilkinson and coworkers in 1964 with a proposed structure[22] which was determined by crystal X-ray diffraction in 1965 by Lawton and Mason.[23] The product was determined to be moisture sensitive thus the

reagents needed to be treated under anhydrous conditions to obtain an optimum yield. However, decomposition occurs relatively slowly over several days to weeks at room temperature making this compound an ideal starting material.

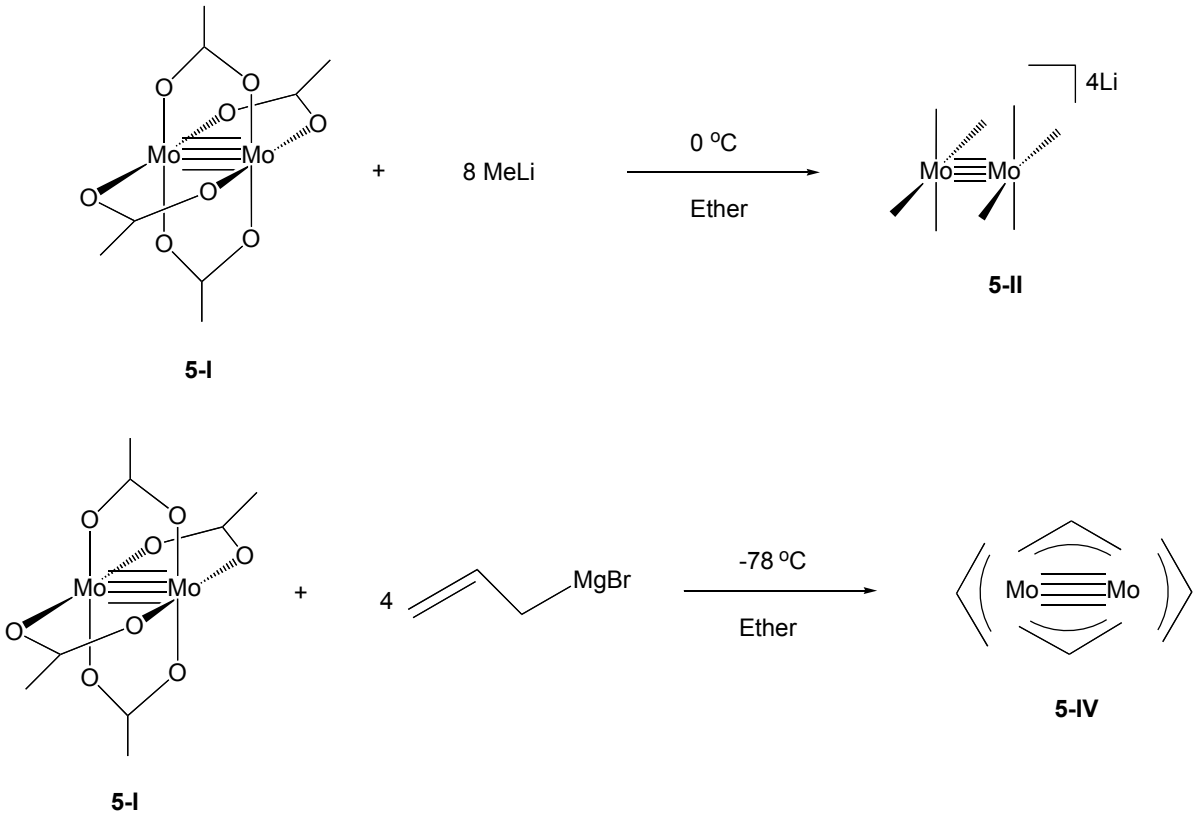

Scheme V-1: Synthesis of $Li_4Mo_2(CH_3)_8$ **5-II** and $Mo_2(C_3H_5)_4$ **5-IV** from $Mo_2(O_2CCH_3)_4$ **5-I**.

Molybdenum phosphide (MoP_4) was synthesized via two routes as seen in Scheme V-2. In a typical synthesis, a solution of the Mo alkyl complex in diethyl ether was transferred to a Fischer-Porter bottle equipped with a pressure regulator and was introduced to a high pressure of phosphine gas which was then heated at 80 ^{0}C.

A series of different reaction conditions was examined for **5-II** and **5-IV**. The solvent was either removed under reduced pressure leaving the Mo alkyl complex in the

solid state on various substrates (copper films, ITO slides, steel films, or bocks of carbon) to which PH_3 was then introduced. Or, the Mo alkyl remained in the diethyl ether solvent from which MoP_4 was precipitated and was isolated as a powder.

Once PH_3 was introduced to the bright red color of **5-II**, a rapid darkening was observed to a black formation of the MoP_4 (Scheme V-2, Route 1). After 24 hours the Fischer-Porter bottle was heated to 80 ^{0}C for several hours to ensure the reaction has gone to completion. Initial results showed that without heating, only the surface of **5-II** had been converted to MoP_4. Under these conditions the unreacted Mo alkyls decomposed during electrochemical analysis and results were inconclusive as the materials were a combination of products.

Route 1:

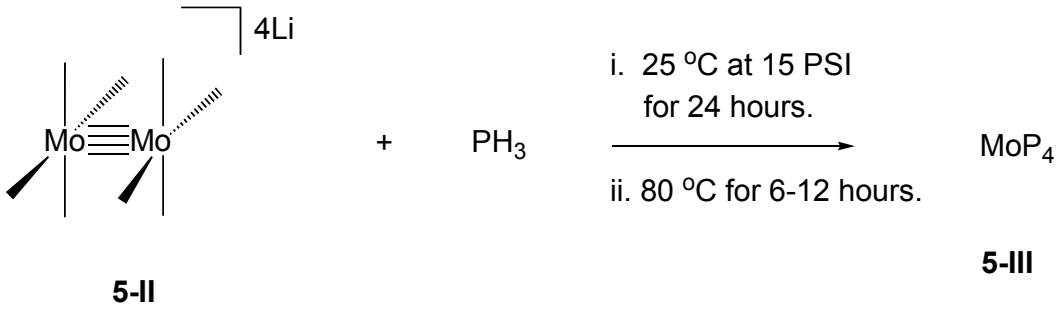

5-II **5-III**

Route 2:

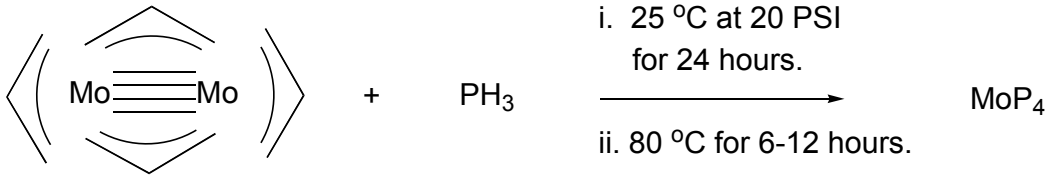

5-IV **5-V**

Scheme V-2: The synthesis of MoP_4 **5-III** (Route 1) and **5-V** (Route 2) via reaction of PH_3 with **5-II** and **5-IV**.

Once PH_3 was introduced to the vibrant green color of **5-IV**, a rapid darkening was observed to a black formation of the MoP_4 (Figure V-1, Route 2). After 24 hours the Fischer-Porter bottle was heated to 80 ^{0}C for several hours to ensure the reaction has gone to completion. The mesoporous MoP_4 materials produced by these two routes were amorphous in character and could be converted to the crystalline MoP_4 phase upon annealing at 400 ^{0}C for 6 hours at 0.1 torr (Figure V-6).

5.2.2: Characterization and electrochemistry

SEM and BET Analysis

By modifying the reaction conditions the morphology of the material synthesized was found to vary. In Route 1 (Scheme V-2, removing the ether solvent under vacuum) and using **5-II** in the solid state on an ITO slide, the resulting particles can be seen to have worm-like porous structures (Figure V-1). This interesting morphology may have formed via the formation of methane gas being released upon the reaction $Li_4Mo_2(CH_3)_8$ with PH_3. The infra-red spectrum of **5-III** has no peaks in the 3000 cm^{-1} region indicating that the Mo-CH_3 groups have been efficiently eliminated. The porous material has an average pore size of 40 nm and was shown to have a surface area of 99 m^2g^{-1} determined by N_2 adsorption-desorption isothermal analysis (BET method) as shown in Figure V-2. The gas sorption of **5-III** is interpreted as a Type IV isotherm exhibited by a mesoporous solid.[24]

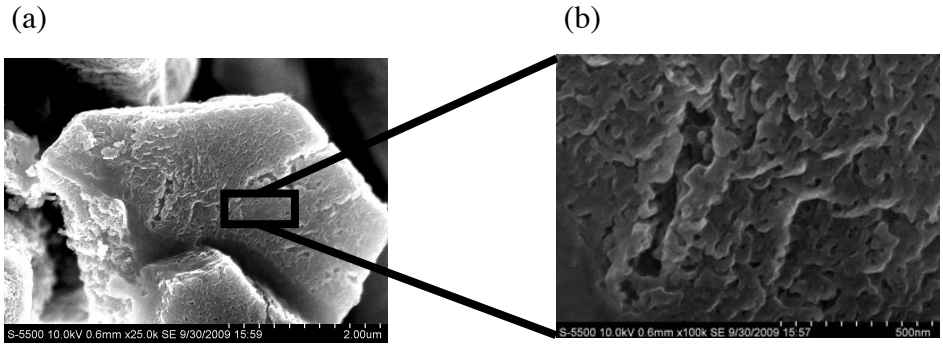

Figure V-1: SEM images of MoP_4 (**5-III**) (a) showing the large particles and (b) higher resolution image displaying the worm-like porosity of the material.

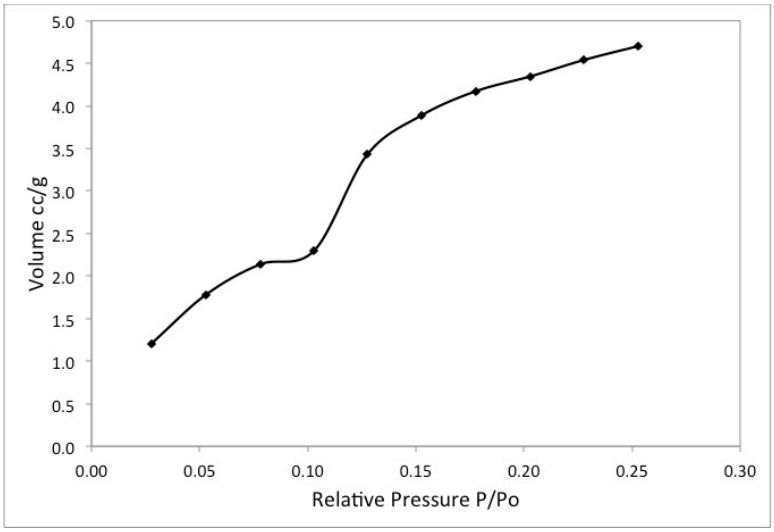

Figure V-2: N_2 adsorption desorption isotherm for MoP_4 (**5-III**).

By changing the substrate to steel, copper, and a carbon block particles of MoP_4 of different sizes and lattice structures were produced (Figure V-3).

(a) (b) (c)

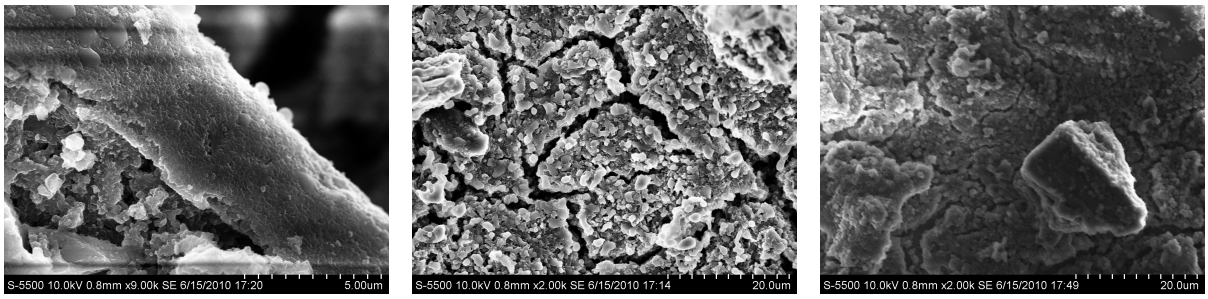

Figure V-3: SEM images of MoP_4 on different substrates of (a) steel, (b) copper, and (c) a block of carbon.

In Route 2 (Scheme V-2, removing the ether solvent under vacuum) and using **5-IV** in the solid state on an ITO slide the resulting material has a quite different morphology from that of **5-III**. SEM images of the powder with particulates ranging in size from 1-4 mm are shown in Figure V-4. This is most likely due to the size of the by-products leaving the material, which are larger than that of the by-products (methane gas) in **5-III**. The use of a starting material that generates very small by-products is a form of controlling the morphology of the resulting TMP. The MoP_4 material of **5-V** was shown to have a surface area of 29.6 m^2g^{-1} determined by N_2 adsorption-desorption isothermal analysis (BET method) as shown in Figure V-5. The average pore-size for the mesoporous materials was on the order of 0.44 nm as determined by multipoint BET pore size distribution. The gas sorption of **5-V** is interpreted as a Type VI isotherm exhibited by a nonporous solid with an almost completely uniform surface.[24]

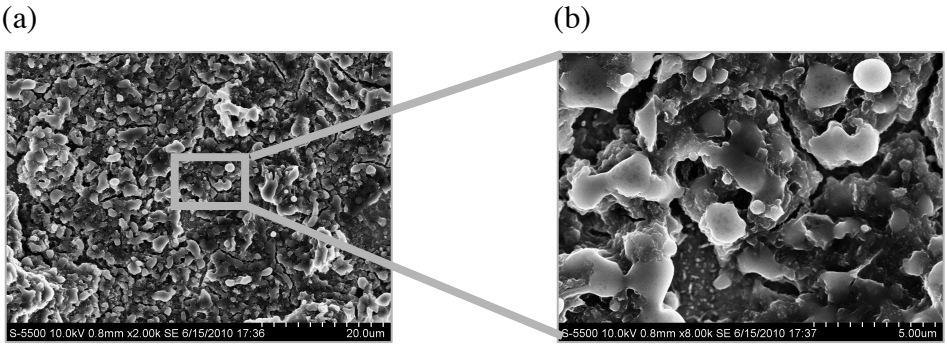

Figure V-4: SEM images of MoP_4 (**5-V**) (a) showing the particulate and (b) higher resolution image displaying the uniformity of the surface of the material.

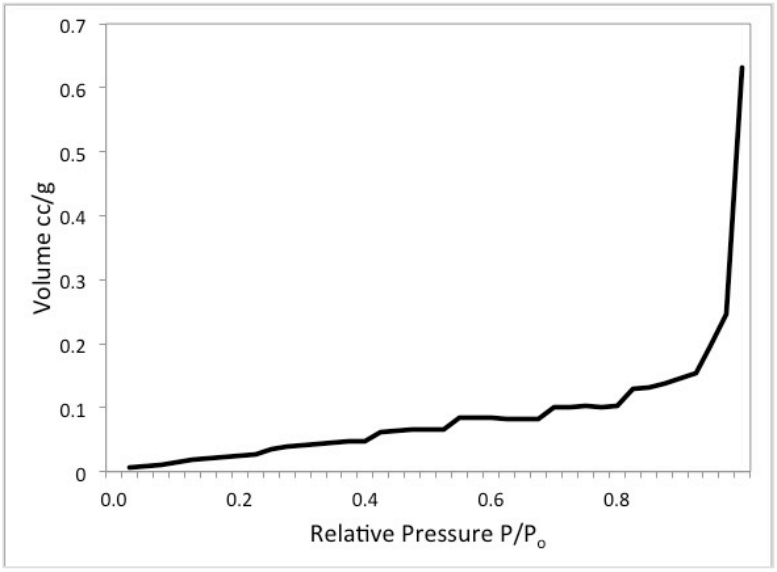

Figure V-5: N_2 adsorption desorption isotherm for MoP_4 (**5-V**).

X-ray diffraction

All materials of MoP_4 were found to be X-ray amorphous, and subsequent thermal treatment to anneal the material resulted in crystalline formation shown as the appearance of peaks in XRD patterns (Figure V-6). Upon annealing at 400 ^{0}C the observed diffraction peaks for **5-III** corresponded to MoP_4 (PDF# 26-1273). Indexing the XRD

powder pattern showed that the compound crystallized in the monoclinic crystal system, space group C2/c with lattice parameters a = 5.3132, b = 11.139, and c = 5.8202 Å.

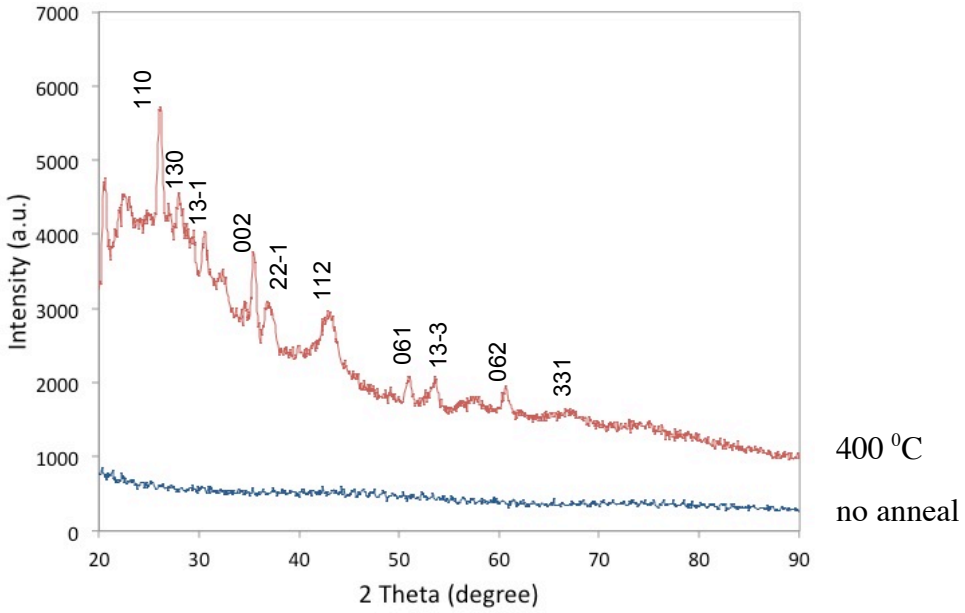

Figure V-6: Powder XRD patterns of MoP_4 prior to annealing and after annealing.

XPS analysis

Using XPS to analyze the surface of the materials formed on different substrates it was determined that for **5-III** and **5-V** deposited on ITO slides an average ratio of 1:4 Mo to P was found. Figure V-7 shows an XPS survey scan for **5-III**. Peaks corresponding to Mo, P, Li, O, and C are present. Peaks with binding energies of 235.4 eV and and 232.7 eV correspond to the 3d doublet of Mo(IV). Peaks with binding energies of 130.4 eV, 52.4 eV, 528.4 eV, and 281.7 eV correspond to the 2p singlet of P, 1s singlet of Li, 1s singlet of O, and 1s singlet of C.

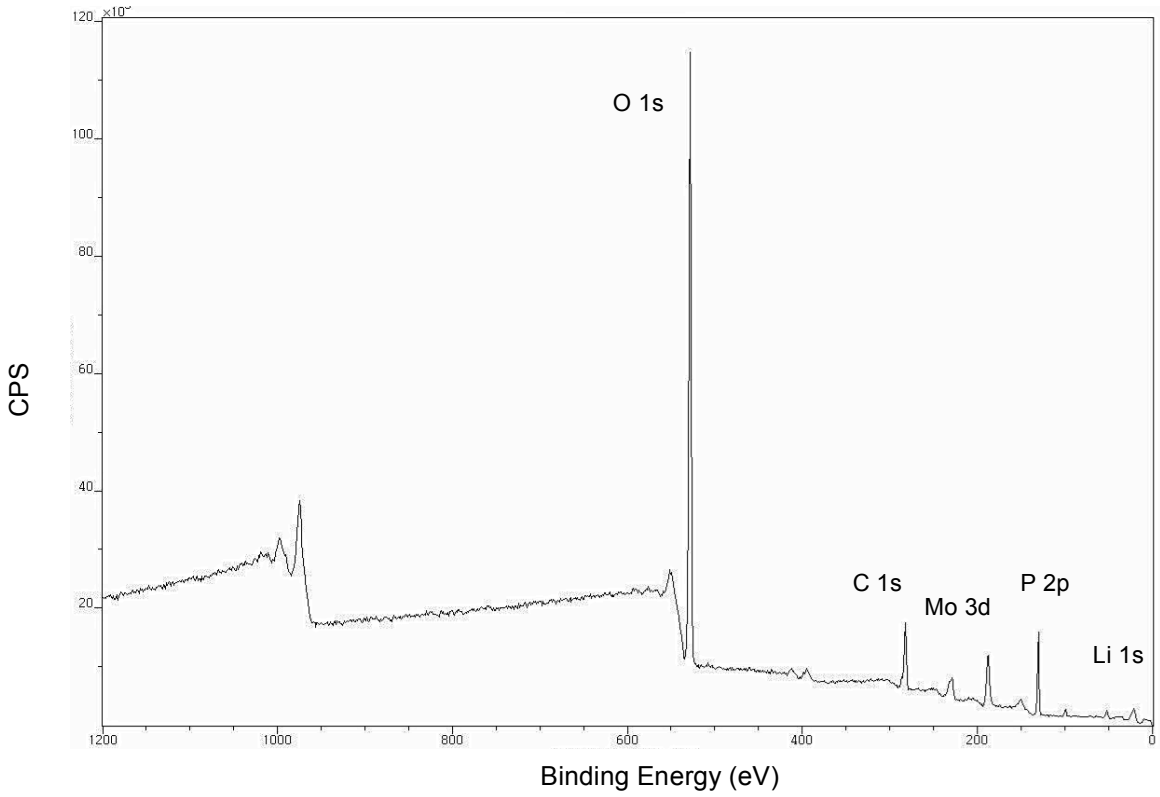

Figure V-7: XPS survey scan of MoP_4 **5-III**.

Upon changing the substrate to copper, steel, or carbon the ratios between Mo and P varied as well as was the case for the reactions resulting in a fine powder precipitate. For samples on ITO the ratios of Mo:P are hypothesized to be more accurate because the ITO slides in the XPS instrument have a charged surface and analysis proceeds without charging the sample while for the other substrates the sample had to be charged to obtain a signal. When the sample needs charging then the signal becomes reduced and broadens making exact calculations difficult. This was seen in the form of a variety of ratios of Mo:P in the substrates of copper, steel, carbon, and with the precipitate itself. XPS analysis of just the precipitate of **5-V** provided no evidence of Mo or P present. Values for Mo, P, Li, C, and O composition from XPS analysis can be seen in Table V-1.

Table V-1: Percent Compositions of samples using XPS

Substrate	*Mo Source*	*Composition (%)*				
		Mo	P	Li	C	O
ITO	**5-III**	8.72	32.04	33.88	20.34	5.02
ITO	**5-V**	7.86	31.02	n/a	44.28	16.84
Copper	**5-III**	5.34	6.54	26.64	14.59	46.89
Copper	**5-V**	5.46	15.84	n/a	23.23	55.57
Steel	**5-III**	5.03	6.29	29.31	15.54	43.82
Steel	**5-V**	7.47	19.49	n/a	23.03	50.03
Carbon	**5-III**	0.42	3.01	24.26	75.92	2.80
Carbon	**5-V**	5.96	14.98	n/a	23.07	55.99
no substrate	**5-III**	7.53	18.34	0.0	23.49	49.65
no substrate	**5-V**	0.0	0.0	n/a	86.84	13.08

Electrochemical studies

The materials **5-III** and **5-V** have been tested in 1.0 M $LiPF_6$ electrolyte dissolved in a 1:1 mixture of EC (ethylene carbonate) and DMC (dimethyl carbonate) and evaluated as anode materials using various electrochemical methods. In particular, slow scan cyclic voltammetry (SSCV) studies offer increased sensitivity to monitoring and separating charge storage processes involving both capacitive and diffusional controlled intercalation behaviors for mesoporous materials. Mesoporous **5-III** shows two different reactions occurring during the electrochemical process which are most likely due to (a) intercalation (equation 1) of Li^+ ions and (b) the conversion reactions that are not fully understood at present (equation 2) as seen in Figure V-8.

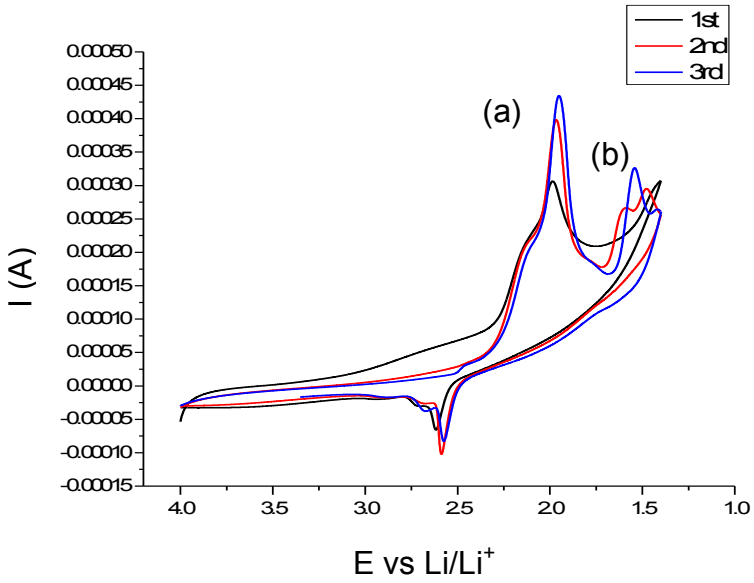

Figure V-8: Voltammetric response of Li^+ insertion/deinsertion in mesoporous MoP_4 film of **5-III** on ITO.

Looking at the change in potential over time within two cycles plateaus are observed which demonstrate the two different chemical processes proceeding in the electrochemistry of **5-III** (Figure V-9).

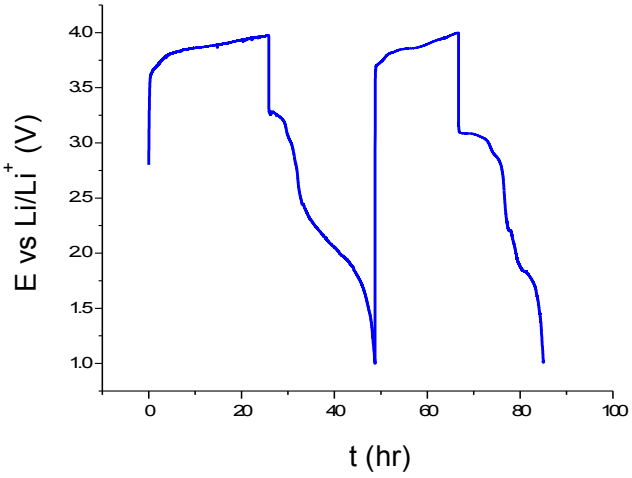

Figure V-9: Galvanostatic plot of Li-ion transport of **5-III** at 2.5 x 10^{-5} A, demonstrating the presence of conversion reactions.

Knowing that the morphology of **5-V** was not mesoporous and had a very low surface area it was not surprising that the material was not a good candidate for the transport of Li-ions as an anode material for batteries. Figure V-10 shows that although the Li^+ is taken in by the material it is an irreversible reaction.

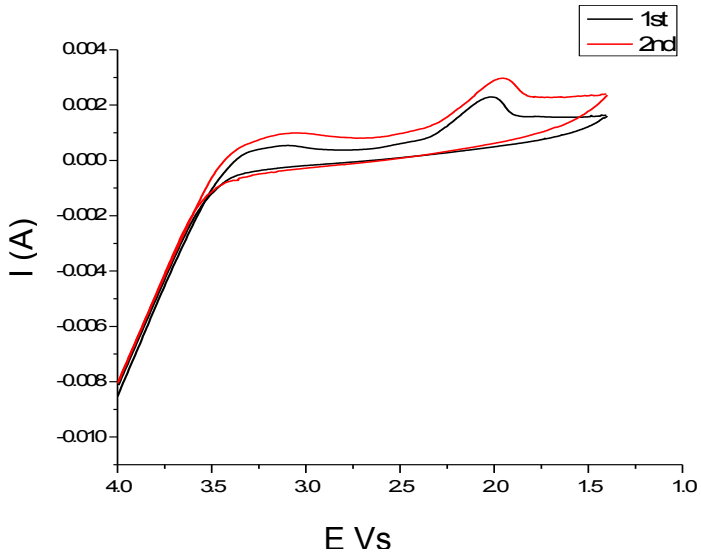

Figure V-10: Voltammetric response of Li^+ insertion/deinsertion in MoP_4 of **5-V**.

5.2.3: Conclusion and Future Studies

In conclusion, the work described the development of a method using mild conditions to synthesize amorphous TMPs, specifically MoP_4, which, depending upon the source of the molybdenum complex and reaction conditions, produces a variety of materials with different morphologies. One in particular, a mesoporous MoP_4 formed on an ITO slide demonstrated a reversible reaction of Li-ion transport and also showed the possible existence of a conversion processes. The next step is to screen other Mo alkyl starting materials to synthesize MoP_4 or other stoichiometries (Mo_xP_y) to further explore the morphologies and electrochemistry of TMPs to make advancements in the understanding of the mechanism of these reactions and, thus, leading to research focused

on expanding the use of these materials that have high capacities, long life cycles, and resist changes in morphology to produce an improved battery.

5.3: EXPERIMENTAL DETAILS

5.3.1: General Synthesis

All reactions were performed under a dry, oxygen-free nitrogen atmosphere or under vacuum using standard Schlenk line and dry box techniques. Solvents were dried prior to use by distillation from sodium benzophenone ketyl anion under nitrogen. The compounds $Mo_2(O_2CCH_3)_4$ (**5-I**), $Li_4Mo_2(CH_3)_8$ (**5-II**), and $Mo_2(C_3H_5)_4$ (**5-IV**) were prepared as previously described.[25] Phosphine (PH_3) (99.996 %) was purchased from Linde and used without further purification. Phosphine is a highly poisonous and reactive gas. All operations were performed by highly trained personnel under rigorous exclusion of air.

5.3.2: Synthesis of molybdenum phosphides

MoP_4 (5-III)

$Li_4Mo_2(CH_3)_8$ (**5-II**) (0.090 g, 0.234 mmol) was dissolved in dry diethyl ether (30 mL) and transferred to a Fischer-Porter bottle (containing ITO slides that had been previously cleaned, dried, and contained under dry, oxygen-free nitrogen atmosphere or vacuum) via cannula. Diethyl ether was removed under vacuum and the solid was cooled to -78 ^{0}C. **5-II** was exposed to an excess of phosphine gas with the resultant pressure of 15 PSI. The flask was sealed, allowed to warm to room temperature, and **5-II** reacted overnight under PH_3. A dark precipitate began to form immediately, and after several hours, the red color of **5-II** began to disappear. Excess PH_3 was removed under vacuum and the black powder was heated to 80 ^{0}C for 6 hours. The bottle was taken into the dry box and the ITO slide of MoP_4 was collected. Isolated: 0.089 g, 86 %.

MoP_4 (5-V)

$Mo_2(C_3H_5)_4$ (**5-IV**) (0.104 g, 0.282 mmol) was dissolved in dry diethyl ether (30 mL) and transferred to a Fischer-Porter bottle (containing ITO slides that had been previously cleaned, dried, and contained under dry, oxygen-free nitrogen atmosphere or vacuum) via cannula. Diethyl ether was removed under vacuum and the solid was cooled to -78 ^{0}C. **5-IV** was introduced to an excess of phosphine gas with the resultant pressure of 20 PSI. The flask was sealed, allowed to warm to room temperature, and **5-IV** reacted overnight under PH_3. A dark precipitate began to form immediately, and after several hours, the green color of **5-IV** began to disappear. Excess PH_3 was removed under vacuum and the black powder was heated to 80 ^{0}C for 6 hours. The bottle was taken into the dry box and the ITO slide of MoP_4 was collected. Isolated: 0.102 g, 83 %.

5.3.3: Instrumental details

XRD analysis was performed on a Bruker D8 diffractometer equipped with a Ge monochromated Cu Kα source. SEM images were collected with a Zeiss Supra 40 VP scanning electron microscope. Nitrogen isotherms were recorded on an Autosorb-I system (Quantachrome) under ultrahigh vacuum in a clean system with a diaphragm and turbo pumping system.

The MoP_4 TMP materials were tested in 1.0 M $LiPF_6$ electrolyte dissolved in a 1:1 mixture of EC (ethylene carbonate) and DMC (dimethyl carbonate) and evaluated as anode materials using slow scan cyclic voltammetry (SSCV). Galvanostatic studies using a current of 2.5 x 10^{-5} A were performed.

All X-ray photoelectron spectra were obtained using a Kratos AXIS Ultra spectrometer equipped with a monochromatized Al Ka source, hybrid optics, and a delay line detector coupled to a hemispherical analyzer. The analysis chamber base pressure was typically 2 x 10-9 Torr. All spectra were recorded using a single sweep with a spot size of 300 μm x 700 μm. Survey scans were collected from 0–1200 eV with a pass

energy of 80 eV, step size of 1 eV, and a dwell time of 250 ms. All binding energies were referenced to the adventitious carbon line (C 1s, 284.8 eV) and charge neutralization was applied during all acquisitions. All samples were prepared in a nitrogen filled glove box and transported directly to the spectrometer.

5.4: REFERENCES

1. M. Armand and J.-M. Tarascon, *Nature (London)*, 2008, **451**, 652-657.

2. J. B. Goodenough and Y. Kim, *Chem. Mater.*, 2009, **22**, 587-603.

3. B. Scrosati, J. Hassoun and Y.-K. Sun, *Energy & Environmental Science*, 2011, **4**, 3287-3295.

4. P. Biensan, B. Simon, J. P. de Guibert, M. Broussely, J. M. Bodet and F. Perton, *J. Power Sources*, 1999, **81,Äì82**, 906-912.

5. D. W. Murphy and P. A. Christian, *Science*, 1979, **205**, 651-656.

6. Y. Shi, B. Guo, S. A. Corr, Q. Shi, Y.-S. Hu, K. R. Heier, L. Chen, R. Seshadri and G. D. Stucky, *Nano Letters*, 2009, **9**, 4215-4220.

7. W. Kaveevivitchai and A. J. Jacobson, *Chem. Mater.*, 2013.

8. D. Mikhailova, A. Sarapulova, A. Voss, A. Thomas, S. Oswald, W. Gruner, D. M. Trots, N. N. Bramnik and H. Ehrenberg, *Chem. Mater.*, 2010, **22**, 3165-3173.

9. M. P. Bichat, F. Gillot, L. Monconduit, F. Favier, M. Morcrette, F. Lemoigno and M. L. Doublet, *Chem. Mater.*, 2004, **16**, 1002-1013.

10. F. Gillot, S. Boyanov, L. Dupont, M. L. Doublet, M. Morcrette, L. Monconduit and J. M. Tarascon, *Chem. Mater.*, 2005, **17**, 6327-6337.

11. K. Wang, J. Yang, J. Xie, B. Wang and Z. Wen, *Electrochemistry Communications*, 2003, **5**, 480-483.

12. V. Mauchamp, P. Moreau, L. Monconduit, M.-L. Doublet, F. Boucher and G. Ouvrard, *The Journal of Physical Chemistry C*, 2007, **111**, 3996-4002.

13. F. Gillot, L. Monconduit and M. L. Doublet, *Chem. Mater.*, 2005, **17**, 5817-5823.

14. J. W. Hall, N. Membreno, J. Wu, H. Celio, R. A. Jones and K. J. Stevenson, *J. Am. Chem. Soc.*, 2012, **134**, 5532-5535.

15. J. R. Dahn, *Physical Review B*, 1991, **44**, 9170-9177.

16. D. C. S. Souza, V. Pralong, A. J. Jacobson and L. F. Nazar, *Science*, 2002, **296**, 2012-2015.

17. M. G. Kim, S. Lee and J. Cho, *J. Electrochem. Soc.*, 2009, **156**, A89-A94.

18. A. E. Henkes and R. E. Schaak, *Chem. Mater.*, 2007, **19**, 4234-4242.

19. A. E. Henkes and R. E. Schaak, *Inorganic Chemistry*, 2007, **47**, 671-677.

20. A. E. Henkes, Y. Vasquez and R. E. Schaak, *J. Am. Chem. Soc.*, 2007, **129**, 1896-1897.

21. *Gmelins Handb. Anorg. Chem., Part C*, 1965, **16**, 45.

22. T. A. Stephenson, E. Bannister and G. Wilkinson, *Journal of the Chemical Society (Resumed)*, 1964, **0**, 2538-2541.

23. D. Lawton and R. Mason, *J. Am. Chem. Soc.*, 1965, **87**, 921-922.

24. S. Lowell and J. E. Shields, *Powder Surface Area and Porosity*, Chapman & Hall, New York, 1991.

25. F. A. Cotton, J. M. Troup, T. R. Webb, D. H. Williamson and G. Wilkinson, *J. Am. Chem. Soc.*, 1974, **96**, 3824-3828.

Glossary

BE	Binding Energy
BET	Brunauer-Emmett-Teller Theory
Cp	Cyclopentadienyl
CPS	Counts Per Second
CVD	Chemical Vapor Deposition
ESI	Electrospray Ionization
hcp	Hexagonal Close Packed
IR	Infrared
MS	Mass Spectrometry
MW	Microwave
NMR	Nuclear Magnetic Resonance
PDF	Powder Diffraction File
PMe_3	Trimethylphosphine
PVC	Physical Vapor Deposition
Pyr	Pyrrolyl
Pz	Pyrazolate
SEM	Scanning Electron Microscopy
TMP	Transition Metal Phosphide
W	Watt
XPS	X-ray Photoelectron Spectroscopy
XRD	X-ray Diffraction

Bibliography

A. R. Yavari, *Nature (London)*, 2006, **439**, 405-406.

I. Goswami and R. Laxman, *Semiconductor International*, 2004, **27**, 49.

K. Seshan, *Handbook of Think-Film Deposition Processes and Techniques*, Noyes, Norwich, NY, 2002.

H. Lee, *Journal of Micromechanical Microengineering*, 2006, **16**, 557.

M. J. Hampden-Smith and T. T. Kodas, *The Chemistry of Metal CVD*, 1994.

D. L. Smith, *Thin-film Deposition: Principles and Practices*, McGraw-Hil, Boston, 1995.

E. A. Trifonova, D. S. Perekalin, K. A. Lyssenko and A. R. Kudinov, *J. Organomet. Chem.*, 2013, **727**, 60-63.

Gmelins Handb. Anorg. Chem., Part C, 1965, **16**, 45.

C. H. Wang, L. F. Xu, X.-L. Fan and J.-T. Wang, *Phys. Lett. A*, 2011, **375**, 562-567.

L. Calucci, F. G. N. Cloke, U. Englert, P. B. Hitchcock, G. Pampaloni, C. Pinzino, F. Puccini and M. Volpe, *Dalton Transactions*, 2006, 4228-4234.

H. Lee, *Journal of Microelectronics and Microengineering*, 2006, **16**, 557.

F. J. Williams, M. S. Tikhov, A. Palermo, N. Macleod and R. M. Lambert, *The Journal of Physical Chemistry B*, 2001, **105**, 2800-2808.

L. Marot, G. De Temmerman, V. Thommen, D. Mathys and P. Oelhafen, *Surface and Coatings Technology*, 2008, **202**, 2837-2843.

J. H. Rivers, L. J. DePue Anderson, C. M. N. Starr and R. A. Jones, *Dalton Transactions*, 2012, **41**, 5401-5408.

E. M. Gordon, D. C. Gaba, K. A. Jebber and D. M. Zacharias, *Organometallics*, 1993, **12**, 5020-5022.

Y. Chi, H.-L. Yu, W.-L. Ching, C.-S. Liu, Y.-L. Chen, T.-Y. Chou, S.-M. Peng and G.-H. Lee, *J. Mater. Chem.*, 2002, **12**, 1363-1369.

Y. H. Song, Y. L. Chen, Y. Chi, C. S. Liu, W. L. Ching, J. J. Kai, R. S. Chen, Y. S. Huang and A. J. Carty, *Chemical Vapor Deposition*, 2003, **9**, 162-169.

Y. Chi, E. Lay, T. Y. Chou, Y. H. Song and A. J. Carty, *Chemical Vapor Deposition*, 2005, **11**, 206-212.

W. J. McCarty, X. Yang, L. J. D. Anderson and R. A. Jones, *Dalton Transactions*, 2012, **41**, 173-179.

J. Shin, A. Waheed, K. Agapiou, W. A. Winkenwerder, H.-W. Kim, R. A. Jones, G. S. Hwang and J. G. Ekerdt, *J. Am. Chem. Soc.*, 2006, **128**, 16510-16511.

V. K. Ahluwalia, *Alternate energy processes in chemical synthesis : microwave, ultrasonic, and photo activation*, Alpha Science International Ltd., Oxford, U.K. :, 2008.

S. Caddick, *Tetrahedron*, 1995, **51**, 10403-10432.

L. Perreux and A. Loupy, *Tetrahedron*, 2001, **57**, 9199-9223.

R. S. Varma, *Green Chemistry*, 1999, **1**, 43-55.

U. A. A. Mirza, John Wiley & Sons, 2011, pp. 213-229.

D. J. Varughese, M. S. Manhas and A. K. Bose, *Tetrahedron Lett.*, 2006, **47**, 6795-6797.

B. K. Banik, K. J. Barakat, D. R. Wagle, M. S. Manhas and A. K. Bose, *The Journal of Organic Chemistry*, 1999, **64**, 5746-5753.

C. O. Kappe and D. Doris, *Nature Reviews Drug Discovery*, 2005, **5**, 51-63.

A. Stambouli, M. Chastrette and M. Soufiaoui, *Tetrahedron Lett.*, 1991, **32**, 1723.

R. Laurent, A. Laporterie, J. Dubac and J. Berlan, *Organometallics*, 1994, **13**, 2493-2495.

F. Adámek and M. Hájek, *Tetrahedron Lett.*, 1992, **33**, 2039-2042.

R. N. Gedye, W. Rank and K. C. Westaway, *Can. J. Chem.*, 1991, **69**, 706-711.

G. B. Jones and B. J. Chapman, *The Journal of Organic Chemistry*, 1993, **58**, 5558-5559.

R. Gedye, F. Smith, K. Westaway, H. Ali, L. Baldisera, L. Laberge and J. Rousell, *Tetrahedron Lett.*, 1986, **27**, 279-282.

J. F. Watts and J. Wolstenholme, *An introduction to surface analysis by XPS and AES*, J. Wiley, New York, NY, 2003.

D. Briggs and J. T. Grant, *Surface Analysis by Auger and X-Ray Photoelectron Spectroscopy*, IM Publications, 2003.

J. W. Hall, N. Membreno, J. Wu, H. Celio, R. A. Jones and K. J. Stevenson, *J. Am. Chem. Soc.*, 2012, **134**, 5532-5535.

B. Scrosati, *Nat Nano*, 2007, **2**, 598-599.

M. J. Hampden-Smith and T. T. Kodas, *The Chemistry of Metal CVD*, 1994.

I. K. Igumenov, N. V. Gelfond, N. B. Morozova and H. Nizard, *Chemical Vapor Deposition*, 2007, **13**, 633-637.

E. L. Crane, Y. You, R. G. Nuzzo and G. S. Girolami, *J. Am. Chem. Soc.*, 2000, **122**, 3422-3435.

J. Gatineau, K. Yanagita and C. Dussarrat, *Microelectron. Eng.*, 2006, **83**, 2248-2252.

J. Gatineau and C. Dussarrat, *ECS Transactions*, 2007, **6**, 303-307.

Y. H. Song, Y. L. Chen, Y. Chi, C. S. Liu, W. L. Ching, J. J. Kai, R. S. Chen, Y. S. Huang and A. J. Carty, *Chemical Vapor Deposition*, 2003, **9**, 162-169.

J. Shin, A. Waheed, K. Agapiou, W. A. Winkenwerder, H.-W. Kim, R. A. Jones, G. S. Hwang and J. G. Ekerdt, *J. Am. Chem. Soc.*, 2006, **128**, 16510-16511.

S. Caddick, *Tetrahedron*, 1995, **51**, 10403-10432.

T. Matsumura-Inoue, M. Tanabe, T. Minami and T. Ohashi, *Chem. Lett.*, 1994, **23**, 2443-2446.

P. Lidstroum, J. Tierney, B. Wathey and J. Westman, *Tetrahedron*, 2001, **57**, 9225-9283.

R. S. Varma, *Green Chemistry*, 1999, **1**, 43-55.

T. Brietzke, W. Mickler, A. Kelling, U. Schilde, H.-J. Krüger and H.-J. Holdt, *European Journal of Inorganic Chemistry*, 2012, **2012**, 4632-4643.

K. Servaty, C. Moucheron and A. Kirsch-De Mesmaeker, *Dalton Transactions*, 2011, **40**, 11704-11711.

T. David Pilz, N. Rockstroh and S. Rau, *J. Coord. Chem.*, 2010, **63**, 2727-2742.

S. Herrero, R. Jimenez-Aparicio, J. Perles, J. L. Priego and F. A. Urbanos, *Green Chemistry*, 2010, **12**, 965-967.

R. A. Jones, G. Wilkinson, A. M. R. Galas, M. B. Hursthouse and K. M. A. Malik, *J. Chem. Soc., Dalton Trans.*, 1980, 1771-1778.

M. I. Bruce, M. G. Humphrey, M. R. Snow, E. R. T. Tiekink and R. C. Wallis, *J. Organomet. Chem.*, 1986, **314**, 311-322.

R. A. Jones, F. M. Real, G. Wilkinson, A. M. R. Galas, M. B. Hursthouse, K. M. A. Malik, *J. Chem. Soc., Dalton Trans.,* 1980, 511-518.

D. Villemin, M. Hammadi, M. Hachemi and N. Bar, *Molecules*, 2001, **6**, 831-844.

O. Renn and L. M. Venanzi, *Helv. Chim. Acta*, 1995, **78**, 993-999.

M. S. Mudholkar and L. T. Thompson, *J. Appl. Phys.*, 1995, **77**, 5138-5143.

S. L. Roberson, D. Finello and R. F. Davis, *Thin Solid Films*, 1998, **324**, 30-36.

R. Fix, R. G. Gordon and D. M. Hoffman, *Thin Solid Films*, 1996, **288**, 116-119.

M. Damayanti, *J. Electrochem. Soc.*, 2006, **153**, J41.

Y. H. Song, Y. L. Chen, Y. Chi, C. S. Liu, W. L. Ching, J. J. Kai, R. S. Chen, Y. S. Huang and A. J. Carty, *Chemical Vapor Deposition*, 2003, **9**, 162-169.

J. Shin, A. Waheed, K. Agapiou, W. A. Winkenwerder, H.-W. Kim, R. A. Jones, G. S. Hwang and J. G. Ekerdt, *J. Am. Chem. Soc.*, 2006, **128**, 16510-16511.

J. H. Rivers, L. J. DePue Anderson, C. M. N. Starr and R. A. Jones, *Dalton Transactions*, 2012, **41**, 5401-5408.

L. McElwee-White, *Dalton Transactions*, 2006, **0**, 5327-5333.

W. J. McCarty, X. Yang, L. J. D. Anderson and R. A. Jones, *Dalton Transactions*, 2012, **41**, 173-179.

I. Jipa, K. Danova, N. Popovska, M. A. Siddiqi, R. A. Siddiqui, B. Atakan, T. Cremer, F. Maier, H. Marbach, H.-P. Steinruck, F. W. Heinemann and U. Zenneck, *J. Mater. Chem.*, 2011, **21**, 3014-3024.

Y. Chi, E. Lay, T. Y. Chou, Y. H. Song and A. J. Carty, *Chemical Vapor Deposition*, 2005, **11**, 206-212.

T. Ando, N. Nakata, K. Suzuki, T. Matsumoto and S. Ogo, *Dalton Transactions*, 2012, **41**, 1678-1682.

Y. Chi, H.-L. Yu, W.-L. Ching, C.-S. Liu, Y.-L. Chen, T.-Y. Chou, S.-M. Peng and G.-H. Lee, *J. Mater. Chem.*, 2002, **12**, 1363-1369.

P. Pertici, G. Vitulli, M. Paci and L. Porri, *Journal of the Chemical Society, Dalton Transactions*, 1980, 1961-1964.

G. L. Hardgrove, Templeton, D. H.,, *Acta Crystallographica*, 1959, **12**, 28-32.

A. G. Walstrom, M. Pink, X. Yang and K. G. Caulton, *Dalton Transactions*, 2009, **0**, 6001-6006.

A. J. Deeming, S. S. Ullah, A. J. P. Domingos, B. F. G. Johnson and J. Lewis, *Journal of the Chemical Society, Dalton Transactions*, 1974, **0**, 2093-2104.

E. A. Trifonova, D. S. Perekalin, K. A. Lyssenko and A. R. Kudinov, *J. Organomet. Chem.*, 2013, **727**, 60-63.

C. H. Wang, L. F. Xu, X.-L. Fan and J.-T. Wang, *Phys. Lett. A*, 2011, **375**, 562-567.

L. Calucci, F. G. N. Cloke, U. Englert, P. B. Hitchcock, G. Pampaloni, C. Pinzino, F. Puccini and M. Volpe, *Dalton Transactions*, 2006, 4228-4234.

O. Renn and L. M. Venanzi, *Helv. Chim. Acta*, 1995, **78**, 993-999.

J. F. Watts and J. Wolstenholme, *An introduction to surface analysis by XPS and AES*, J. Wiley, New York, NY, 2003.

P. K. Wu, *MRS Online Proceedings Library*, 1995, **385**, null-null.

P. M. A. Sherwood, *J. Electron Spectrosc. Relat. Phenom.*, 1996, **81**, 319-342.

N. S. McIntyre, P. A. Spevack and M. J. Walzak, *Journal of Surface Review Letters*, 1995, **2**, 689-699.

G. C. Herdt, D. R. Jung and A. W. Czanderna, *Prog. Surf. Sci.*, 1995, **50**, 103-129.

S. Pignataro, *Fresenius. J. Anal. Chem.*, 1995, **353**, 227-233.

S. Iwata and A. Ishizaka, *J. Appl. Phys.*, 1996, **79**, 6653-6713.

S. Chen, L. Xie and F. Xue, *Appl. Surf. Sci.*, 2013, **276**, 454-457.

S. Chen, F. Yan, F. Xue, L. Yang and J. Liu, *Mater. Chem. Phys.*, 2010, **124**, 472-476.

W. Liao and J. G. Ekerdt, *Chem. Mater.*, 2013, **25**, 1793-1799.

H. Lee, *Journal of Microelectronics and Microengineering*, 2006, **16**, 557.

F. J. Williams, M. S. Tikhov, A. Palermo, N. Macleod and R. M. Lambert, *The Journal of Physical Chemistry B*, 2001, **105**, 2800-2808.
L. Marot, G. De Temmerman, V. Thommen, D. Mathys and P. Oelhafen, *Surface and Coatings Technology*, 2008, **202**, 2837-2843.

J. H. Rivers, L. J. DePue Anderson, C. M. N. Starr and R. A. Jones, *Dalton Transactions*, 2012, **41**, 5401-5408.

J. Shin, A. Waheed, K. Agapiou, W. A. Winkenwerder, H.-W. Kim, R. A. Jones, G. S. Hwang and J. G. Ekerdt, *J. Am. Chem. Soc.*, 2006, **128**, 16510-16511.

J. Shin, A. Waheed, W. A. Winkenwerder, H.-W. Kim, K. Agapiou, R. A. Jones, G. S. Hwang and J. G. Ekerdt, *Thin Solid Films*, 2007, **515**, 529-5307.

V. V. Bakovets, V. N. Mitkin and N. V. Gelfond, *Chemical Vapor Deposition*, 2005, **11**, 112-117.

A. Panneerselvam, M. A. Malik, M. Afzaal, P. O'Brien and M. Helliwell, *J. Am. Chem. Soc.*, 2008, **130**, 2420-2421.

T. Kada, M. Ishikawa, H. Machida, A. Ogura, Y. Ohshita and K. Soai, *J. Cryst. Growth*, 2005, **275**, e1115-e1119.

S. T. Oyama, *J. Catal.*, 2003, **216**, 343-352.

N. Bahlawane, P. A. Premkumar, Z. Tian, X. Hong, F. Qi and K. Kohse-Huinghaus, *Chem. Mater.*, 2009, **22**, 92-100.

R. A. Fischer, W. Scherer, M. Kleine, O. Lehmann and M. Stuke, *Chem. Mater.*, 1995, **7**, 1863-1872.

M. Armand and J.-M. Tarascon, *Nature (London)*, 2008, **451**, 652-657.

J. B. Goodenough and Y. Kim, *Chem. Mater.*, 2009, **22**, 587-603.

B. Scrosati, J. Hassoun and Y.-K. Sun, *Energy & Environmental Science*, 2011, **4**, 3287-3295.

P. Biensan, B. Simon, J. P. de Guibert, M. Broussely, J. M. Bodet and F. Perton, *J. Power Sources*, 1999, **81,Äì82**, 906-912.

D. W. Murphy and P. A. Christian, *Science*, 1979, **205**, 651-656.

Y. Shi, B. Guo, S. A. Corr, Q. Shi, Y.-S. Hu, K. R. Heier, L. Chen, R. Seshadri and G. D. Stucky, *Nano Letters*, 2009, **9**, 4215-4220.

W. Kaveevivitchai and A. J. Jacobson, *Chem. Mater.*, 2013.

D. Mikhailova, A. Sarapulova, A. Voss, A. Thomas, S. Oswald, W. Gruner, D. M. Trots, N. N. Bramnik and H. Ehrenberg, *Chem. Mater.*, 2010, **22**, 3165-3173.

M. P. Bichat, F. Gillot, L. Monconduit, F. Favier, M. Morcrette, F. Lemoigno and M. L. Doublet, *Chem. Mater.*, 2004, **16**, 1002-1013.

F. Gillot, S. Boyanov, L. Dupont, M. L. Doublet, M. Morcrette, L. Monconduit and J. M. Tarascon, *Chem. Mater.*, 2005, **17**, 6327-6337.

K. Wang, J. Yang, J. Xie, B. Wang and Z. Wen, *Electrochemistry Communications*, 2003, **5**, 480-483.

V. Mauchamp, P. Moreau, L. Monconduit, M.-L. Doublet, F. Boucher and G. Ouvrard, *The Journal of Physical Chemistry C*, 2007, **111**, 3996-4002.

F. Gillot, L. Monconduit and M. L. Doublet, *Chem. Mater.*, 2005, **17**, 5817-5823.

J. W. Hall, N. Membreno, J. Wu, H. Celio, R. A. Jones and K. J. Stevenson, *J. Am. Chem. Soc.*, 2012, **134**, 5532-5535.

J. R. Dahn, *Physical Review B*, 1991, **44**, 9170-9177.

D. C. S. Souza, V. Pralong, A. J. Jacobson and L. F. Nazar, *Science*, 2002, **296**, 2012-2015.

M. G. Kim, S. Lee and J. Cho, *J. Electrochem. Soc.*, 2009, **156**, A89-A94.

A. E. Henkes and R. E. Schaak, *Chem. Mater.*, 2007, **19**, 4234-4242.

A. E. Henkes and R. E. Schaak, *Inorganic Chemistry*, 2007, **47**, 671-677.

A. E. Henkes, Y. Vasquez and R. E. Schaak, *J. Am. Chem. Soc.*, 2007, **129**, 1896-1897.

Gmelins Handb. Anorg. Chem., Part C, 1965, **16**, 45.

T. A. Stephenson, E. Bannister and G. Wilkinson, *Journal of the Chemical Society (Resumed)*, 1964, **0**, 2538-2541.

D. Lawton and R. Mason, *J. Am. Chem. Soc.*, 1965, **87**, 921-922.

S. Lowell and J. E. Shields, *Powder Surface Area and Porosity*, Chapman & Hall, New York, 1991.

F. A. Cotton, J. M. Troup, T. R. Webb, D. H. Williamson and G. Wilkinson, *J. Am. Chem. Soc.*, 1974, **96**, 3824-3828.

Vita

Lauren Joy De Pue graduated from Larry A. Ryle High School in Union, Kentucky in 2000. She then entered the University of Kentucky and completed a degree of Bachelor of Science in Chemistry and Biology in May 2004, during which time she worked under Prof. David A. Atwood and Brian C. Rymond. In August 2004 she attended Yale University in New Haven, Connecticut where she earned a Masters in Chemistry in June 2006. In August 2006, she came to The University of Texas at Austin to begin graduate school in the laboratory of Prof. Richard A. Jones toward the completion of her Ph.D.

Permanent address: LaurenJoyDePue@gmail.com

This dissertation was typed by the author.